Measurement of the ^{22}Ne$(p,\gamma)^{23}$Na reaction using the DRAGON facility and commissioning of the EMMA recoil mass spectrometer

Matthew Williams

Doctor of Philosophy

University of York

Physics

November 2018

Abstract

The ^{22}Ne$(p,\gamma)^{23}$Na reaction rate has been shown to have a significant impact on the abundances of elements produced in a variety of astrophysical environments. This thesis presents results obtained from the first inverse kinematics study of the ^{22}Ne$(p,\gamma)^{23}$Na reaction, which was undertaken using the DRAGON recoil separator facility at TRIUMF. The strengths of resonances at $E_{c.m.} = 181, 248, 458, 610, 632$ and 1222 keV were measured, as well as the non-resonant contribution in the range of $282 \leqslant E_{c.m.} \leqslant 511$ keV. The important reference resonance at $E_{c.m.} = 458$ keV is found to have a strength of $\omega\gamma = 0.467(14)$ eV, which is significantly lower than previously reported values. The astrophysical impact of the new ^{22}Ne$(p,\gamma)^{23}$Na reaction rate was assessed, with respect to the most recent STARLIB compilations, using a variety classical nova and asymptotic giant branch (AGB) star nucleosynthesis models. The new rate results in changes of up to a factor of two in ^{22}Ne and ^{23}Na abundances produced in oxygen-neon and carbon-oxygen classical novae respectively, whereas no significant changes are evident for the low and intermediate mass AGB star models considered here.

This thesis also documents the successful commissioning of a new recoil mass spectrometer located at the TRIUMF ISAC-II facility. The Electromagnetic Mass Analyser (EMMA) is designed to separate the products of nuclear reactions and disperse those products onto focal plane detectors in accordance with their mass/charge (m/q) ratio. EMMA's acceptances, transport efficiencies, resolution and dispersion were investigated in a series of in-beam and alpha source tests. Results from these tests compare favourably with design expectations, with the exception of apparently reduced vertical angle acceptance and larger than expected geometric aberrations at large horizontal angles; both require further investigation. In addition, EMMA was successfully able to identify the heavy products of fusion evaporation reactions induced by beams of ^{23}Na and ^{24}Na on a natural-Cu target. Together, the results from these commissioning tests represent important and necessary first steps toward implementing EMMA into the experimental nuclear physics program at ISAC.

Contents

List of Figures

List of Tables

Acknowledgements

In a project with such a long and rich history as EMMA, I cannot help but feel as if I joined the marathon for the last few miles. To adequately capture the extent of everyone's contribution to a mountain of work, upon which I find myself standing, would require a chapter of its own. So on that score I must offer my sincere apologies, and force myself to be more economical with my words than I would otherwise wish.

Firstly I thank my TRIUMF supervisor Dr Barry Davids, who immediately made me feel like a valued member of the EMMA group. After so many years of effort, it gives me a great sense of satisfaction to have helped bring your brainchild to fruition. Secondly to my York supervisor Professor Brian Fulton, your sagely guidance and gentle encouragement have helped me to persevere despite times of frustration, and to become a better physicist in the process. This brings me neatly on to thanking fellow members of the clean room 'Sisyphus crew': Jon Lighthall, Kevan Hudson, Caleb Ward, and the many co-op students. While leaving a 'makers mark' on your handy-work would not bode well for electrostatic properties, your tireless efforts will not be forgotten by me. I owe special gratitude to Jon Lighthall and his family for making me feel welcome in Canada and in the EMMA group. Peter Machule, Martin Alcorta, Nicholas Esker and Naimat Khan also deserve many thanks for their exhaustive efforts in making EMMA a reality.

I must also give thanks to all members of the DRAGON group, particularly to post-docs Annika Lennarz and Devin Connolly who helped me understand how DRAGON experiments are analysed. Putting the xenon incident to one side, both of you have set a very high standard as young researches that I hope to follow. A big thank-you must also go to Dr Alison Laird, who first proposed the $^{22}\mathrm{Ne}(p,\gamma)^{23}\mathrm{Na}$ measurement and later put me in contact with her esteemed collaborators in the astrophysical modelling community: Professor Jordi José and Dr Umberto Battino, each of whom provided calculation results in their respective fields of specialization. Further acknowledgements of their specific inputs are given in the relevant sections.

My deepest thanks also to the students and post-docs, past and present, whom I've had the pleasure of meeting, befriending and pubbing with over the course of my time at the University of York and TRIUMF. I started an attempt to list you all, but quickly realised that I should probably leave room for my thesis.

Lastly to my family, I have always carried your love and support with me, from my first day at school, to completing my PhD. Finding the right words to express my gratitude is utterly beyond me; so I will simply say thank you, for everything.

Declaration of Authorship

I declare that this thesis is a presentation of original work and I am the sole author. This work has not previously been presented for an award at this, or any other, University. All sources are acknowledged as References.

Chapter 1

Astrophysical Motivation

1.1 Stellar evolution

For most of human history stars have been thought of as unchanging by-standers in our universe; indeed Aristotle stated in his treatise *On the Heavens*: "In the whole range of time past, so far as our inherited records reach, no change appears to have taken place either in the whole scheme of the outermost heaven or in any of its proper parts". Modern science however, has revealed a far more active role for stars, which are dynamic, i.e. change with time, and are responsible for the creation of all the elements found in nature, with the exception of the most simple varieties left over from the Big Bang (mainly hydrogen and helium). The time-scales over which stars gradually build the complexity of the universe today are enormous, with life-cycles that are perceptible only on the order of billions of years, dwarfing any anthropological records Aristotle would have relied upon. The evolution of stars must instead be pieced together by taking snap shots gathered from extensive surveys of many stars at various evolutionary stages. Only through performing this exercise do certain patterns emerge.

The exercise of cataloguing stellar characteristics began in the late 19^{th} century, which laid the foundations for stellar physics in the early 20th century, most notably through the work of Arthur Eddington who showed that nuclear processes could describe energy generation in stars [1]. The most famous plot of stellar characteristics is the Hertzsprung-Russell (HR) diagram, which plots luminosity (or intrinsic brightness) vs surface temperature (or colour). The HR diagram represents a major piece of the puzzle towards understanding how stars evolve with time. A HR diagram for stars within the local solar neighbourhood is shown by Figure 1.1, with labels indicating the main stellar categories associated with different evolutionary stages. This section will outline the main phases of stellar evolution and the nuclear processes driving them, as it is the consumption of

nuclear 'fuel' via thermonuclear reactions that cause stars to shine, induce changes in their characteristics, and ultimately limits their life-spans.

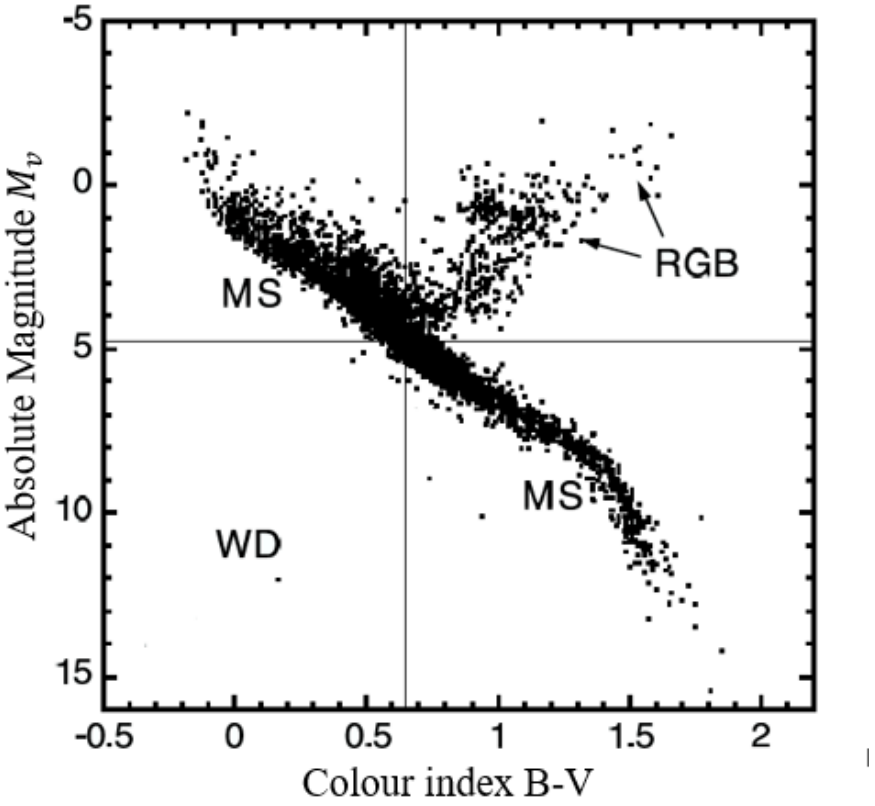

FIGURE 1.1: Hertzsprung-Russell diagram of 5000 stars from the solar neighbourhood with well-known distances. Three populated regions are labelled: the main sequence (MS), red giant branch (RGB), and white dwarf (WD) region. The cross hairs indicate the location of the sun. Figure reproduced from Ref [2], using data taken from the Hipparcos space satellite.

1.1.1 Star formation

Stars are formed from gas clouds, primarily composed of hydrogen and helium, which collapse inwards provided that the gas density is sufficient for the gravitational potential energy of the cloud to exceed its internal kinetic energy. As the cloud undergoes a free-fall collapse, gravitational potential energy is converted into thermal energy and radiation. Eventually the temperature of the gas will rise enough to dissociate molecular hydrogen, and then ionize the hydrogen which - along with the increasing density - causes the opacity of the cloud to increase. This in turn slows the collapse of the cloud as the pressure from thermal energy increases. As the temperature in the core rises, some nuclear reactions become feasible, firstly through deuterium burning via $^2\mathrm{H}(p,\gamma)^3\mathrm{He}$, and then destruction of lithium also via proton capture. Only stars which have an initial mass above 0.08 $M_\odot$ will reach core temperatures high enough to ignite

hydrogen burning, at which point the energy produced from nuclear reactions will be sufficient to support the star against further gravitational collapse, and hence hydrostatic equilibrium is reached. Gas clouds below this mass will eventually become predominantly supported by electron degeneracy pressure before the temperature rises to levels needed to be supported by hydrogen burning, and thus are classed as brown dwarfs. A more quantitative description of the criteria for gravitational collapse and ignition of nuclear burning can be found in Ref [3].

1.1.2 Main sequence burning

Stars that burn hydrogen in their cores are classed as main sequence (MS) stars, and appear on the Hertzsprung-Russell diagram as indicated by Figure 1.1. Hydrostatic hydrogen burning can primarily occur via two sets of reaction mechanisms: the pp-chains and CNO cycles. The latter requires the initial cloud to be enriched with seed material from a previous generation of stars, however the former can take place just from primordial material left over from the big bang. Both of these reaction mechanisms involve the processing of four hydrogen nuclei into a helium nucleus, along with the release of 26.731 MeV of energy. The pp chains proceed through a series of reactions involving only light nuclei up to $A = 8$, shown diagrammatically by Figure 1.2 with the reactions listed in Table 1.1. The $p(p, e^+\nu)d$ reaction (common to all three pp chains) proceeds extremely slowly[1], both in absolute terms and relative to other reactions listed in Table 1.1, and therefore dictates the time-scale of core hydrogen burning, keeping stars on the main sequence for most of their lifespans.

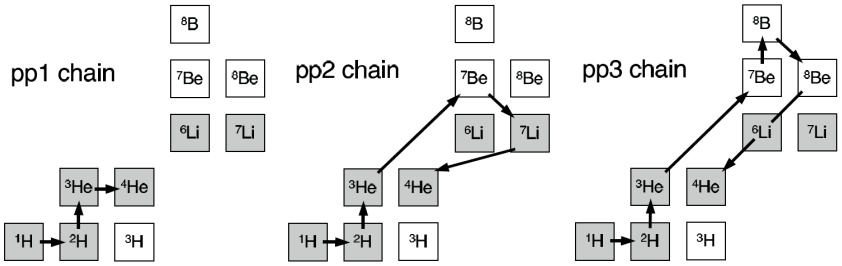

FIGURE 1.2: Diagram of the pp chains, with arrows representing the nuclear reactions involved and their direction. Grey boxes indicate stable isotopes, white are radioactive. Figure taken from from Ref [2].

The Sun generates approximately 90% of its energy through the pp1 chain, with the remainder coming from the pp2 chain. Stars that are more massive than the Sun, and hence achieve greater core temperatures, will begin to generate more energy via the CNO

[1]This reaction proceeds slowly due to being mediated by the weak nuclear force. Though its cross section is too small for feasible direct measurements, it has a relatively small uncertainty since the electro-weak interaction is fairly well constrained.

pp1 chain	pp2 chain	pp3 chain
$p(p, e^+\nu)d$	$p(p, e^+\nu)d$	$p(p, e^+\nu)d$
$d(p, \gamma)^3\mathrm{He}$	$d(p, \gamma)^3\mathrm{He}$	$d(p, \gamma)^3\mathrm{He}$
$^3\mathrm{He}(^3\mathrm{He}, 2p)\alpha$	$^3\mathrm{He}(\alpha, \gamma)^7\mathrm{Be}$	$^3\mathrm{He}(\alpha, \gamma)^7\mathrm{Be}$
	$^7\mathrm{Be}(e^-, \nu)^7\mathrm{Li}$	$^7\mathrm{Be}(p, \gamma)^8\mathrm{B}$
	$^7\mathrm{Li}(p, \alpha)\alpha$	$^8\mathrm{B}(\beta^+\nu)^8\mathrm{Be}$
		$^8\mathrm{Be}(\alpha)\alpha$

TABLE 1.1: List of nuclear reactions involved in the pp chains.

cycles. Here the CNO material acts as a catalyst for the conversion of four hydrogen nuclei into a helium nucleus. Note that since there are no stable mass $A = 5$ or 8 nuclei the CNO material cannot be produced via the pp chains, and must instead be included as part of the initial chemical composition of the star. As displayed by Figure 1.3 and listed in Table 1.2, the CNO cycles all proceed via a series of proton radiative captures, beta-decays, and are closed by a (p, α) reaction.

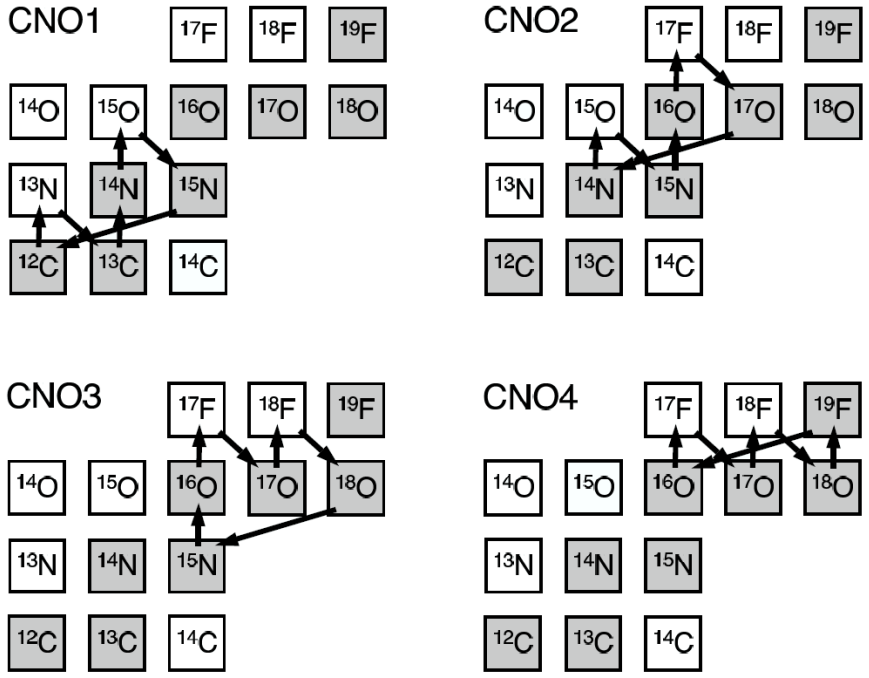

FIGURE 1.3: Diagram of the CNO cycles, with arrows representing the nuclear reactions involved and their direction. Grey boxes indicate stable isotopes, white are radioactive. Figure taken from Ref [2].

1.1.3 Leaving the main sequence

As the core becomes depleted of hydrogen it begins to contract to generate energy that is no longer provided by nuclear processes, though hydrogen burning continues to proceed in a shell surrounding the core. The additional energy output from the hydrogen burning

CNO1	CNO2	CNO3	CNO4
$^{12}C(p,\gamma)^{13}N$	$^{14}N(p,\gamma)^{15}O$	$^{15}N(p,\gamma)^{16}O$	$^{16}O(p,\gamma)^{17}F$
$^{13}N(\beta^+\nu)^{13}C$	$^{15}O(\beta^+\nu)^{15}N$	$^{16}O(p,\gamma)^{17}F$	$^{17}F(\beta^+\nu)^{17}O$
$^{13}C(p,\gamma)^{14}N$	$^{15}N(p,\gamma)^{16}O$	$^{17}F(\beta^+\nu)^{17}O$	$^{17}O(p,\gamma)^{18}F$
$^{14}N(p,\gamma)^{15}O$	$^{16}O(p,\gamma)^{17}F$	$^{17}O(p,\gamma)^{18}F$	$^{18}F(\beta^+\nu)^{18}O$
$^{15}O(\beta^+\nu)^{15}N$	$^{17}F(\beta^+\nu)^{17}O$	$^{18}F(\beta^+\nu)^{18}O$	$^{18}O(p,\gamma)^{19}F$
$^{15}N(p,\alpha)^{12}C$	$^{17}O(p,\alpha)^{14}N$	$^{18}O(p,\alpha)^{15}N$	$^{19}F(p,\alpha)^{16}O$

TABLE 1.2: List of nuclear reactions involved in the CNO cycles.

shell, caused by further heating from core contraction, results in a dramatic expansion of the star which leaves the main sequence to become a *red giant star*. During the red giant phase the convective hydrogen envelope surrounding the stars expands deep enough to dredge the products of hydrogen burning to the surface in an episode known as *first dredge-up*.

Eventually the core contracts to reach densities high enough to be supported by electron degeneracy pressure. Helium burning will then commence via the triple-alpha process if the core temperature reaches above 0.1 GK. However, under degenerate conditions the additional energy from helium burning does not result in thermal expansion, but rather causes further heating and increases the energy generation rate to result in a *thermonuclear runaway*[1]. The energy produced during the thermonuclear runaway goes into lifting the degenerate conditions in an event known as *the helium flash*, after which core helium burning continues under hydrostatic equilibrium on *the horizontal branch* indicated on Figure 1.9.

Helium burning in stars first takes place via the triple alpha process, whereby three alpha particles are converted into a ^{12}C nucleus. This occurs via a two-step process, first involving two alpha particles fusing to form ^{8}Be, followed by an additional alpha capture: $^{8}Be(\alpha,\gamma)^{12}C$ [4]. The nucleus ^{8}Be is unstable and will decay back to two alpha particles, though eventually there will be a small equilibrium concentration of ^{8}Be. Fred Hoyle pointed out that, in order to produce enough carbon to explain observed abundances, the second step must proceed via a resonant reaction involving an excited state in ^{12}C near 7.7 MeV [5]. This prediction was later confirmed with the discovery of a 0^+ state [6, 7] at an excitation energy of $E_x = 7654.20(15)$ keV [8]. Once the helium has been exhausted in the core the star will again contract, causing core temperatures to rise, until helium burning is ignited in the surrounding shell. Nuclear burning now occurs in two shells: the helium burning shell and the hydrogen burning shell. The star

[1] Stars with initial masses above $2M_\odot$ will reach high enough core temperatures to ignite helium burning before degenerate conditions are reached, and therefore do not exhibit a thermonuclear runaway event at the onset of helium burning

has now entered onto the *asymptotic giant branch*, which will be discussed in more detail in Section 1.2.

1.1.4 End points of stellar evolution

For stars with initial masses above $10M_{\odot}$, helium burning is not the end point of thermonuclear burning. In these stars the ignition of further sequential burning stages can occur in the form of carbon burning, neon burning, oxygen burning and silicon burning. The result is to process CNO material towards the iron peak nuclei on the chart of solar system abundances shown in Figure 1.4. The iron peak nuclei have the greatest binding energy per nucleon and therefore will no longer release energy exothermically via thermonuclear reactions.

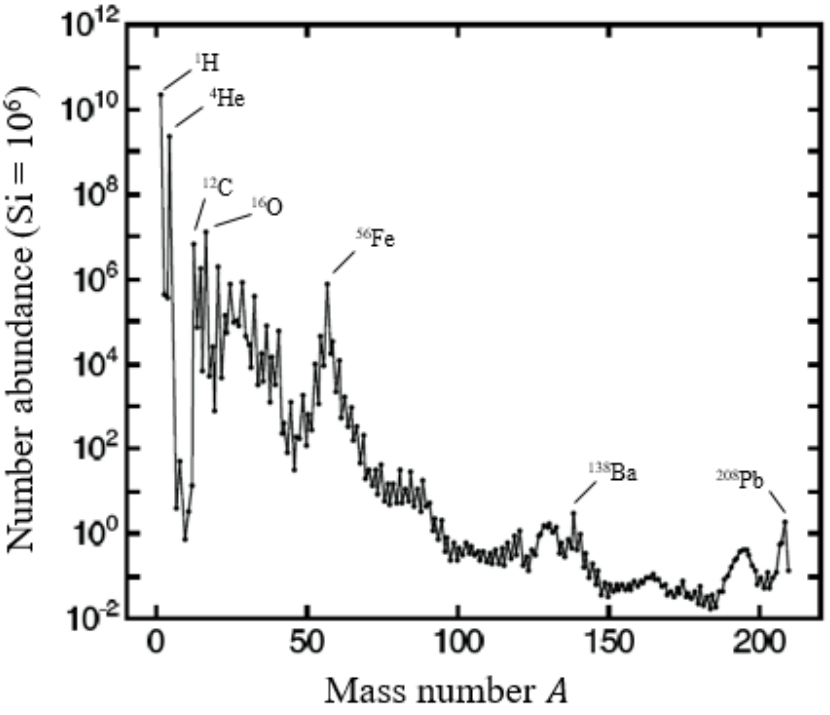

FIGURE 1.4: Chart of solar chemical abundances normalized to Si = 10^6. The local maximum around $A = 50 - 65$ is referred to the *iron peak*. Figure adapted from Ref [2].

Eventually the ashes of advanced burning build up until the core can no longer be supported by electron degeneracy pressure beyond a critical mass of 1.4 $M_{\odot}$. This is known as the Chandrasekhar limit; the maximum mass of a body that can be supported against gravitational collapse by electron degeneracy pressure alone. The core then collapses inwards and copious neutrinos are produced via electron capture reactions. The neutrons produced cannot beta decay since there are no available states for the electrons to emerge in. As the matter in the core reaches nuclear densities, the inward

collapse is abruptly halted by the short range repulsion of the strong nuclear force. The core then 'bounces' to create a shockwave that results in a (Type-II) supernova explosion. These explosions are thought to be a candidate for explaining a significant portion of elemental abundance beyond the iron peak.

1.2 Asymptotic Giant Branch Stars

The asymptotic giant branch (AGB) is a region on the Herzsprung-Russell diagram populated by cool, luminous stars, that have evolved beyond the main sequence. As shown in Figure 1.5, their inert cores are composed of mainly carbon and oxygen, which is surrounded by a helium burning shell. Outside of this is a hydrogen burning shell separated by an inter-shell region consisting primarily of helium. A convective envelope of hydrogen surrounds the star. However, convective transport is prevented from extending down into the products of hydrogen burning by a radiative buffer zone. The canonical description of AGB star evolution outlined herein is adopted from Ref [9].

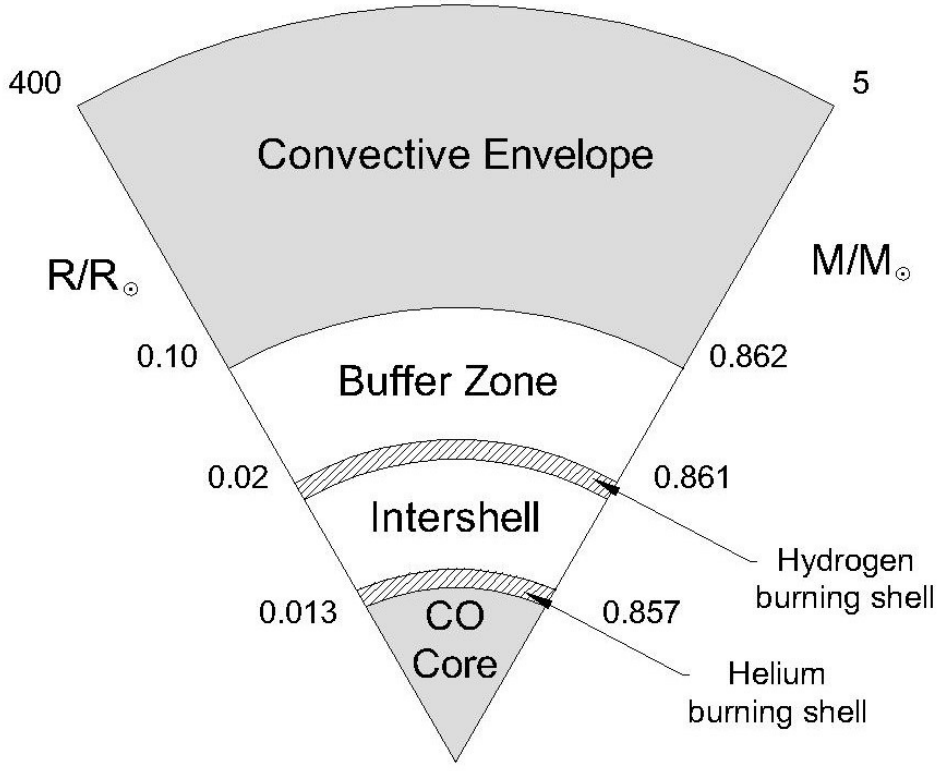

FIGURE 1.5: Diagram showing the internal structure and dimensions of a 5 $M_{\odot}$ AGB star. Figure reproduced from Ref [10].

The time-scales for helium and hydrogen shell burning are not equivalent, and eventually the helium available within its respective burning shell will no longer be sufficient to maintain energy generation. In response, the hydrogen burning shell expands deeper into the star; resulting in rising temperatures, pressures, and helium content, until helium burning can be re-ignited. Once re-ignited, the helium burning shell undergoes a rapid burst of energy output known as a *thermal pulse* (TP). The thermal pulse causes an expansion and cooling of the star until the helium burning shell returns to its initial state. During the thermal pulse the convective envelope extends down into the inter-shell region causing a significant mixing episode termed *third dredge-up*. Further thermal pulses and third dredge-up events are driven by the inherent instability caused by the rapidly burning helium shell vs the slow burning hydrogen shell. The onset of thermal pulses is also characterized by significant mass loss through strong stellar winds, which expel the dredged up products of hydrogen burning into the surrounding interstellar medium (ISM). A schematic representation of the third dredge up episode is shown by Figure 1.7.

1.2.1 Hot Bottom Burning

The base of the convective envelope reaches the hydrogen burning shell during the inter-pulse period in AGB stars. The temperatures reached in the hydrogen burning shell are sufficiently high to allow hydrogen burning on seed nuclei in the $A \geqslant 20$ mass region. The nucleosynthesis that takes place in the context of this environment is termed *hot bottom burning* (HBB). Hydrostatic hydrogen burning beyond mass $A = 20$ does not impact significantly on the energy generated in stellar interiors, though through HBB it does play an important role in terms of nucleosynthesis. In particular the focus here will concern the amount of ^{23}Na produced in this environment, as it is central for understanding the O-Na anti-correlation which will be discussed in the next section.

The most likely reaction pathways for hydrostatic hydrogen burning beyond $A = 20$ are indicated on Figure 1.8. The neon-sodium (NeNa) cycle, highlighted in Figure 1.8, is active during HBB and the reactions contained within it play an important role in the synthesis of ^{23}Na. The NeNa cycle consists of a series of β-decays, (p, γ), and (p, α) reactions, and the competition between these processes will determine the nucleosynthesis pathway at a given temperature. The temperatures reached in HBB (60-100 MK) are not sufficient for reactions on unstable nuclei to play an important role, even considering the relatively long lived isotope ^{22}Na with a half life of $T_{1/2} = 2.6$

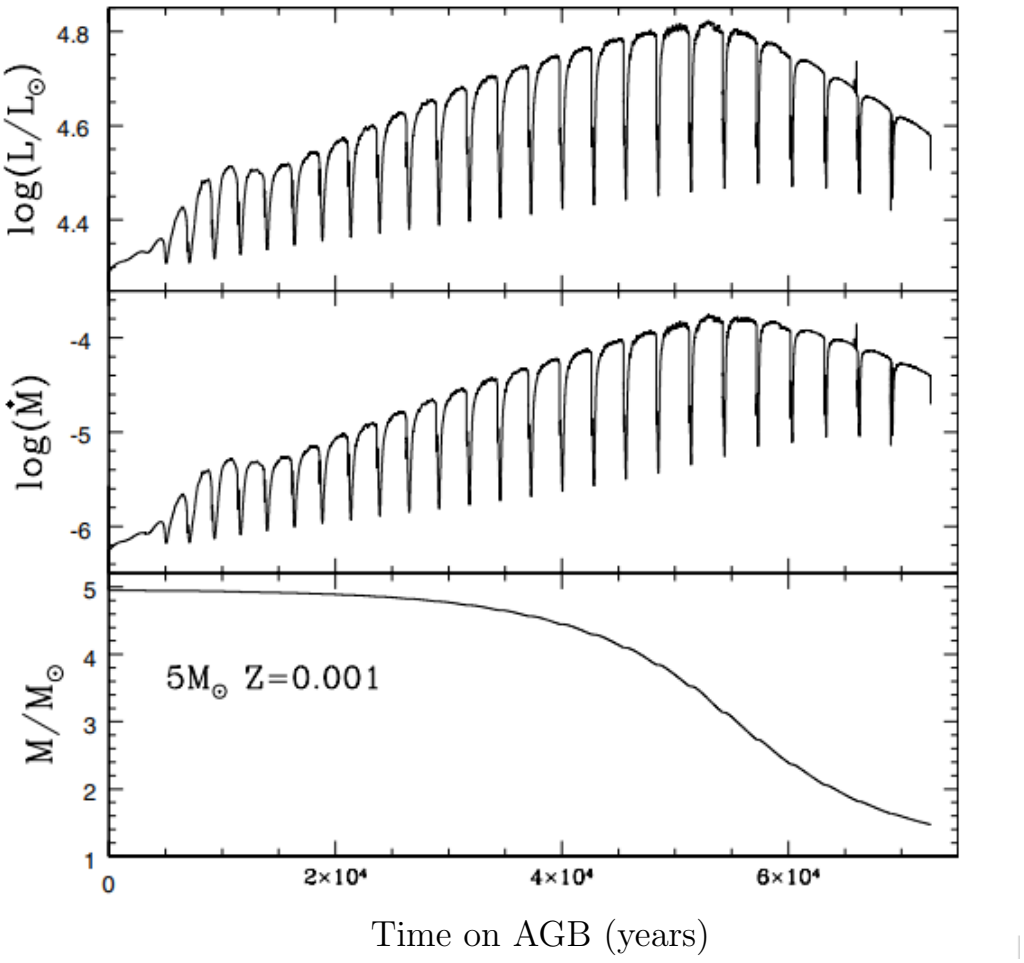

FIGURE 1.6: Graph showing luminosity ($L/L_{\odot}$), mass loss rate $\dot{M}$ in $M_{\odot}$/year, and total mass ($M/M_{\odot}$) as a function of time for a $5M_{\odot}$ star. Time is expressed in years after entering the AGB evolutionary phase. Figure taken from Ref [9].

years. It is also important to note that the NeNa cycle is disconnected from the CNO cycle such that no CNO material can be processed into the $A \geqslant 20$ mass region[1].

The impact of current reaction rate uncertainties in the NeNa cycle were investigated by Izzard *et al.* for AGB stellar models with varying masses and metallicities[2] [11]. The results showed variations of up to two orders of magnitude in ^{23}Na yields, with uncertainties in the $^{22}\mathrm{Ne}(p,\gamma)^{23}\mathrm{Na}$ reaction having the largest impact. Abundance predictions

[1]The $^{19}\mathrm{F}(p,\gamma)^{20}\mathrm{Ne}$ reaction could in principle provide a link between the CNO cycles and NeNa cycle. However, its reaction rate is 3 orders of magnitude smaller than the competing $^{19}\mathrm{F}(p,\alpha)^{16}\mathrm{O}$ reaction at these temperatures.

[2]Metallicity (Z) is defined as the mass fraction of a star attributed to elements heavier than helium. For example, the Sun has a metallicity of $Z = 0.0134$ i.e. the Sun comprises 1.34% elements heavier than helium (metals) by mass.

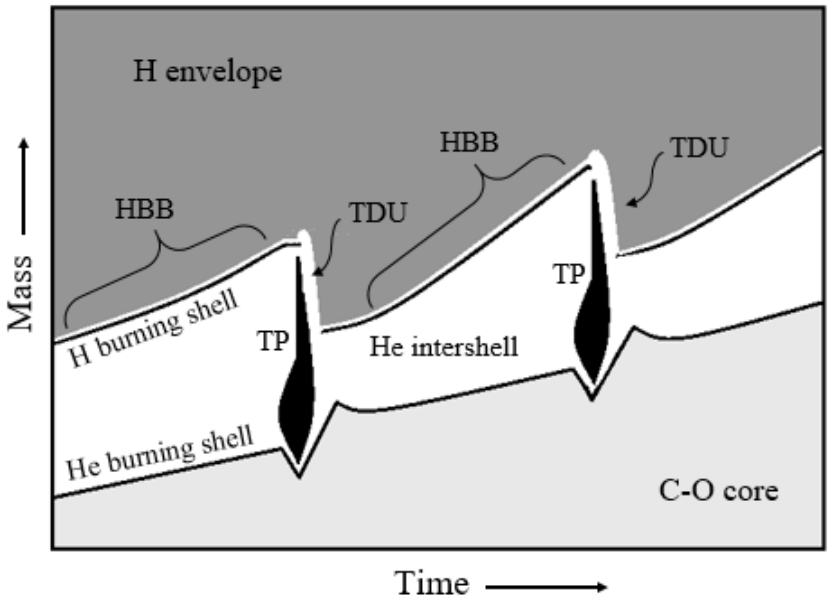

FIGURE 1.7: Schematic of a $M \leqslant 9M_{\odot}$ thermally pulsing AGB star. The convective hydrogen envelope is shown in dark gray, the degenerate C-O core is shown in light gray. The hydrogen and helium burning layers are also shown, the latter being active during the inter-pulse phases where hot bottom burning (HBB) takes place. The helium burning shell periodically ignites a thermal pulse (TP) that extinguishes the hydrogen burning shell by creating a convective region (black) which extends over the entire inter-shell region. The thermal pulses are followed by a mixing episode called third dredge-up (TDU) where the convective envelope reaches into the inter-shell.

for ^{22}Ne, ^{20}Ne, and ^{24}Mg were also affected by varying this reaction rate. The work presented in this thesis aims to experimentally constrain this reaction rate at the relevant temperatures for HBB in AGB stars. A newly obtained reaction rate will then be used in state-of-the-art AGB star model calculations to ascertain the impact on predicted elemental abundances.

1.2.2 The Na-O Anticorrelation in Globular Clusters

Globular clusters (GCs) are dense aggregates of stars that formed in the early universe in regions of space with above average gas density. A comprehensive review of the processes governing the formation of GCs can be found in Ref [12]. Star formation in GCs is thought to be induced in one massive starburst or merger event happening in the early stages of galaxy formation. In these conditions the efficiency of star formation is very high, meaning that these stars are formed very early in the cluster's life, and in a relatively short span of time. As a result some of the oldest observed stars reside in

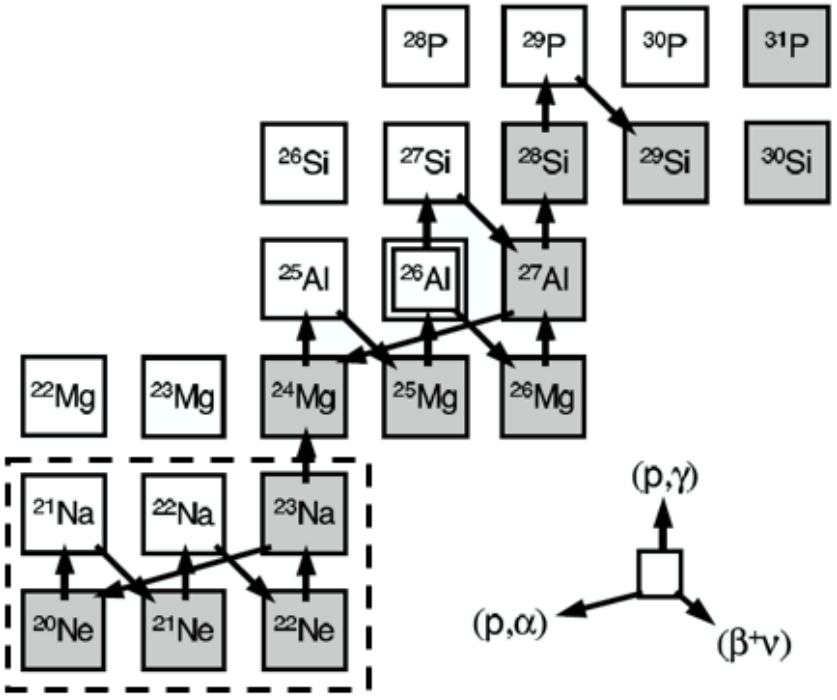

FIGURE 1.8: Diagram of hydrostatic hydrogen burning cycles in the $A \geqslant 20$ mass region. The neon-sodium cycle is highlighted by the dashed box. Stable nuclei are shown in gray and unstable in white. The nuclide ^{26}Al is a special case since it can be formed in its ground state ($T_{1/2} = 7 \times 10^5$ years) or isomeric state ($T_{1/2} = 6$ s). Figure adapted from Ref [2]

globular clusters. The age of these clusters can be estimated by their main sequence turn-off point[1], which also provides a robust lower limit on the age of the universe [13].

The simple picture of a single stellar population makes GCs excellent laboratories to study galactic chemical evolution. However, this paradigm has in recent years been challenged by the observation of multiple stellar populations within a single globular cluster. A prime example is NGC 2808 which has multiple distinct main sequence paths, an unmistakable signature of multiple epochs of star formation (displayed by Figure 1.10).

In addition to observed features on the H-R diagram, globular cluster stars also exhibit abundance correlations indicative of enrichment by previous generations of stars. Some of these abundance correlations are not observed in their field star[2] counterparts, suggesting that the cluster environment itself has a profound effect on chemical evolution. The O-Na anti-correlation is one such abundance pattern that is observed ubiquitously

[1]The main sequence turn-off point is a feature, observed in HR-diagrams of globular clusters, located at the hottest point along the main sequence path (See Figure 1.9). Assuming a single stellar population, stars massive enough to appear on the MS path past this point will have already evolved beyond the MS. As the cluster ages, the turn-off point slides down to cooler and redder portions of the main sequence.

[2]Field stars are individual stars which are not members of any star cluster or association.

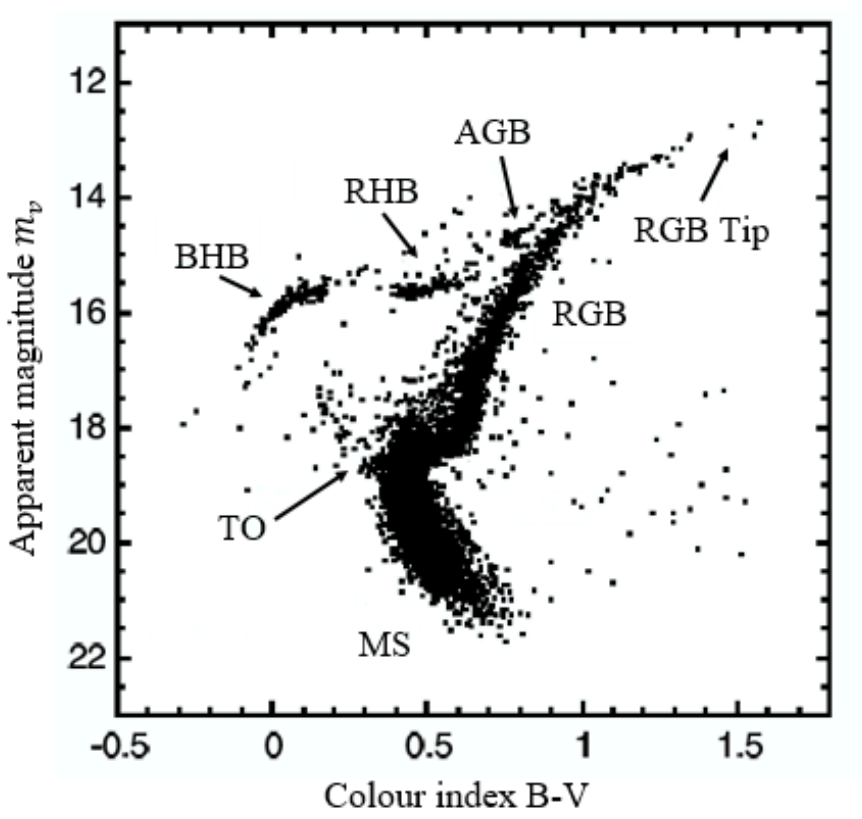

FIGURE 1.9: Hertzsprung-Russell diagram of globular cluster M3. The apparent magnitude is plotted against colour since all the stars can be assumed to have approximately the same distance from earth. The main regions are labelled, including: the main sequence (MS), red giant branch, blue horizontal branch (BHB), red horizontal branch (RHB), asymptotic giant branch (AGB), RGB tip, and the main sequence turn-off point (TO). Figure adapted from Ref [2].

across all well studied globular clusters, as shown in Figure 1.11. The presence of sodium-rich oxygen-poor stars is suggestive of material processed through the complete CNO cycle: at the temperature where this occurs radiative proton capture on ^{22}Ne produces ^{23}Na, forming part of the neon-sodium (NeNa) cycle.

Intriguingly the O-Na anticorrelation is found in relatively un-evolved stars, suggesting that the Na-enriched material must have been delivered via pollution by a more massive previous generations of stars, since unevolved stars could not possibly have the core temperatures needed to initiate the NeNa and MgAl cycles [18, 19]. In addition, the anti-correlation shows no evidence of segregation in particular regions of the red giant branch (RGB). This observed lack of morphology along the RGB would be unexpected if some evolutionary process were at work, for instance extra mixing that might dredge up processed material to the stellar surface [20].

Intermediate mass (3-5 $M_{\odot}$) AGB stars (IM-AGB) that have undergone HBB are generally considered to be the best candidates for polluting globular clusters with Na-rich

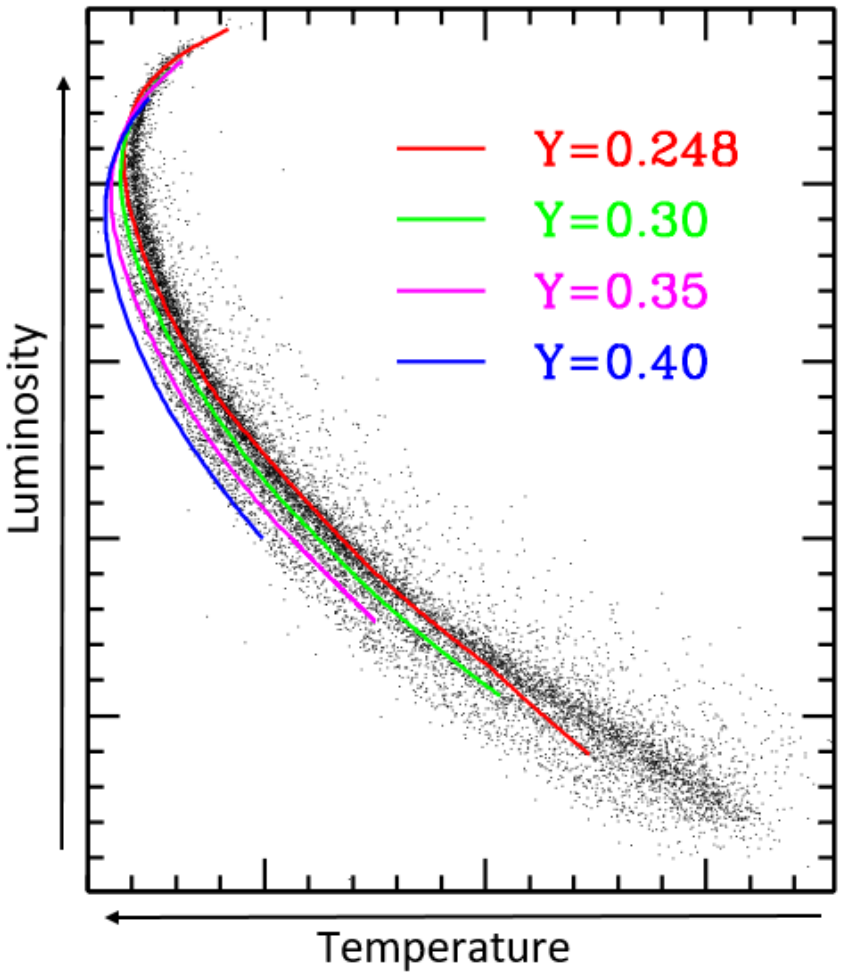

FIGURE 1.10: Colour-Magnitude Diagram of NGC 2808 suggesting the presence of multiple main sequences. These have been fitted with four 12.5 Gyr isochrones, with differing helium content. Figure adapted from Ref [14].

O-poor material; as described by Gratton *et al.* [21]. Their candidacy is not without issues however, as was pointed out by Denissenkov & Herwig *et al.* [22]; at temperatures sufficient to deplete oxygen the sodium will be first produced and then destroyed in the inter-pulse phases. Therefore the final abundances of Na and O will depend quite critically on the interplay of dredge-up, HBB, and mass loss. It is worth pointing out that the treatment of mass loss and the efficiency of convective transport are two of the most uncertain stellar model parameters. Reducing the nuclear physics uncertainties in ^{23}Na production in IM-AGB stars is therefore desirable to constrain yield estimates and model parameters.

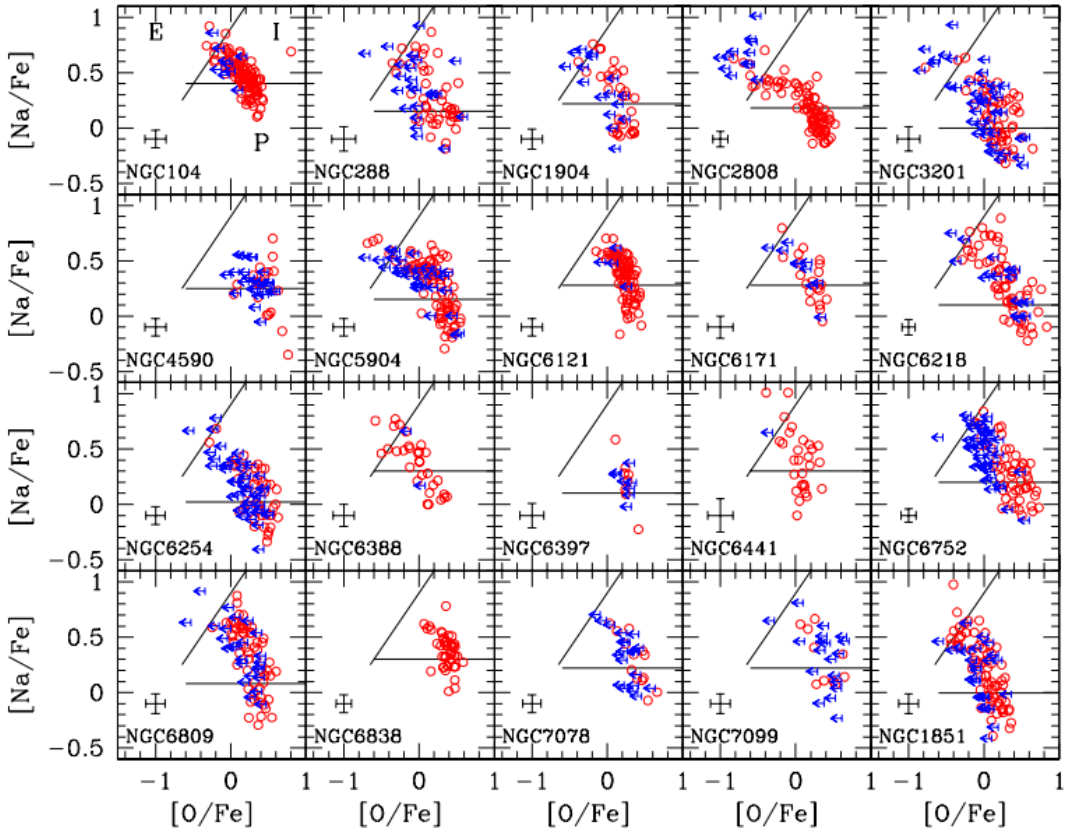

FIGURE 1.11: Abundance plots taken from spectroscopic surveys of 20 globular clusters [15–17]. The bracket notation for the chemical abundances is defined as: $[\mathrm{X/Fe}] = \log[N_\mathrm{X}/N_\mathrm{Fe}]_\mathrm{star} - \log[N_\mathrm{X}/N_\mathrm{Fe}]_\mathrm{sun}$. Where N_X in this case denotes the number density of the elements sodium or oxygen, and N_Fe represents the number density of iron. Red circles indicate results for both sodium and oxygen content, blue lines indicate only upper limits for oxygen. This figure shows that enhanced sodium abundance is observed to be anti-correlated with oxygen in many globular clusters, thereby demonstrating the common nature of this abundance trend.

1.3 Classical Novae

The term nova dates back to the works of renowned Danish astronomer Tycho Brahe, who after observing the supernova of 1572 documented the event in his book "De Nova Stella" (Latin for 'On the New Star'). The term has since been used to describe any bright transient event observed in the night sky, until much later the terms classical nova and supernova were implemented to distinguish between their very different observational characteristics and origins. Though the typical peak luminosity ($10^5 L_\odot$) and mean mass ejection ($2 \times 10^{-5} M_\odot$) for novae do not compare with other more violent explosive events, such as core collapse supernovae and compact object mergers, they are the most frequent with a rate of roughly 50 events per year in the Milky Way according to recent estimates [23]. Consequently, classical novae do contribute to galactic chemical

evolution. In fact classical novae have been proposed as a major source of ^{13}C, ^{17}O, ^{15}N and ^{7}Li [24].

1.3.1 The classical novae progenitor

The progenitor system for novae comprises a white dwarf (WD), with a core consisting mainly of carbon-oxygen (CO) or oxygen-neon (ONe) material, that is accreting matter from a main sequence or red giant companion via Roche lobe overflow [25]. Conservation of angular momentum results in the formation of an accretion disk surrounding the WD. Matter accumulates on the WD surface under degenerate conditions, meaning that rising temperatures are not alleviated by thermal expansion. Instead the temperature continues to rise until a thermonuclear runaway (TNR) occurs, which subsequently lifts the degenerate conditions to result in an explosive outburst. The explosion does not completely destroy the underlying core however, thereby allowing the process to be repeated[1].

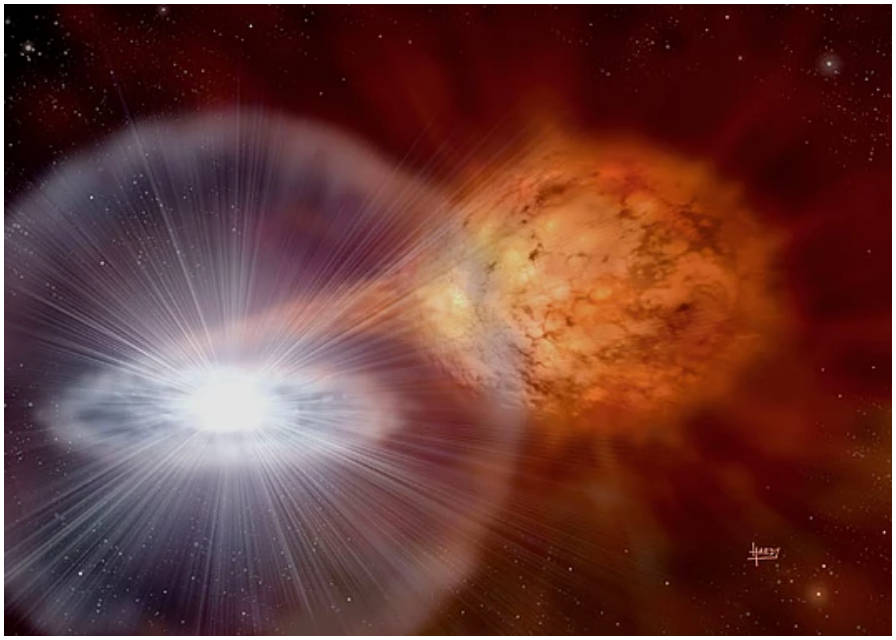

FIGURE 1.12: Artists impression of the recurrent nova RS Ophiuchi, comprising a white dwarf orbiting red giant companion. Figure taken from Ref [27]

1.3.2 Nucleosynthesis in classical novae

Nuclear burning in novae first commences via the p-p chains, and later through the cold-CNO and hot-CNO cycles which constitute most of the energy generation powering the

[1]Typical recurrence times are expected to be 10^4 to 10^5 years, though other objects known as recurrent novae have recurrence rates of only years or decades [26]

HCNO1	HCNO2	HCNO3
$^{12}\mathrm{C}(p,\gamma)^{13}\mathrm{N}$	$^{15}\mathrm{O}(\beta^{+}\nu)^{15}\mathrm{N}$	$^{15}\mathrm{O}(\beta^{+}\nu)^{15}\mathrm{N}$
$^{13}\mathrm{N}(p,\gamma)^{14}\mathrm{O}$	$^{15}\mathrm{N}(p,\gamma)^{16}\mathrm{O}$	$^{15}\mathrm{N}(p,\gamma)^{16}\mathrm{O}$
$^{14}\mathrm{O}(\beta^{+}\nu)^{14}\mathrm{N}$	$^{16}\mathrm{O}(p,\gamma)^{17}\mathrm{F}$	$^{16}\mathrm{O}(p,\gamma)^{17}\mathrm{F}$
$^{14}\mathrm{N}(p,\gamma)^{15}\mathrm{O}$	$^{17}\mathrm{F}(\beta^{+}\nu)^{17}\mathrm{O}$	$^{17}\mathrm{F}(p,\gamma)^{18}\mathrm{Ne}$
$^{15}\mathrm{O}(\beta^{+}\nu)^{15}\mathrm{N}$	$^{17}\mathrm{O}(p,\gamma)^{18}\mathrm{F}$	$^{18}\mathrm{Ne}(\beta^{+}\nu)^{18}\mathrm{F}$
$^{15}\mathrm{N}(p,\alpha)^{12}\mathrm{C}$	$^{18}\mathrm{F}(p,\alpha)^{15}\mathrm{O}$	$^{18}\mathrm{F}(p,\alpha)^{15}\mathrm{O}$

TABLE 1.3: List of nuclear reactions involved in the hot-CNO cycles.

TNR. The HCNO cycles are displayed on Figure 1.13, proceeding through the reactions listed in Table 1.3. Peak temperatures in classical novae can reach upto 400 MK, which is sufficient to process material up to $A = 40$ via proton induced reactions. Though not having a significant impact on the energy generation in classical novae, explosive hydrogen burning beyond $A = 20$ strongly influences the chemical abundances observable in the ejected material. These observed abundances, in both the ejecta and pre-solar grains from novae, provide strong constraints on astrophysical modelling of the explosion because the nuclear reactions responsible for these abundances are highly sensitive to temperature. However, improvements can only be made to stellar models provided that the important nuclear reaction rates are known to a sufficient level of precision. Specific reactions are deemed to be 'important', and therefore warrant further study, if they fulfil two necessary conditions: 1) The reaction must have a significant impact on a stellar property that influences an astronomical observable (e.g., abundances), 2) Changes in the reaction rate within experimental uncertainties must lead to significant variations in that given stellar property.

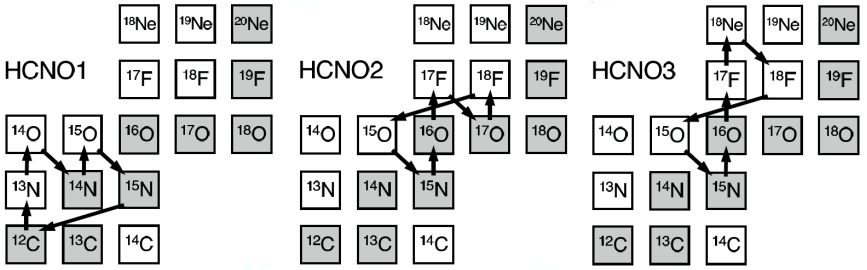

FIGURE 1.13: Diagram of the hot-CNO cycles, with arrows representing the nuclear reactions involved and their direction. Grey boxes indicate stable isotopes and white are radioactive. Figure taken from from Ref [2].

Sensitivity studies are a commonly used method to highlight which nuclear reactions need to be further constrained by experiment. Normally these studies proceed by taking the temperature-density profile generated from a 1D hydrodynamical simulation and then performing reaction network calculations, which involves varying each reaction rate within its respective uncertainties. A draw-back of this approach is that the nuclear reactions are de-coupled from the hydrodynamics, and convective mixing is consequently

ignored. A sensitivity study performed by Iliadis et al. [28] revealed that varying the ^{22}Ne$(p,\gamma)^{23}$Na reaction within its current uncertainties can alter the final abundances of ^{22}Ne by a factor of 100, ^{23}Na by up to a factor of 7, ^{24}Mg by a factor of 5, as well as ^{20}Ne, ^{21}Ne, ^{25}Mg, ^{26}Mg, ^{26}Al and ^{27}Al by at least a factor of 2 each. Therefore improved knowledge of this reaction rate within the relevant temperature ranges would be extremely beneficial in order to further constrain abundance predictions from nova models.

Chapter 2

Theory

2.1 Nuclear reactions

Thermonuclear reactions are the engines that allow stars to shine and drive the chemical evolution of the cosmos. Once an important reaction has been identified, the task of the experimental nuclear astrophysicist is then to characterize the rate at which such a reaction will proceed under the relevant astrophysical conditions. The direct approach to achieving this is to replicate as closely as possible, under experimentally controlled conditions, the collision of two nuclei at appropriately chosen energies. This chapter will begin by defining the reaction cross section, which contains the nuclear physics input to reaction rates. Then the concept of resonances will be introduced, along with how their characteristics can be measured in the lab. The latter half of this chapter will then focus on describing how astrophysical rates can be calculated from measurable nuclear properties.

2.1.1 Reaction cross sections

The cross section of a particular nuclear reaction is a quantity that measures the probability that the reaction will occur. This is defined below in terms of the number of reactions (N_R) occurring as a function of: the total number of incident beam ions (N_b), the area density of the target (N_t/A), and the cross section (σ).

$$\frac{N_R}{t} = \frac{N_b}{t}\frac{N_t}{A}\sigma \tag{2.1}$$

From Equation 2.1 it is clear to see that the cross section has units of area, and can classically be thought of as analogous to the geometric cross section of the interacting

nuclei. In fact cross sections are expressed in units of *barns* ($10^{-28}\ m^2$), which is approximately equal to the area profile of a uranium nucleus. However, given that the cross section can differ significantly from the classical area of the reactant nuclei, it is best to stick with the previously outlined definition of an *interaction probability*.

2.1.2 Penetrability

The potential inside the nucleus can be roughly approximated by a finite spherical well potential. The amplitude of an incident particle's wave function inside the nuclear interior is strongly perturbed if the nuclear potential is surrounded by a repulsive potential-barrier. In the case of charged particles the shape of the barrier is described by the Coulomb potential, ignoring the possible transfer of angular momentum which will be discussed at the end of this section. For a particle to appear inside the nuclear interior it must tunnel through the repulsive barrier. In order to derive the penetrability through this potential barrier it is easier to first consider the simplified case of transmission through a rectangular-barrier potential of height V_0. In the limit where the barrier thickness δr is small, the transmission probability of an incident particle of kinetic energy E will be approximately given by:

$$\hat{T} \approx \exp\left(-\frac{2}{\hbar}\sqrt{2m(V_0 - E)}\delta r \right) \tag{2.2}$$

Equation 2.2 can be used to describe any potential-barrier shape, by dividing an arbitrary barrier into n infinitesimally small slices i of width dr. The total transmission is then given by the product of the all the transmission coefficients for each slice:

$$\hat{T} = \prod_{i}^{n} \hat{T}_i \tag{2.3}$$

In the limit where n is large, this can be written as:

$$\hat{T} \approx \exp\left(-\frac{2}{\hbar}\sum_{i} \sqrt{2m(V_i - E)}(r_{i+1} - r_i) \right) \tag{2.4}$$

For the case of the Coulomb potential, Equation 2.4 becomes:

$$\hat{T} \approx \exp\left(-\frac{2}{\hbar}\sqrt{2m}\int_{R_0}^{R_c} \sqrt{\frac{Z_0 Z_1 e^2}{r} - E}\ dr \right) \tag{2.5}$$

Where Z_0 and Z_1 are the charge of the target and projectile respectively. The lower limit of the integral (R_0) is the radius of the spherical-well potential and so defines the height of the Coulomb barrier, $V_C = Z_0 Z_1 e^2/R_0$. This can be numerically expressed as $V_C = 1.44 Z_0 Z_1/R_0$ (MeV), with R_0 in units of femto-meters. R_c is the *classical turning point*, which refers to the radius at which the energy of the incoming particle matches that of the barrier potential, $E = Z_0 Z_1 e^2/R_c$. Figure 2.1 shows an attractive finite spherical well potential plus a repulsive Coulomb barrier. The area under the Coulomb barrier is divided into many thin rectangular-barrier potentials. The total transmission probability for an incident particle of energy E must therefore be the probability of tunnelling through all the barriers integrated between the classical turning point and the spherical-well radius.

Using the definition of the classical turning point, Equation 2.5 can be solved analytically to find the Gamow factor:

$$\hat{T} \approx \exp\left(-\frac{2\pi}{\hbar}\sqrt{\frac{m}{2E}} Z_0 Z_1 e^2 \right) \equiv e^{-2\pi\eta} \tag{2.6}$$

The quantity η is referred to as the *Sommerfeld parameter*. Using the above definition for the Gamow factor, one may conveniently express the dependence of the cross section on the Coulomb penetrability to define the *astrophysical S-factor*, S(E).

$$\sigma(E) \equiv \frac{1}{E} e^{-2\pi\eta} S(E) \tag{2.7}$$

The definition of the astrophysical S-factor factors out the main sources of energy dependence contained within the nuclear cross section. The 1/E factor accounts for the cross section dependence on the de Broglie wavelength, while the Gamow factor separates the penetrability through the Coulomb barrier in the case of head-on collisions i.e. collisions that transfer no orbital angular momentum (l) and are thus defined as $l = 0$ or 's-wave'. Though it's of course possible to transfer orbital angular momentum during the course of a reaction, larger angular momentum transfers are hindered by a centrifugal barrier through which an incoming projectile must tunnel. The penetrability of charged particles through the Coulomb barrier with arbitrary angular momentum will not be explicitly dealt with here, though it is worth mentioning that this problem can only be solved numerically - for which existing codes are available.

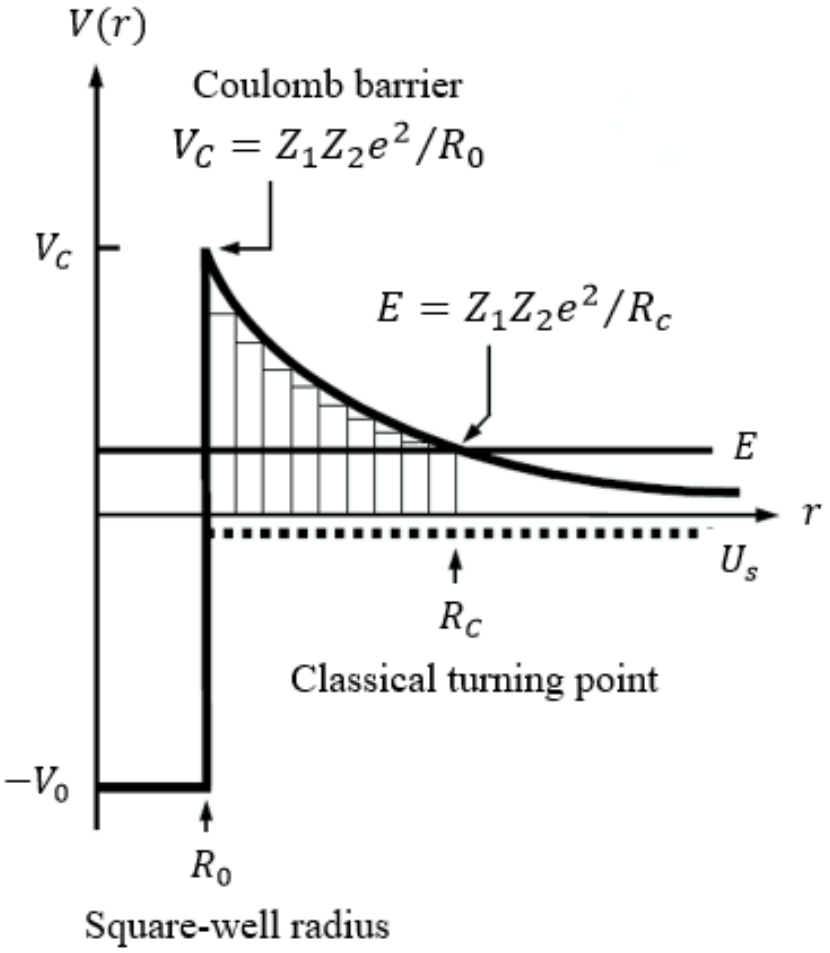

FIGURE 2.1: Diagram of a square well potential of radius R_0 plus Coulomb potential of height V_c. The Coulomb barrier between the classical turning point and the square-well radius has been split into many square-barrier potentials as shown. Figure reproduced from Ref [2].

2.1.3 Resonances

The previous section describes the smoothly varying probability that an incoming particle will tunnel through the Coulomb barrier. However, the reaction cross section does not always vary smoothly with energy, and resonant phenomena can occur at particular energies. These resonances are sharp variations in the reaction cross section as a function of energy, occurring when the probability density of an incident particle's wave function is maximised within the nuclear interior due to significant overlap between the initial and final states of the reaction. The Hamiltonian describing a proton incident upon a stationary target nucleus can be written as follows:

$$H = H_t + E_p + \sum_{i=1}^{A} V_i(\vec{r}_i) \tag{2.8}$$

Where H_t is the Hamiltonian of the target nucleus composed of A nucleons, E_p is the incident proton energy, and the last term is the sum of all interaction potentials $V_i(\vec{r}_i)$ experienced by the incoming proton from each individual nucleon of the target. This last term is extremely complex and considerable theoretical efforts are aimed at attempts to describe the potential resulting from interactions between individual nucleons. In light of this, the situation can be simplified by introducing an average potential $\bar{V}(r)$.

$$H = [H_t + E_p + \bar{V}(r)] + \left[-\bar{V}(r) + \sum_{i=1}^{A} V_i(\vec{r}_i) \right] = H_0 + H' \tag{2.9}$$

Where H_0 is the *single-particle* Hamiltonian, and any deviations from the average potential are absorbed within the *residual interaction* Hamiltonian H'. The single particle Hamiltonian gives rise to periodic rises in the cross section called *single particle resonances*. These resonances arise due to favourable boundary matching conditions, whereby the single-particle wave function probability density is maximised within the nuclear interior. Single particle resonances are typically broad and spaced apart by one or more MeV, however experimental studies reveal the presence of many narrow resonances which are spaced far more closely together (in some cases only a few keV); clearly the single-particle picture of the nucleus-projectile system cannot describe these resonances.

The residual Hamiltonian H' causes a splitting of the single particles states described by H_0 into many *virtual states*, each of which correspond to a complicated mixture of nucleon configurations and summed single-particle wave functions. The boundary matching conditions for the radial wave function will consequently differ for each of these virtual states, thereby giving rise to their own set of resonances. Theses resonance are treated by considering an intermediate projectile-target system called *the compound nucleus*, which subsequently decays into the final state of the reaction.

Resonances arising from compound nuclear levels are each described by a set of properties: a resonance energy (E_r), a spin adn parity (J^π), a lifetime (τ), and a set of branching ratios (B_i) to each possible decay channel. The life time τ is the inverse of the decay rate of the state and is related to the *total width* (Γ) of the state by: $\Gamma = \hbar/\tau$. The width of any given branch is called a *partial width*, and is related to the total width via its branching ratio defined by $B_i = \Gamma_i/\Gamma$.

The resonance width is given by the product of three factors. The first factor is the penetrability P_l, which describes the probability of a particle being emitted from a resonance by tunnelling through the Coulomb and/or angular momentum barrier. This has already been outlined for the case of an s-wave proton in Section 2.1.2. The spectroscopic factor

(S) is the next quantity to consider. This is the probability that nucleons will arrange themselves into a final state well described by a core plus a single particle. Spectroscopic factors are often calculated using the nuclear shell model. Finally, the width also scales with the probability that the single particle will appear at the boundary of the nucleus. This is a dimensionless quantity called the single-particle reduced width, θ_{sp}^2. Together, these factors give the partial width computed for a specific reaction channel:

$$\Gamma_i = \frac{2\hbar}{\mu R^2} P_l C^2 S_i \theta_{sp}^2 \tag{2.10}$$

Where $\hbar$ is the reduced Plank's constant, μ is the reduced mass, R is the channel radius at which the probability of finding the single particle is computed to give θ_{sp}^2, and the quantity C^2 is the square of an isospin Clebsch-Gordon coefficient which gives the probability that the compound state is described by a particular angular momentum and m-state coupling between the reactant particles [29], tables of which can be found in Ref [30].

The profile of the cross sections close to a narrow resonance with energy E_r is well described by the single channel Breit-Wigner formula:

$$\sigma_{if}(E) = \frac{\lambda^2}{4\pi} \frac{(2J+1)}{(j_a+1)(j_b+1)} (1+\delta_{ab}) \frac{\Gamma_i \Gamma_f}{(E-E_r)^2 + \frac{\Gamma^2}{4}} \tag{2.11}$$

Where i and f are the incoming and outgoing channels, λ is the de Broglie wavelength, j_a and j_b are the spins of the projectile and target, J is the spin of the compound nucleus level. The Kronecker delta δ_{ab} applies a factor of two multiplication if the two reactants are identical.

The resonance strength is proportional to the maximum cross section and the resonance width, and is defined below as:

$$\omega\gamma = \frac{2J+1}{(2j_a+1)(2j_b+1)} \frac{\Gamma_i \Gamma_j}{\Gamma} \tag{2.12}$$

The above equation is employed if one is required to deduce the resonance strength from the nuclear properties of a particular resonance. This practise is contained under the generalized umbrella of *indirect methods*, however the results presented in this thesis are obtained via *direct methods*, from which *absolute resonance strengths*[1] are measured.

[1] Absolute resonance strength measurements are those which do not rely upon normalization to another well-known resonance strength; these are called relative measurements and will not be formalized here since all the strengths presented in this work were measured in an absolute fashion.

The next section will apply the Breit-Wigner formulation of resonances with reaction cross sections measured in the lab.

2.1.4 Reaction Yields

The yield for a reaction measured in the lab is simply the total number of detected products (N_r), accounting for detection efficiency (η), divided by the total number of incident beam ions (N_b). This is given by Equation 4.2 below as:

$$Y = \frac{N_r}{N_b \eta} \tag{2.13}$$

Combining Equations 2.1 and 2.13 gives the yield over an infinitesimal target length Δx.

$$Y = \sigma \frac{N_t}{A} = \sigma n \Delta x \tag{2.14}$$

Where $n = \frac{N_t}{V}$ is the number of target atoms per unit volume. Suppose that the target is divided into infinitesimal slices Δx_i, then the yield from a given slice i would be Y_i. Given that each slice is infinitesimally thin, it can be assumed that the energy lost by the beam is small and therefore the cross section is constant over each slice. The total yield is then found by integrating the yield of each slice over the total target thickness.

$$Y = \int \sigma(x) N(x)\, dx = \int \sigma(x) N(x)\, dx \frac{dE(x)}{dx} \frac{dx}{dE(x)} \tag{2.15}$$

Where $N(x)$ is the target number density as a function of depth. The rate at which the beam loses energy over the target is referred to as the stopping power, and is defined as:

$$\epsilon(E) = -\frac{1}{N(x)} \frac{dE}{dx} \tag{2.16}$$

Substituting into Equation 2.15 gives:

$$Y = \int_{E_0 - \Delta E}^{E_0} \frac{\sigma(E)}{\epsilon(E)}\, dE \tag{2.17}$$

Where ΔE is the total energy loss across the target. If the variation in cross section with energy is prescribed by the Breit-Wigner formula, then by substituting Equation 2.12, the narrow resonance yield is obtained as [31]:

$$Y = \frac{\lambda^2(E_r)}{2\pi}\frac{\omega\gamma}{\epsilon(E_r)}\frac{\Gamma}{2}\int_{E_0-\Delta E}^{E_0}\frac{dE}{(E_r-E)^2+(\Gamma(E)/2)^2} \tag{2.18}$$

Assuming that the stopping power and de Broglie wavelength remain constant over the energy range covered by the target, then Equation 2.18 can be solved analytically to give [2]:

$$Y = \frac{\lambda^2(E_r)}{2\pi}\frac{\omega\gamma}{\epsilon(E_r)}\left[\arctan\left(\frac{E_0-E_r}{\Gamma^2}\right)-\arctan\left(\frac{E_0-E_r-\Delta E}{\Gamma^2}\right)\right] \tag{2.19}$$

For a target thick enough to contain essentially the whole energy profile of a resonance, Equation 2.19 will reduce to the maximum yield as [2]:

$$Y = \frac{\lambda(E_r)^2}{2}\frac{\omega\gamma}{\epsilon(E_r)} \tag{2.20}$$

Since stopping powers are measured in the lab frame, Equation 2.21 can be expressed as:

$$Y = \frac{\lambda(E_r)^2}{2}\frac{\omega\gamma}{\epsilon}\frac{m_t+m_p}{m_t} \tag{2.21}$$

Where m_t and m_p are the masses of the the target and projectile respectively in u. The thick target yield quoted above is used to calculate resonance strengths from DRAGON experiments.

2.2 Astrophysical reaction rates

The quantity needed for astrophysical model calculations is the number of reactions occurring per unit volume per unit time. Utilizing the previously outlined definition of the reaction cross section given in Equation 2.1, the reaction rate can therefore be written as:

$$\frac{N_R}{V\cdot t} = \sigma(v)\frac{N_t}{V}\frac{N_b}{A\cdot t} = \sigma(v)\frac{N_t}{V}v\frac{N_b}{V} \tag{2.22}$$

With the current density (number of beam particles N_b passing through an area A per unit time t) given by: $j_b = N_b/(At) = vN_b/V$ where v is the relative velocity between the beam and target.

Consider a reaction between two distinct particles, labelled 0 and 1. The reaction rate per particle pair can then be expressed as

$$r_{01} = N_0 N_1 v\sigma(v) \tag{2.23}$$

The relative velocity (ν) between particles 0 and 1 is not constant in astrophysical environments, but rather a distribution of velocities and will have an associated probability distribution, $P(v)$. Since the relative velocity is finite, we have:

$$\int_0^\infty P(v)\, dv = 1 \tag{2.24}$$

With the above definition of the probability distribution, the thermally averaged reaction rate per particle pair can be generalized in the form:

$$r_{01} = N_0 N_1 \int_0^\infty v P(v) \sigma v\, dv \equiv \frac{N_0 N_1 \langle \sigma v \rangle_{01}}{(1+\delta_{01})} \tag{2.25}$$

The final term $\langle \sigma v \rangle_{01}$ is where the nuclear physics is contained, though it is common to multiply reaction rates by Avogadro's number (N_A), and report them in units of $\mathrm{cm}^3\mathrm{mol}^{-1}\mathrm{s}^{-1}$.

In stellar plasmas the velocity distribution is attributed to the thermal motion of the constituent ions, hence the term *thermonuclear reaction rate*. There are a few exceptions, but in most cases the velocity distribution in stellar plasmas is well described by the Maxwell-Boltzmann distribution whereby the nuclei move non-relativistically under non-degenerate conditions. Provided that the reactant species are in thermal equilibrium with one-another, the relative velocities between them will also be Maxwellian [32]. The Maxwell-Boltzmann distribution is given as:

$$P(v)\, dv = \left(\frac{m_{01}}{2\pi k T}\right)^{3/2} e^{-m_{01}v^2/(2kT)} 4\pi v^2\, dv \tag{2.26}$$

Where the Boltzmann constant $k = 8.6173 \times 10^{-5}$ eV/K, T is the temperature, and m_{01} is the reduced mass given by $m_{01} = m_0 m_1/(m_0 + m_1)$. With $E = m_{01}v^2/2$ and $dE/dv = m_{01}v$, the velocity distribution can instead be expressed as an energy distribution.

$$P(E)dE = \frac{2}{\sqrt{\pi}} \frac{1}{(kT)^{3/2}} \sqrt{E}\, e^{-E/kT}\, dE \tag{2.27}$$

The thermally averaged reaction rate per particle pair can now be expressed as a function of energy:

$$\begin{aligned}\langle \sigma v \rangle_{01} &= \int_0^\infty vP(E)\sigma(E)dE \\ &= \left(\frac{8}{\pi m_{01}}\right)^{1/2} \frac{1}{(kT)^{3/2}} \int_0^\infty E\sigma(E)\, e^{-E/kT}\, dE \end{aligned} \tag{2.28}$$

Numerically the thermonuclear reaction rate at a given temperature is obtained as:

$$N_A\langle \sigma v \rangle_{01} = \frac{3.7318 \times 10^{10}}{T_9^{3/2}} \sqrt{\frac{M_0 + M_1}{M_0 M_1}} \int_0^\infty E\sigma(E)\, e^{-11.605E/T_9}\, dE \tag{2.29}$$

Where the centre of mass energy E is given in units of MeV, the temperature is in GK ($T_9 \equiv T/10^9 K$), the masses of particles 0 and 1 in u, and the cross section in barns ($1\text{b} \equiv 10^{-24}$ cm^2).

2.2.1 The Gamow window

The energy at which most reactions will occur at within a stellar plasma depends on the interplay between the thermal distribution of the constituent nuclei, and the penetrability associated with the specific reaction being considered. While the penetrability for a given reaction will increase with energy, the number of particles with a high enough energy to overcome the Coulomb barrier will be in general small. Conversely, there will be a relatively large number of particles with energies that are simply too low to contribute in any meaningful way to the total reaction rate. The goldilocks zone between these two factors is called the Gamow window, which defines the energy regime where non-resonant reactions are most likely to occur. Resonant reaction rates will be treated in Section 2.2.3.

Taking the previously outlined definition of the S-factor given by Equation 2.7, and substituting into Equation 2.28 allows one to write the thermonuclear reaction rate as:

$$N_A\langle \sigma v \rangle_{01} = \left(\frac{8}{\pi m_{01}}\right)^{1/2} \frac{N_A}{(kT)^{3/2}} \int_0^\infty S(E)\, e^{-2\pi\eta}\, e^{-E/kT}\, dE \tag{2.30}$$

Figure 2.2 shows the competing $e^{-E/kT}$ and $e^{-2\pi\eta}$ terms as a function of energy for the ^{22}Ne$(p,\gamma)^{23}$Na reaction at a temperature of 0.2 GK. By plotting the product of these

two factors on a linear scale, the Gamow window is shown to bear a striking resemblance to a Gaussian distribution. The maximum and width of the Gamow peak, the latter found by approximation to a Gaussian, can be calculated numerically by [2]:

$$E_0 = 0.1220\left(Z_0^2 Z_1^2 \frac{M_0 M_1}{M_0 + M_1} T_9^2\right)^{1/3} \quad \text{(MeV)} \tag{2.31}$$

$$\Delta = 0.2368\left(Z_0^2 Z_1^2 \frac{M_0 M_1}{M_0 + M_1} T_9^5\right)^{1/6} \quad \text{(MeV)} \tag{2.32}$$

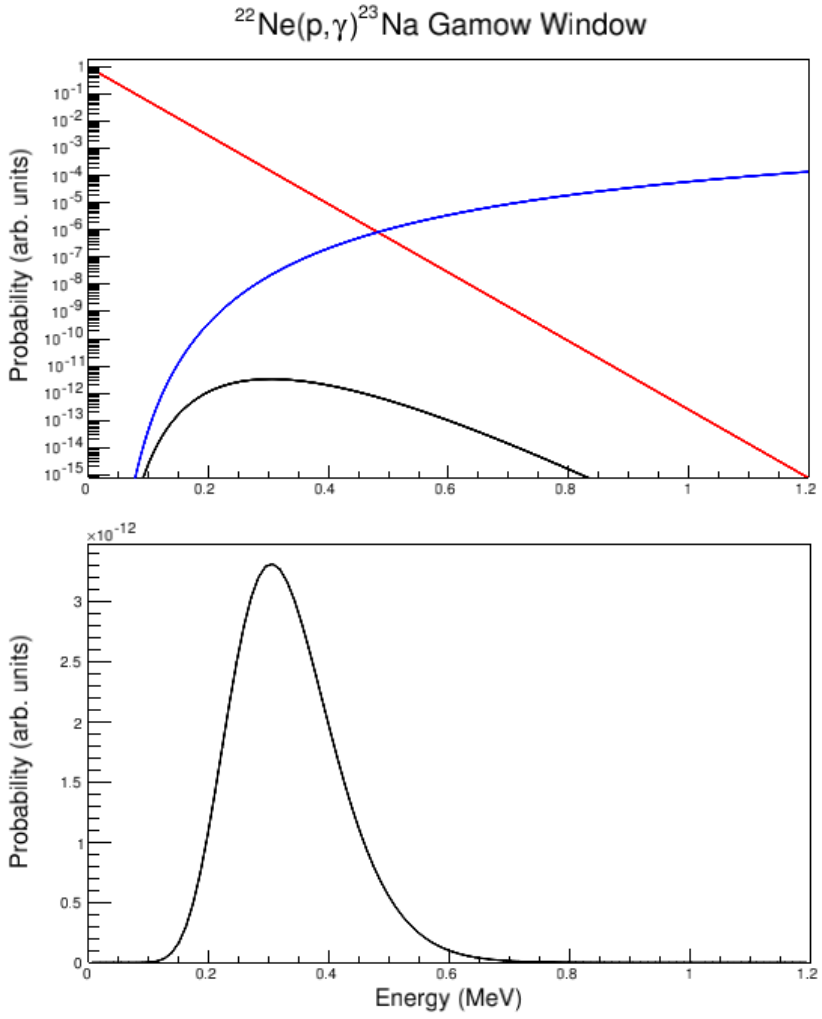

FIGURE 2.2: The top panel shows the Maxwell-Boltzman factor ($e^{-E/kT}$; red) and the Gamow factor ($e^{-2\pi\eta}$; blue) for the ^{22}Ne$(p,\gamma)^{23}$Na reaction at a temperature of 0.4 GK. The product of the two factors gives the Gamow peak indicated by the black line, shown on both log (top) and linear (bottom) scales. The Gamow peak is centred at 0.304 MeV and has a $1/e$ width $\Delta = 0.236$ MeV

2.2.2 Non-resonant reaction rates

The previous section introduced the concept of the Gamow window, which describes the dependence of the reaction rate on temperature and the S-wave penetrability through the Coulomb barrier, but neglects other aspects that influence the nuclear cross section contained in the astrophysical S-factor. If the astrophysical S-factor remains constant as a function of energy, then the S-factor can simply be taken outside of the integrand in Equation 2.30 to give:

$$N_A\langle\sigma v\rangle_{01} = \left(\frac{8}{\pi m_{01}}\right)^{1/2} \frac{N_A}{(kT)^{3/2}} S_0 \int_0^\infty e^{-2\pi\eta}\, e^{-E/kT}\, dE \tag{2.33}$$

A constant S-factor would arise in cases where only the tails of distant resonances contribute to the reaction rate. In this situation the reaction mechanism is dominated by the *direct capture* process. A complete description of the direct capture model of nuclear reactions is beyond the scope of this thesis. Instead the focus here shall remain with describing the influence of constant or smoothly varying S-factors upon the reaction rate. In cases where the S-factor is not constant, but varies smoothly with energy, the S-factor can be expanded into a Taylor series about $E = 0$ as follows:

$$S(E) \approx S(0) + S'(0)E + \frac{1}{2}S''(0)E^2 + \ldots \tag{2.34}$$

Where the primes denote derivatives with respect to energy E. Substituting the above Taylor expansion into the thermonuclear rate leads to a sum of integrals which can be solved analytically to give [33]:

$$N_A\langle\sigma v\rangle_{01} = \frac{1}{3}\left(\frac{4}{3}\right)^{3/2} \frac{\hbar}{\pi} \frac{N_A}{m_{01} Z_0 Z_1 e^2} S_{\text{eff}} \tau^2\, e^{-\tau} \tag{2.35}$$

Where the constant S-factor has now been replaced with an effective S-factor (S_{eff}) defined as [33]:

$$S_{\text{eff}}(E_0) = S(0)\left[1 + \frac{5}{12\tau} + \frac{S'(0)}{S(0)}\left(E_0 + \frac{35}{36}kT\right) + \frac{1}{2}\frac{S''(0)}{S(0)}\left(E_0^2 + \frac{89}{36}E_0 kT\right)\right] \tag{2.36}$$

Where $\tau \equiv 3E_0/(kT)$ and E_0 is the peak of the reaction rate given by Equation 2.31. The first two terms in the square bracket correct for the asymmetry of the Gamow peak,

which is approximated by a symmetrical Gaussian, and the latter terms correct for the varriation of the S-factor with energy. The reaction rate can be numerically calculated with a temperature power law derived in Ref [34], which will not be explicitly written here.

2.2.3 Resonant reaction rates

As described in Section 2.1.3 a reaction may proceed via a narrow resonance, whereby a compound nuclear state gives rise to a dramatic enhancement in the cross section over a narrow energy range. Substituting the Breit-Wigner cross section (Equation 2.11) into the thermonuclear rate gives the resonant reaction rate as follows:

$$N_A\langle\sigma v\rangle = \sqrt{2\pi}\frac{N_A\omega\hbar^2}{(\mu kT)^{3/2}}\int_0^\infty e^{-E/kT}\frac{\Gamma_i(E)\Gamma_f(E+Q-E_f)}{(E_r-E)^2+\Gamma(E)^2/4}\,dE \tag{2.37}$$

Where the partial width of the outgoing channel Γ_f is a function of the energy available to the reaction products; calculated by the sum of the initial energy E and the reaction Q-value minus the excitation energy of the final state E_f into which the resonance transitions. If there is more than one possible final state into which the resonance can decay, their individual contributions to the total reaction rate will add incoherently.

For isolated narrow resonances their contribution to the total reaction rate does not depend significantly upon the exact shape of the cross section within the Gamow window. Resonances are considered to be narrow if the Maxwell-Boltzmann factor and partial widths are approximately constant over the total width of the resonance. Isolated simply means that the nuclear level density of the compound nucleus is low enough that adjacent resonances with the same quantum numbers do not overlap significantly in energy. In this case the reaction rate owing to a specific resonance depends only upon its associated energy and strength, and the contribution of many resonances will add incoherently to give the total rate.

The total rate flowing through several isolated narrow resonances can be calculated numerically using Equation 2.38

$$N_A\langle\sigma v\rangle = \frac{1.5399\times10^{11}}{(\mu T_9)^{3/2}}\sum_i(\omega\gamma)_i e^{-11.605E_i/T_9}\quad(\mathrm{cm^3mol^{-1}s^{-1}}) \tag{2.38}$$

Where $(\omega\gamma)_i$ and E_i are the strength and energy of the i^{th} resonance in units of eV and MeV respectively. This simplified dependence of the total reaction rate on the

characteristics of narrow resonances ought to be emphasized in the context of this thesis, since the aforementioned properties are precisely the nuclear physics observables that the DRAGON experiment is designed to measure. Though it should also be noted that Equation 2.38 will not hold if a resonance is broad and therefore the shape of the resonant cross section becomes important to consider. In such cases the reaction rate will need to be evaluated via numerical integration of Equation 2.37.

Chapter 3

Experimental Considerations

3.1 TRIUMF

The TRIUMF[1] facility located in Vancouver is Canada's national laboratory for nuclear and particle physics research and can be considered as being amongst the world leading facilities in experimental nuclear science. All of the experimental work presented in this thesis was conducted at the TRIUMF facility, utilizing the lab's flagship program of producing stable and radioactive ion beams in order to investigate the properties of atomic nuclei. The production of ion beams in the lab is a vastly complex field of active research, and so a complete presentation of the physics surrounding this multifaceted topic is beyond the scope of this thesis. However, this section will aim to give a brief overview of the core principles used to generate ion beams at TRIUMF, and introduce the relevant key pieces of equipment used to do this.

3.1.1 The ISOL technique

The TRIUMF Isotope Separator and Accelerator (ISAC) facility is among a select few places world-wide capable of producing radioactive ion beams (RIBs). Several methods exist for producing radioactive beams for use in experimental nuclear physics, see Refs. [35, 36] and references therein, though the *isotope separator online (ISOL) technique* is the method used at TRIUMF. The ISOL technique involves firing a primary beam of light projectile nuclei at a thick target composed of nuclei with greater atomic number (Z). At high enough energies the projectiles induce breakup of the target nuclei into lower mass fragments, which can then be subsequently extracted and accelerated towards experiment areas for study.

[1] Originally TRIUMF stood for TRI-University Meson Facility but the acronym has since been discontinued given that the lab is now supported by a consortium of 19 Canadian universities

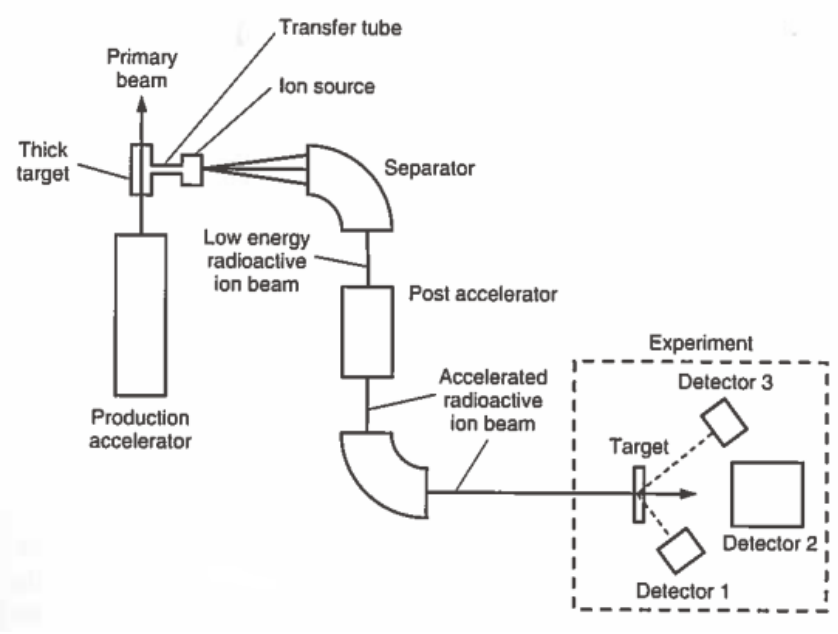

FIGURE 3.1: Basic components of an isotope separator online (ISOL) facility. Taken from Ref [2]

.

At TRIUMF a primary beam of 500 MeV protons is delivered by the main cyclotron, which accelerates negatively charged hydrogen atoms before they are stripped to bare protons and sent towards the ISAC target hall. The protons pass through the target and the radioactive fragments diffuse out into an ion source where they are ionized to a 1^+ charge state and extracted by an applied electric field. A high resolution magnetic separator is then used to select the desired radioactive products based on their deflection in the magnetic field, which is determined by their atomic mass, and unwanted ions are deflected into carefully positioned slits.

3.1.2 The ISAC facility

After extraction from the ion source and separation, the ions are then transported to the radio frequency quadrupole (RFQ) which forms the first step in the ISAC accelerator chain. Located in the ISAC-I experimental hall, the RFQ accelerates ions to energies of 2 - 150 AkeV, provided that the ions fall within the acceptance of the RFQ which is limited to $A/q < 30$. The Charge State Breeder (CSB) can be used to raise the charge state of ions such that they fall with the A/q acceptance of the RFQ and of later accelerator stages[1]. Since use of the CSB was not necessary for any of the experimental work presented in this thesis, its principles of operation and characteristics will not be

[1]The acceptances of the DTL and SC-LINAC are further reduced to $A/q < 7$ and have a lower acceptance limit of $A/q > 2$ [37]

discussed; for more information see ref [38]. The RFQ comprises four vane-shaped rods with an applied oscillating electric potential. The potential has a maximum amplitude of 75 kV and a frequency of 35 MHz. The opposing polarities of pairs of opposite rods generates a quadrupole electric field that focuses the beam in one transverse direction, and after a half RF period will focus in the other transverse direction, thus achieving 2D confinement of the beam. By shifting one pair of rods by half an RF period, an electric field along the beam axis will be created, accelerating the ions forward.

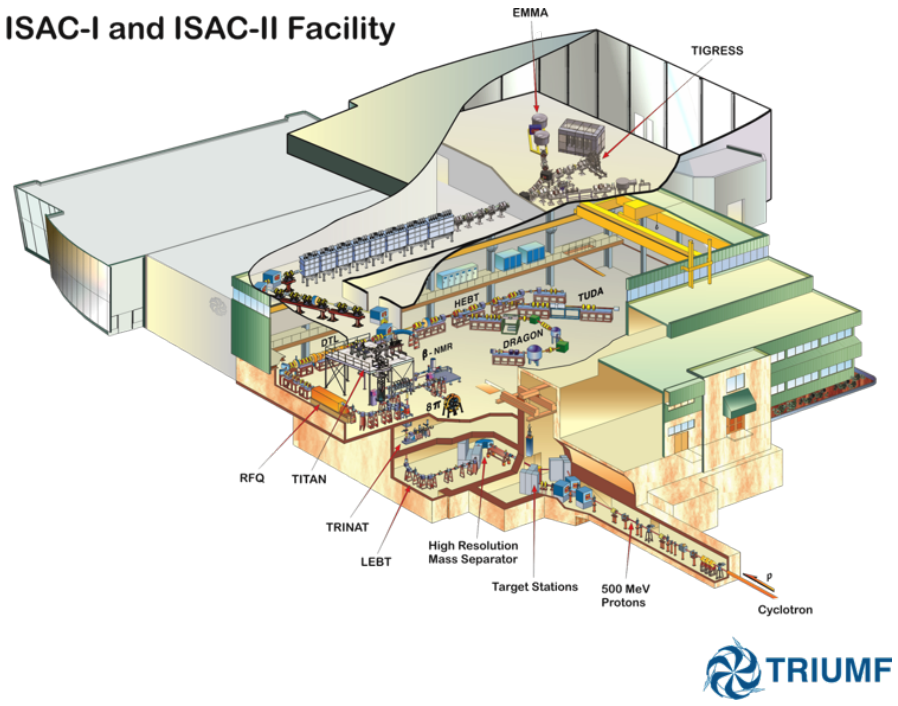

FIGURE 3.2: Schematic of the TRIUMF-ISAC radioactive ion beam facility, in which the EMMA experiment can be seen located in the top-right of the diagram. Figure taken from Ref. [39].

Before entering the RFQ, the beam is bunched into beam packets, and downstream of the RFQ an 12 MHz chopper removes the satellite peaks produced during the bunching process. This gives ISAC beams a characteristic time period between bunches of 85 ns. The beam is then transported along the Medium Energy Beam Transport (MEBT) beamline where a carbon stripper foil is used to increase the charge state of the beam. The beam is then re-bunched and sent through a drift tube linear accelerator (DTL), which uses an RF electric field to accelerate the beam up to 1.8 A MeV. A DTL works by accelerating the beam with a time-varying electric field, while shielding the beam with drift tubes when the field would cause deceleration. The final acceleration stage is the super-conducting linear accelerator (SC-LINAC) which is capable of delivering beams with energies over 6.5 A MeV to the ISAC-II experimental hall.

3.1.3 The OLIS facility

Beams of stable nuclei are also produced at TRIUMF with the Off-Line Ion Source (OLIS) facility. This facility consists of a microwave driven cusp source for singly and doubly charged ions, a surface ion source for alkali beams, and a multi-charge (super-nanogan) ion source [40]. Enriched samples are often used with OLIS to increase the isotopic purity of the beam.

3.2 The EMMA recoil spectrometer

The Electromagnetic Mass Analyzer (EMMA) is a vacuum-mode recoil mass spectrometer designed to separate the products of nuclear reactions from the unreacted beam, and subsequently disperse them in accordance with their mass/charge (A/q) ratio. EMMA is situated within the ISAC-II experimental hall at TRIUMF (see figure 3.2) and is specially designed to be coupled with the TIGRESS HPGe (high purity germanium) γ-ray detector array [41]. The design of EMMA is tailored for experiments involving fusion-evaporation and transfer reactions with radioactive beams, and as such is optimized for both efficiency and selectivity, Ref.[42] details the initial design considerations for EMMA.

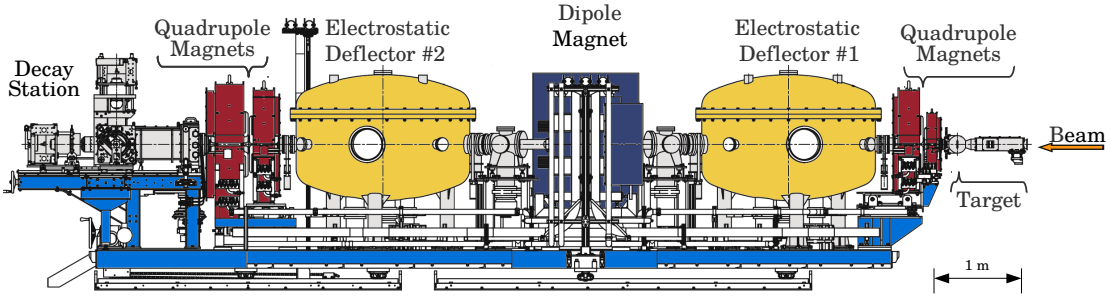

FIGURE 3.3: Schematic of the EMMA recoil mass spectrometer, showing the target chamber, quadrupole lenses and dipole magnets, electrostatic deflectors, and focal plane chambers. Note that the decay station is not yet constructed, and the only focal plane detectors available currently are those discussed in Section 3.2.3.

3.2.1 Target chamber

EMMA targets consist of thin foils of material mounted directly onto target frames, of which a maximum of three can be fixed to the rotatable target wheel. In place of a target frame, an alpha source can be mounted instead to test the spectrometer and calibrate charged particle detectors within the chamber. In addition to determining

the beam flux, the thin foil targets need to be regularly monitored for target content degradation during an experiment. This is achieved by monitoring scattered particles with two silicon surface barrier (SSB) detectors mounted at 20° from the beam axis. The rate of elastically scattered particles detected by the SSB detectors is proportional to the beam intensity and the number density of particles in the target. A Faraday cup inside the target chamber can be maneuvered into the path of the beam periodically to measure the absolute beam intensity. For beam currents too low to be accurately measured with a Faraday cup, a PIN diode fixed to an electrically isolated target frame can be used instead. In addition to monitoring the target content, this method of normalizing the number of SSB counts to the beam current measured by the Faraday cup can be used to determine the total number of incident beam particles independently of beam intensity fluctuations within a given period of data taking. The ability to measure the total number of incident beam particles is vital for determining reaction cross sections.

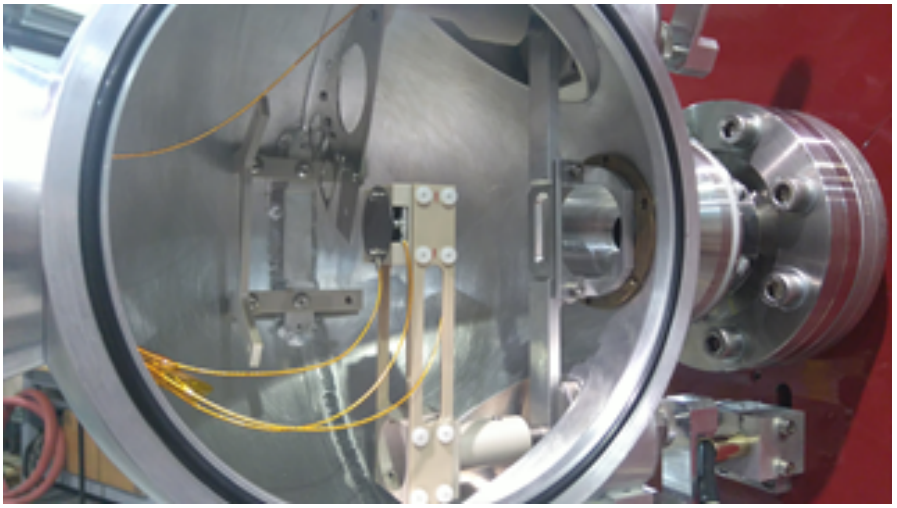

FIGURE 3.4: Image of the EMMA target chamber taken prior to the December 2016 test. The target mounting mechanism and Faraday cup are both visible inside the chamber. The 2° aperture is also shown mounted, but was not in place during that test beam time.

3.2.2 Ion optical elements

The ion optical layout of EMMA is based on that of a similar spectrometer, the Fragment Mass Analyzer (FMA), currently operated at Argonne National Laboratory [43]. This design, first employed by CAMEL at INFN Legnaro [44], incorporates a dipole magnet placed between two electrostatic deflectors, and is often refereed to as an EME type layout. The electrostatic deflectors select ions based on their energy per charge (E/q), while the dipole magnet selects on momentum per charge (p/q). The two elements together can therefore be used to form ion trajectories based on mass per charge (A/q).

The motion of ions in the presence of magnetic and electric fields is described by the Lorentz equation:

$$\mathbf{F} = q(\mathbf{E} + \mathbf{v} \times \mathbf{B}) \tag{3.1}$$

Where $\mathbf{F}$ is the centripetal force experienced by the ions, q is the charge state of the ion, $\mathbf{v}$ is the ion velocity, and the electric and magnetic fields are denoted by $\mathbf{E}$ and $\mathbf{B}$ respectively.

If only an electric field is acting on the ions, Equation 3.1 can be reduced to find the radius of curvature that the trajectory of the ions will follow:

$$\rho_E = \frac{mv_\perp^2}{q|\mathbf{E}|} \tag{3.2}$$

Where m is the particle mass and $v_\perp$ denotes the velocity component perpendicular to the field direction.

The products of fusion evaporation reactions will tend to have a large energy distribution, and so a relatively wide energy acceptance is called for. The energy acceptance simply refers to the maximum and minimum energies of ions - relative to that of the central trajectory - that can be transmitted without colliding with the walls of the spectrometer and being lost. To first order this is determined by the physical separation between electrodes of the electrostatic defectors, and by taking into account the dimensions and positions of apertures along the beamline which may restrict ion trajectories.

Similarly, the radius of curvature of charged particles exposed to a magnetic field can be determined from Equation 3.1 as:

$$\rho_B = \frac{mv_\perp}{q|\mathbf{B}|} \tag{3.3}$$

The maximum electric rigidity of ions which can be transmitted through EMMA is determined by multiplying together the bending radius of the electric dipoles and maximum electric field that can be maintained across the electrodes without breakdown. The maximum stable field that can be applied across each of the electrostatic deflectors has yet to be determined[1], though they are designed to achieve a maximum rigidity of 20 MV. The main design characteristics of the spectrometer are listed on Table 3.1. The magnetic rigidity of EMMA is limited to 0.9 Tm by the maximum achievable pole-tip

[1] As of the time of writing this thesis the maximum potential differences achieved for each of the EDs are 250 kV and 330 kV for ED1 and ED2 respectively

field for Q1. Q1 is a short quadrupole so it requires a very high pole tip field in the standard tune, thereby limiting the maximum magnetic rigidity. In practise however, the electrostatic rigidity limit is more restrictive than the magnetic rigidity limit imposed by Q1.

Dipoles	MD	EDs	
Radius of Curvature	1m	5m	
Deflection Angle	40°	20°	
Gap (mm)	120	125	
Maximum Field	1 T	40kV/cm	
Maximum Rigidity	1 Tm	20MV	
Quadrupoles	Q_1	$Q_{2,3}$	Q_4
Bore Diameter (cm)	7	15	20
Effective Field Length (cm)	14	30	40
Max pole tip field (T)	1.21	0.87	0.81
Max field gradient (T/m)	35	11	8.1
Solid angle acceptance		16 msr ($\pm 3.6^\circ$)	
m/q acceptance		± 4 %	
Energy acceptance		$+25\%/-17\%$	
First order m/q resolving power		550	
m/q dispersion		0 - 20 mm/%	

TABLE 3.1: As designed EMMA ion-optical dimensions, maximum fields, and expected performance, calculated using the ion optics code GIOS [45]. For all the work presented in this thesis the m/q dispersion is set to the standard value of 10 mm/%, but can be varied within the limits indicated. Note that the m/q resolving power is quoted assuming a 1 mm beam spot and neglects any aberrations due to finite angular or energy spread of the transmitted ions. This should therefore be considered a theoretical upper limit to the resolving power under idealized conditions.

In addition to the ion optical elements themselves, EMMA has a series of strategically placed slit systems that are designed to enhance the beam suppression capability of the spectrometer. There are three slit boxes along the optical axis of EMMA, two positioned immediately upstream and downstream of the dipole magnet, and a final set of slits at the focal plane. The MD slits are identical in design and are controlled by pairs of linear motion actuators. The focal plane slits comprise two pairs of slits; the first being a standard pair of actuated plate slits; and the other is a pair of finger slits which can also be rotated to more finely control the profile they present to the beam.

3.2.3 Focal plane detectors

The EMMA focal plane station accommodates a series of detector systems that form part of a modular set-up that can be tailored to the specific needs of the experiment. This

section will detail the principle of operation and design specifications of each detector used to obtain the measurements presented in this thesis.

i) PGAC

The primary recoil detection device, onto which the transmitted ions are focused, is a parallel grid avalanche counter (PGAC). Sometimes referred to as a multi-wire proportional counter (MWPC), a PGAC consists of a series of wire grids held at fixed voltages within a gas medium. The purpose of the PGAC is to measure the incident position of ions reaching the focal plane of EMMA. As the dispersion of ions at the focal plane is determined by their m/q, the x-y positions of incident ions measured by the PGAC allows for identification of transmitted species.

The EMMA PGAC is constructed from three wire grids held onto separate printed circuit boards (PCBs) spaced by 3.25 mm. The wires in the middle grid are held at positive voltage, while the other two are held at a negative voltage; thus creating an electric potential between the wire planes. As ions enter the PGAC they ionize the iso-butane gas contained within the PGAC, the charge carriers produced through ionization are accelerated towards the wire grids inducing an electrical signal on nearby wires. The potential difference across the wire grids is set high enough to induce a Townsend discharge, whereby the accelerated free electrons collide with the gas molecules, liberating secondary electrons to create an avalanche effect that greatly amplifies the signal.

Position sensitivity is achieved by connecting the cathode wires to an inductor-capacitor delay line, which delays the arrival of signals into the data acquisition (DAQ) system by a time delay dependent on the position of the wire that received the initial signal. The time delay is recorded with respect to the anode grid which acts as the trigger for the DAQ, see Section 3.2.4. The first cathode grid consists of 166 vertically held wires, while the second cathode, positioned after the anode, is comprised of 66 horizontally held wires. The anode wire grid, comprised of 66 horizontally held wires, is split into 3 electrically isolated sections of 22 wires each in order to reduce the overall capacitance of the detector. The spacing between the wires on all grids is 1 mm. The outer three wires of each grid are held at ground potential, and kapton shields between the grids further reduces the fiducial area of the detector to 160 $\times$ 54 mm. Table 3.2 lists the characteristics of the EMMA PGAC.

The time delay applied between adjacent cathode wires is 2.5 ns. Therefore, as the spacing between the wires is 1 mm, a 2.5 ns delay corresponds to 1 mm. Each cathode wire plane outputs a pair of signals, from which their time delays with respect to the anode is used to reconstruct the position of the incident charged particle. For example,

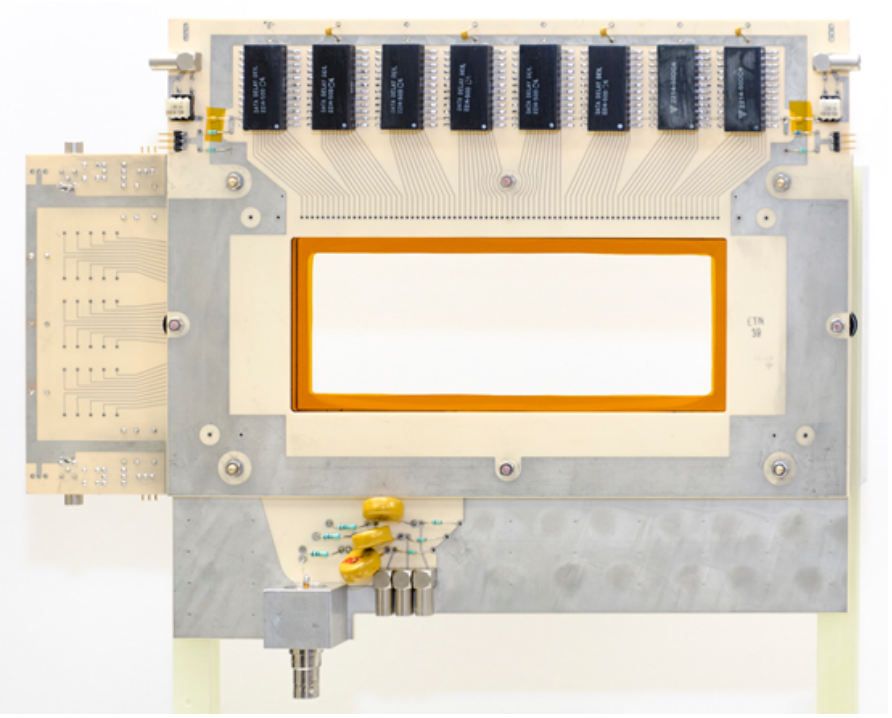

FIGURE 3.5: Picture of the EMMA PGAC. The delay-line chips associated with the x-sensitive cathode wires are clearly visible across the top of the PCB. The kapton shield lining the fiducial area of the detector is also visible.

Gas	Isobutane
Operating pressure	2 - 6 Torr
Window material	Mylar
Window thickness	0.9 μm
Window position (from anode)	-27.2 mm, +52.8 mm
Wire material	Gold-plated Tungsten
Cathode wire diameter	25 μm
Cathode wire pitch	1 mm
Number of cathode wires	166 (vertical), 66 (horizontal)
Anode wire diameter	15 μm
Anode wire pitch	1 mm
Number of anode wires	66 (horizontal)
Anode-cathode gap	3.18 mm
Fiducial area	154 mm $\times$ 54 mm
Transparency	94%
Typical cathode bias	-80V
Typical anode bias	+470V

TABLE 3.2: Design characteristics of the EMMA PGAC, including typical operating pressures and voltages. The positions of the windows are given with respect to the anode plane along the beam axis (positive means further downstream).

a particle incident on the detector with an x-position 20 mm from the left side of the detector will produce an X-left signal delayed by 20 mm $\times$ 2.5 ns/mm = 50 ns and an X-right signal of (166 - 20) mm $\times$ 2.5 ns/mm = 365 ns. Equation 3.4 details how

cathode timing signals are used to measure position with respect to the center of the PGAC.

$$X = \frac{L}{2} \times \left[\frac{X_{right} - X_{left}}{X_{right} + X_{left}} \right] \tag{3.4}$$

Where L is the length of the detector in a given direction (166 mm and 66 mm for the x and y directions respectively). X_{left} and X_{right} are the x-sensitive cathode timing signals, but can be substituted for y-sensitive signals i.e. Y_{top} and Y_{bottom}. The time difference is normalized to the sum since the sum should always give a constant value related to the dimensions of the detector.

ii) Ionization chamber

EMMA is capable of separating the products of nuclear reactions by their atomic mass, however mass spectrometers such as EMMA do not have sufficient resolving power to allow for the distinction between isobars (ions with the same atomic mass number, but differing atomic number). Different isobars are instead separated by using the EMMA focal plane ionization chamber, another gas filled detector, which uses energy loss as a function of distance to distinguish ions with differing atomic number (Z). The energy loss per unit length (or *linear stopping power*) can be approximated by the *Bethe equation*, which for non-relativistic particles reduces to Equation 3.5:

$$-\frac{dE}{dx} = \frac{4\pi e^4 z^2}{m_e v^2} NZln\left(\frac{2m_e z^2}{I}\right) \tag{3.5}$$

where v and ze are the speed and charge of the incident particle, N and Z are the number density and atomic number of the absorber medium, m_e is the electron mass and I is an experimentally determined quantity related to the average excitation and ionization potential of each element in the absorber.

As an incident particle travels through the chamber it ionizes the gas molecules along its trajectory. The free electrons produced by ionization in the gas drift toward the *Frisch grid*, which acts to shield the anode so that the signal amplitude dependence on the position of interaction is removed. Once the electrons pass through the *Frisch grid* a signal is induced on the anode pads. The amplitude of the signal generated is proportional to the number of charge carriers produced, which is in turn dependent upon the amount of energy loss in the gas volume to which the anode pad is sensitive. The maximum pulse height expected from the creation of n_0 ion pairs is given by equation 3.6.

$$V_{max} = \frac{n_0 e}{C} \tag{3.6}$$

Where C is the capacitance of the detector, typically of the order of 100 pF. The number of ion-pairs produced can be estimated by the incident particle energy divided by a material dependent parameter accounting for the energy required to produce an ion pair.

By having multiple anode pads spread along the incident particle trajectory, a representation of energy loss as a function of penetration depth can be constructed. So long as the energy resolution is sufficient, isobars can be identified through the differing energy loss measured by each anode segment. The FWHM energy resolution expressed as percentage of the deposited energy can be estimated as:

$$R = 2.35\sqrt{\frac{FW}{E_d}} \tag{3.7}$$

Where F is the Fano factor, W is the energy required per electron-ion pair, and E_d is the total energy deposited.

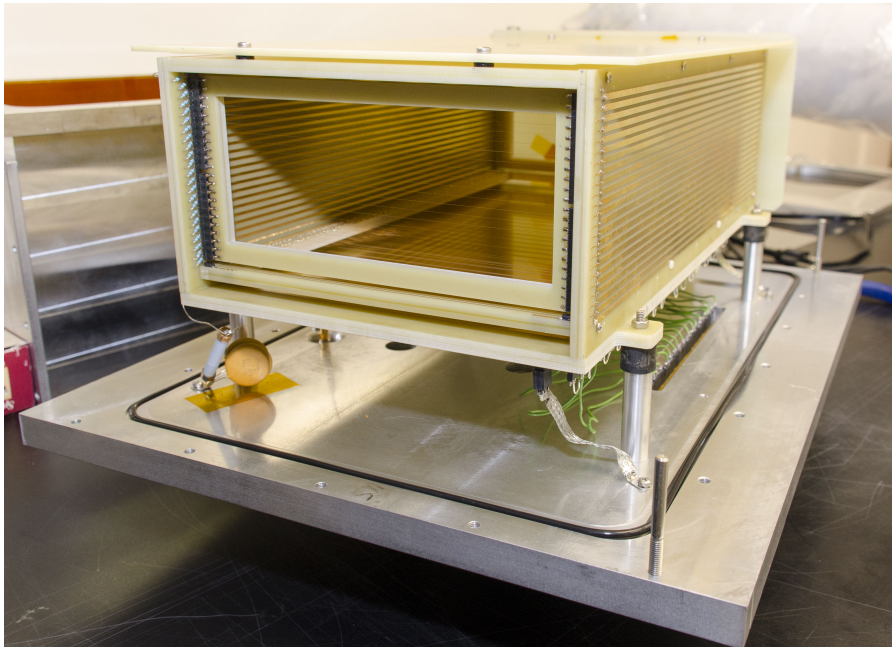

FIGURE 3.6: Picture of the EMMA ionization chamber. The entrance to the ion chamber is shown in the foreground of the image. The active area is identical to the PGAC so as to utilize the full cross section of the focal plane.

The EMMA ionization chamber has 16 anode pads (each 2 cm wide) from which signals can be taken independently, or be electrically ganged together to effectively form larger segments. The chamber itself was designed and manufactured by the TRIUMF detector

facility, as were the preamplifier cards into which the signals are directly fed. Table 3.3 lists some key design characteristics for the EMMA IC.

Gas	Isobutane
Operating pressure	10 - 100 Torr
Chamber voltage	15.8 V/Torr
Window material	Mylar
Window thickness	2 μm
Window support wire diameter	200 μm
Window support wire spacing	5 mm
IC wire diameter	50 μm
IC wire pitch	4 mm
Number of IC wires	18
Transparency	91%
Active area	(160×60) mm^2
Active length	320 mm
Entrance deadlayer length	38.5 mm
Exit deadlayer length	35 mm
Window-to-window distance	393.5 mm

TABLE 3.3: Design characteristics of the EMMA Ion Chamber. Note that the optimal operating voltage increases as a function of pressure.

iii) Focal plane Silicon detector

The final focal plane detector used for the measurements presented in this thesis was an ORTEC ULTRA ion-implanted charged particle detector (Model designation: BU-060-3000-500) [46]. The detector has a factory guaranteed energy resolution of 60 keV FWHM for 5.486 MeV α particles, an active area of 3000 mm^2, and a depletion depth of 500 μm. The heavy ion recoils are stopped completely within the active volume of the detector, measuring their total residual energy. This detector was coupled to a Model 142B ORTEC preamplifier [47] for the December 2016 in-beam test[1], though was later used in conjunction with a 142C preamplifier as per the manufacturer recommendations [48].

3.2.4 Data Acquisition System (DAQ)

The EMMA data acquisition logic is shown diagrammatically by Figure 3.7. The PGAC outputs a total of 7 signals: x3 anode signals and x4 cathode signals. All PGAC signals are fed into a custom pre-amp constructed by the TRIUMF detector group, and are then further amplified by a LeCroy 612A PM Amplifier. The cathode signals are then discriminated by a Tennelec 455 Quad CFD before being sent to a Caen V1290N Multihit

[1]The optimum preamplifier could not be utilized during the December test due to a faulty resistor which was later replaced

TDC. The timing of these signals with respect to the trigger are used to determine position as described in Section 3.2.3.

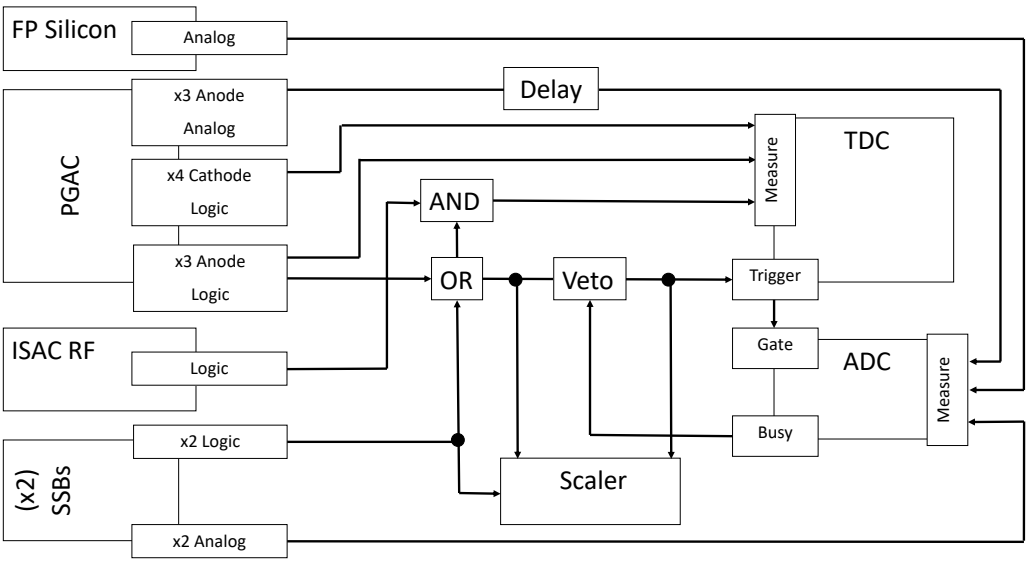

FIGURE 3.7: Logic diagram for the EMMA DAQ system, see text for details.

Two amplified outputs of the anode signals are utilized: the first output is delayed before being fed into the Mesytec 32 channel peak sensing ADC, the other is discriminated by a Caen V843 16 channel CFD. The delay of the anode analogue signals is long enough such that they arrive at the ADC subsequent to the TDC trigger. Two copies of the anode logic signals are taken from the CFD, one set are sent directly to the TDC, whereas a logical `OR` of the secondary outputs are used to form the trigger. Discriminated signals from the SSB detectors (located within the target chamber) are also included in the logical `OR` with the anode signals to generate the trigger. The focal plane ion-implanted silicon detector is not part of any trigger logic, with only analogue signals being sent directly to the ADC after amplification.

The Mesytec ADC gate is opened by a signal sent from the output trigger of the TDC. In order to prevent the acceptance of additional triggers while the ADC is processing signals, the busy signal output from the ADC is fed into the veto input of a Philips Scientific 752 Quad two-fold logic unit through which the trigger signal must pass. A scaler unit receives copies of the trigger both before and after passing the veto; thereby recording the number of presented and accepted triggers respectively, the ratio of which gives an estimate of the DAQ live-time. Discriminated signals from the SSB detectors are also fed into the scaler unit for beam monitoring purposes.

A useful diagnostic for correlating beam induced events is to record the RF signal sent from the RFQ pre-buncher. The RF signal is discriminated by an LRS 621 Quad leading-edge discriminator and fed into an LRS 622 coincidence unit, once a trigger is received the discriminated RF signals are read into the TDC. To be recorded by the TDC, the RF signals must occur in coincidence with a gate created from a copy of the trigger sent to a Philips Scientific Model 794 gate/delay generator. The gate is set wide enough to allow at least 3 RF signals to be recorded per trigger.

3.3 The DRAGON recoil separator

DRAGON (Detector of Recoils And Gamma-rays Of Nuclear reactions) is a vacuum-mode electromagnetic separator located at TRIUMF. The design of DRAGON is specifically optimized to measure cross-sections of proton and alpha induced radiative capture reactions at energies relevant for astrophysical processes [49]. Due to the sub-Coulomb barrier energies involved in these reactions at the relevant stellar temperatures, this type of measurement has the primary challenge of extracting reliable limits on cross-sections for extremely low yield experiments. Beam suppression is therefore critical to the design of the separator as well as detection efficiency. The main components of the DRAGON facility include: a window-less gas target, a γ-ray detector array, an electromagnetic recoil separator, and heavy ion detectors at the focal plane.

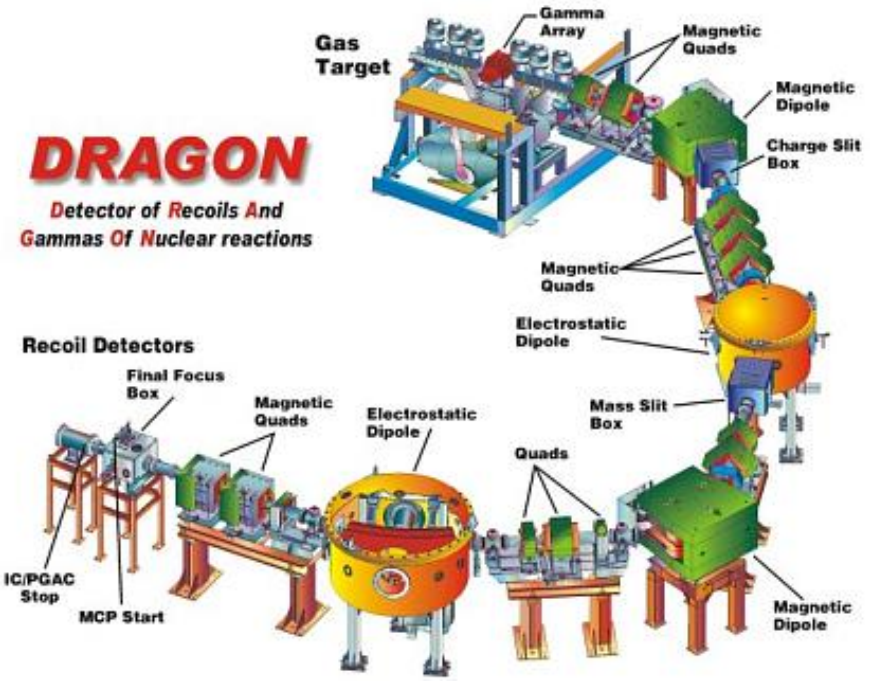

FIGURE 3.8: Diagram of the DRAGON facility at TRIUMF. Image taken from `http://dragon.triumf.ca/system.html`

3.3.1 Windowless gas target and associated pumping systems

A key feature of the DRAGON facility is its sophisticated windowless gas target and associated pumping systems. Many experimental challenges associated with proton and alpha capture reactions can be avoided by the use of a window-less gas target. Other options such as gas cells and compound/implanted foil targets for instance suffer from complications arising from target degradation and background reaction channels. Indeed

many similar experimental setups are emerging in the field which incorporate windowless gas target technology[1](See for instance the St George facility [50] and SECAR [51]).

To contain resonances within the target and increase the yield of a reaction, it is desirable to maximize the number of target atoms exposed to the beam. Pumping constraints however restrict the maximum gas pressure to 8 Torr, and the length must be also be restricted to maximize transmission of recoils through the separator. The 11 cm distance between the inner-most apertures within the target define the gas target volume, however the effective target length is usually 12 - 13 cm depending on the pressure [49]. The target pumping volume is encased in a thin aluminium box to reduce the attenuation of γ-rays emitted from nuclear reactions occurring in the gas. The trapezoidal shape of the target improves the pressure differential by deflecting gas jets leaving the chamber away from the pumping tubes situated at the bottom of the chamber. The temperature and pressure inside the chamber are constantly recorded by internal sensors.

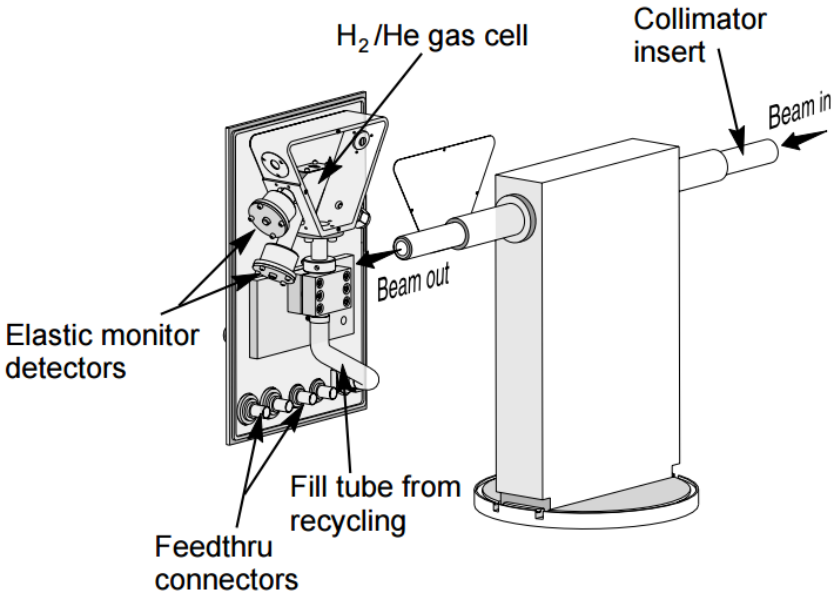

FIGURE 3.9: Diagram of the DRAGON gas target box[49].

Gas leaking out of the inner chamber is recirculated by a series of Roots blowers consisting of: two Leybold WSU2001 (in parallel), two WSU501 (in parallel), and one WS500. The Roots blowers raise the outflow gas pressure above 40 Torr, before being fed through a liquid nitrogen cooled Zeolite trap which removes some impurities and slows the recirculation time for increased pressure stability. The gas target is flanked upstream and downstream by several pumping tubes connected to seven V1000HT turbo-molecular pumps which create a strong pressure differential between the target volume and the $P < 10^{-6}$ vacuum needed in the surrounding beamline. The pumping tubes are tapered

[1]The two separators referenced here are based on the design of DRAGON, but instead use gas jet targets which provide improved target density

and angled towards the target so as not to restrict the geometric acceptance of the spectrometer, see Figure 3.11

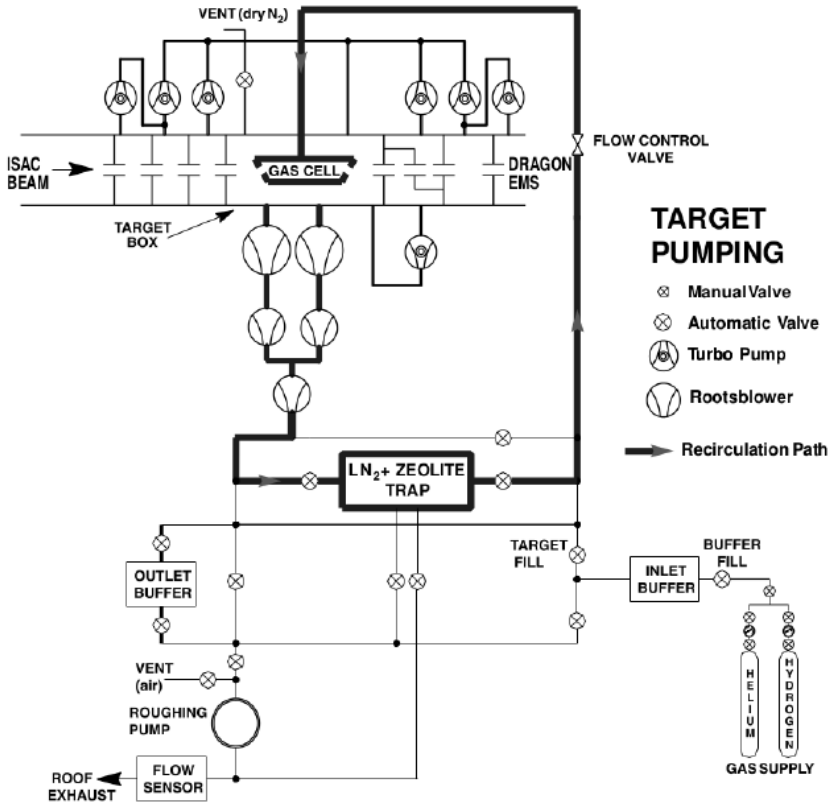

FIGURE 3.10: Schematic of the DRAGON gas target pumping system [49].

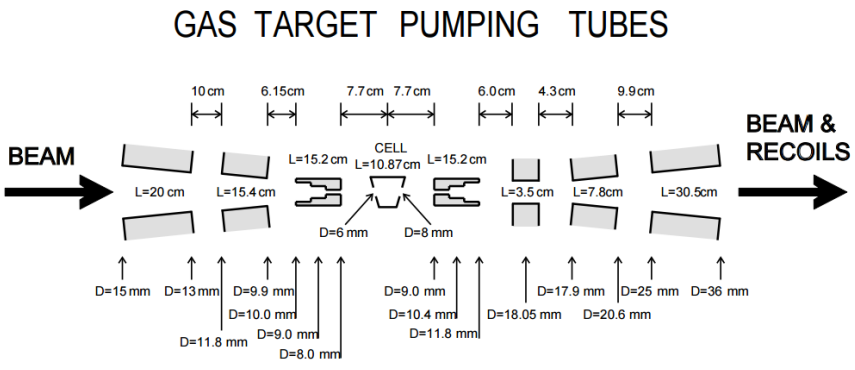

FIGURE 3.11: Diagram of the pumping tubes flanking the entering and exiting beamline of the DRAGON gas target [49].

3.3.2 Beam intensity monitoring system

In order to measure nuclear reaction cross sections it is essential to have a reliable method for determining the total number incident beam ions on target. At DRAGON this is done using two ORTEC Ultra Cam silicon detectors mounted at 30° and 57° from

the beam axis, these are shown on Figure 3.9. The detectors are both collimated by an aperture to view the center of the gas target. Given a reasonable pressure stability, the rate of detected scattered target particles is directly proportional to the incoming beam intensity. This elastic scattering rate measured during the first and last few minutes of data taking runs can then be normalized to Faraday cup readings taken before and after each run to give an absolute determination of the total number of beam ions incident during a run (this method is detailed in Ref [52]).

3.3.3 BGO γ-ray detector array

Surrounding the target is an array of 30 Hamamatsu R1828-01 BGO scintillators for the detection of prompt γ-rays emitted from radiative capture reactions. The hexagonal shape of the detectors allows them to be tessellated in a compact geometry around the target for a maximum coverage in the range of 89-92%. The minimum polar angle (θ) covered by the array is 8°, corresponding to detectors positioned close to the beam axis, while a gap in the azimuthal angle (ϕ) coverage occurs at the bottom of the array, with the missing angular range between $256 - 284^{\circ}$. BGO was chosen as the scintillating material for its high intrinsic efficiency and lack of light emission with long time components (or afterglow). The energy resolution determined with a 6.13 MeV source is roughly 7% FWHM averaged over all 30 detector units. Each crystal is 76 mm long by 56 mm wide and coupled to a 51 mm cylindrical photo-multiplier tube (PMT) [1]. The typical bias applied to each detector is 1700 V The crystals are each coated with a reflective 1 mm thick layer of MgO that aids detection efficiency, and then a 0.5 mm thick aluminium outer casing.

3.3.4 Ion optical elements

The design of DRAGON's ion optics is optimized to handle the specific challenges presented by measuring radiative capture reactions in inverse kinematics at energies of astrophysical interest. These challenges particularly stem from the kinematic similarity between the scantly produced recoils of interest and the copious background of unreacted beam. For radiative capture reactions the momenta of the recoils of interest and unreacted beam are very similar, and both exit the target at close to zero degrees. In fact, due to the momentum kick received by the recoil from the emission of a prompt γ-ray, the recoils have a cone-shaped angular distribution exiting the target. Every spectrometer like DRAGON has a finite angular acceptance, beyond which incoming ions are no longer transmitted through to the focal plane instruments. The acceptance of DRAGON

[1] The PMTs were manufactured by Electron Tubes Ltd

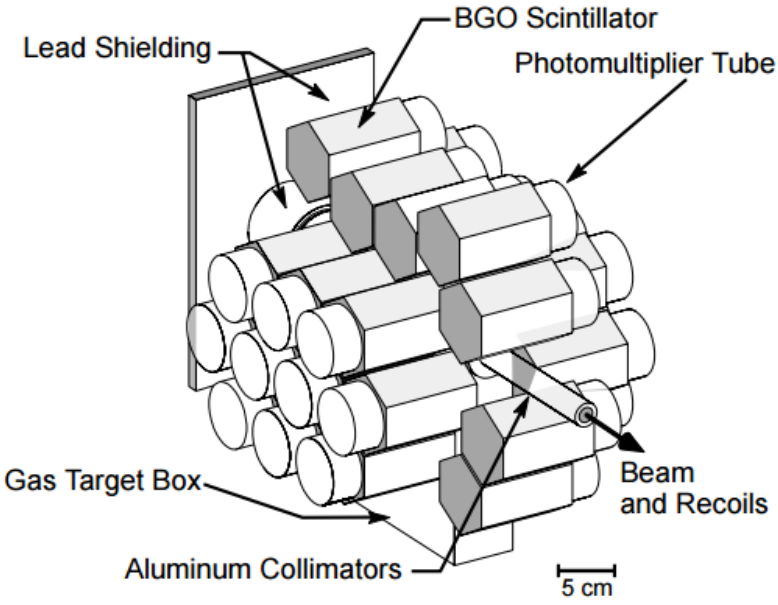

FIGURE 3.12: Diagram of the BGO γ-ray detector array surrounding the DRAGON gas target. The minimum The total solid angle coverage of the array is 92%. Figure taken from Ref [49].

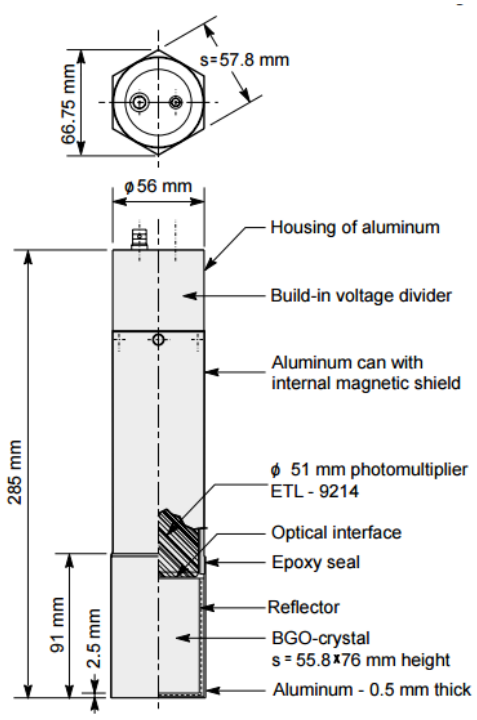

FIGURE 3.13: Diagram of one of the BGO γ-ray detector units [49].

is ± 20 mrad, which is enough to handle the often very small recoil cone angles for (p, γ) and (α, γ) reactions with radioactive beams at astrophysical energies. However, some losses do still occur, due to both the finite angular and energy acceptances, and must be quantified by careful simulation to find what fraction of recoils are transmitted to

the focal plane heavy ion detectors; this fraction is termed the 'separator transmission efficiency' and typically lies in the >95% range for most DRAGON experiments.

Dipoles	MD1	ED1	MD2	ED2
Radius of Curvature	1 m	2 m	0.813 m	2.5 m
Deflection Angle	50°	20°	75°	35°
Gap (mm)	120	100	125	100
Maximum Field	0.59 T	40 kV/cm	0.82 T	32 kV/cm
Maximum Rigidity	0.59 Tm	0.4 MV	0.66 Tm	0.32 MV
Solid angle acceptance		±20 mrad		
Energy acceptance		±4%		

TABLE 3.4: DRAGON magnetic and electric dipole properties, and spectrometer acceptances

In much the same way as EMMA, DRAGON uses a series of electromagnetic fields to select the recoil of interest from the unreacted beam according to their mass/charge ratio. The motion of charged particles in electromagnetic fields was outlined previously in introducing EMMA's ion optics and so will not be repeated here. Instead this section will focus on discussing the key differences between the two separators. The acceptance of DRAGON has already been mentioned as ±20 mrad (±1.14°), which is far smaller than the ±3.6° acceptance of EMMA. The large acceptance of EMMA is required given that this spectrometer is designed to be able to accept the products of particle transfer and fusion evaporation reactions, whereas DRAGON does not need to accommodate such large cone angles to study radiative capture reactions. Similarly the energy acceptance of DRAGON is only ±4%, compared with EMMA's +25%/−17% energy acceptance which needs to accommodate the far larger kinematic phase space for products of fusion evaporation reactions.

DRAGON's ion optical elements consist of two magnetic dipoles and two electrostatic dipoles in an MEME configuration, with quadrupole and sextupole lenses for focusing and higher order corrections. Downstream of the first magnetic dipole (MD1) is a set of slits which can be maneuvered to only allow a given charge state to pass through, given that the momentum spread of the recoil and beam is fairly narrow and remembering that magnetic dipoles select according to momentum-per-charge $\left(\frac{p}{q}\right)$. This slit box also contains a Faraday cup which can be used to measure the charge state distribution of ions emerging from the target. Following MD1 is the first electric dipole (ED1), which together with MD1 provides mass separation. Immediately downstream of ED1 is another slit box designated as the 'mass slits'. Careful positioning of these slits is required to block unwanted ions, but even with careful positioning the suppression is not sufficient for measurements where the unreacted beam exceeds the recoil products by a factor of 10^{10} - 10^{15}. Inevitably a small portion of the tail of the unreacted beam

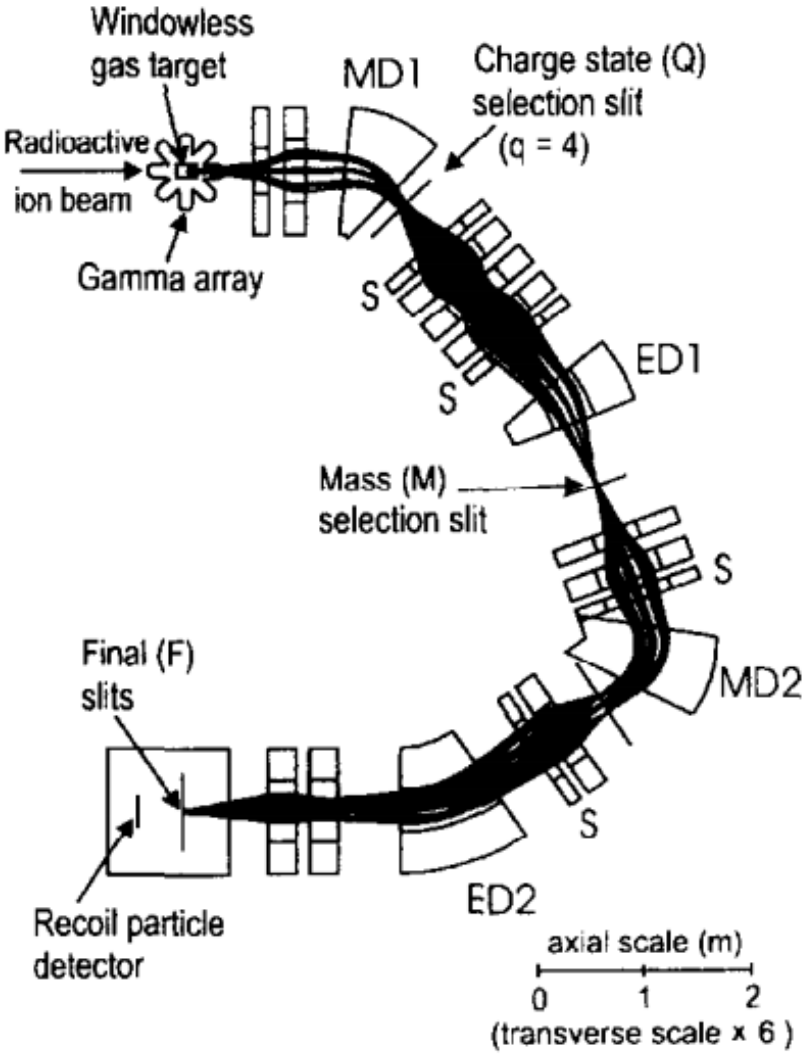

FIGURE 3.14: Ray diagram showing to ion optical layout of DRAGON [49]. Note the multiple focal planes along the spectrometer at the slit box locations; a feature absent in the design of EMMA.

rigidity distribution crosses into the accepted recoil distribution. To counter this a repeated MD-ED pair is used to extend the suppression into the 10^{-10} - 10^{-15} range [53] needed to push the boundaries of nuclear astrophysics experiments.

3.3.5 Heavy ion recoil detectors

Once reaching the focal plane, the transmitted ions are detected and identified by a series of heavy ion detectors. These detectors include a set of micro channel plates (MCPs), an ionization chamber, and a double-sided silicon strip detector (DSSSD). The DRAGON ionization chamber was not used for the work presented in this thesis and so shall not be discussed, however it resembles the EMMA ion chamber discussed in Section 3.2.3.

i) Micro channel plate detectors (MCPs)

The first of the heavy ion detectors used at DRAGON is a set of two micro-channel plate (MCP) detectors. MCPs are slabs of highly resistive material with an applied bias across them and many thousands of very small diameter (15 - 50 μm) tubes spread across their surface. In much the same way as photomultiplier tubes (PMTs), MCPs function as secondary electron emitters but achieve multiplication in a less controlled fashion. A single electron entering one of these channels can produce up to 10^6 secondary electrons at the anode. Unlike PMTs the gain is uncontrolled, but their timing properties are superior in that both the electron transit time and spread in transit times are far shorter than the fastest available PMTs. These properties give MCPs very good timing resolution which makes them extremely useful for time-of-flight measurements.

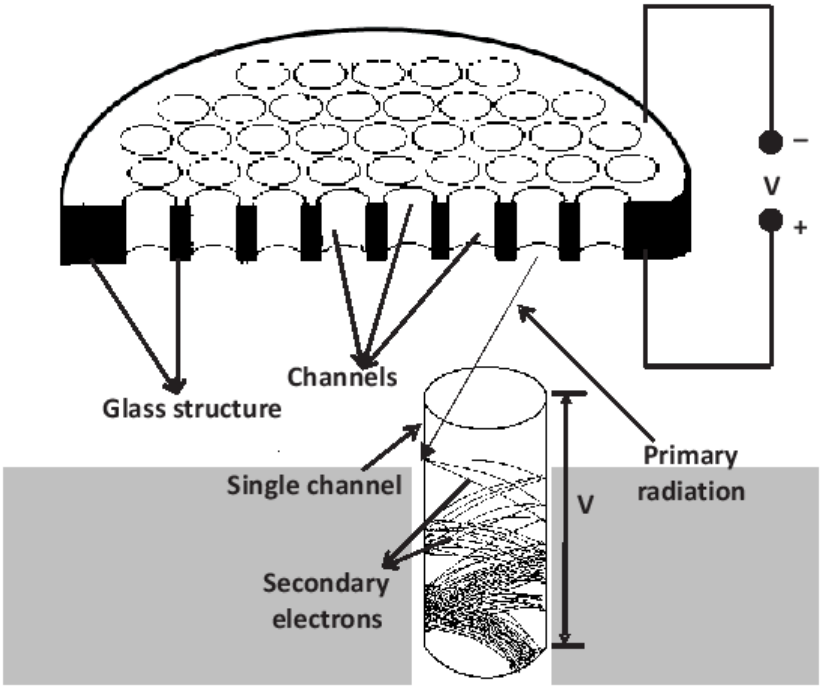

FIGURE 3.15: Schematic of a micro channel plate detector including a diagram of how secondary electrons are generated within the micro-channels. Taken from Ref [54].

At DRAGON a pair of MCPs are used to measure the transit time of ions across a section of beam line. The timing resolution in the MCPs is sufficient to discern between the differing speeds of unreacted beam ions and recoils. The primary electrons are produced by ions passing through very thin carbon foils, and are deflected upwards towards the MCP by a biased grid of wires held at 45° to the beam axis. It is important to note that the wire grids induce losses as a result of ions hitting the wires. The carbon foils used at DRAGON are only 50 nm thick in order to minimize energy loss and straggling.

ii) Double-sided silicon strip detector (DSSSD)

The final heavy ion detector used at DRAGON to fully stop the transmitted recoils is a micron W1 double-sided silicon strip detector (DSSSD) [55]. The active area of the detector is 50×50 mm^2, more than sufficient to cover the image size of the recoils at the focal plane. A detailed description of semiconductor physics is beyond the scope of this thesis, however an outline of the use of semiconductors as charge particle detectors is presented in Ref [56].

3.3.6 Data Acquisition System

The architecture of the DRAGON data acquisition system (DAQ) is constructed around the key function of being able to correlate prompt γ-rays emitted at the target with the arrival of heavy ion recoils at the focal plane. The method by which DRAGON is able to do this is by matching digital timestamps assigned to events received by the "head" (γ-ray) and "tail" (heavy-ion) detectors. The trigger logic and time-stamping is implemented using FPGA (Field Programmable Gate Array) firmware housed within an IO32, a general purpose VME board designed and manufactured at TRIUMF [57]. The IO32 contains an Altera Cyclone-I FPGA [58] and facilitates sixteen NIM and sixteen ECL input channels, and sixteen NIM output channels. The timing is set with reference to a 20 MHz quartz oscillator crystal with an accuracy rating of 20 parts per million. A more detailed description of the internal FPGA trigger logic can be found in Ref [59].

The system triggers for both head and tail detectors at DRAGON are controlled by their own IO32 modules in a master-slave configuration, with the head arbitrarily assigned to be the master. The time stamp counter (TSC) values associated with each event are stored in a first in, first out (FIFO) data structure which is subsequently used for timestamp coincidence matching in the analysis stage. The TSC values for the head events are zeroed by a user initiated command to write to a VME register, and in doing so causes a signal to be sent to the tail IO32 which resets its TSC. The slave IO32 clock is kept in-sync with the master by a pulser signal sent periodically from the master in accordance with its 40 MHz FPGA clock. The result of this configuration is a frequency synchronization and zero-point matching differing only by the transit time of the zero reset pulse between the two IO32s, which is assumed to be negligible.

A complete diagram of the DRAGON trigger logic is displayed in Figure 3.16. The head part of the DAQ handles signals emanating from the 30 BGO array detectors. Each detector signal is split into logic and analog branches, with the latter being delayed by a time sufficient enough to allow the leading edge of the trigger gate to arrive into the Caen V792 QDC [60] (charge to digital converter) before the analog signals are recorded.

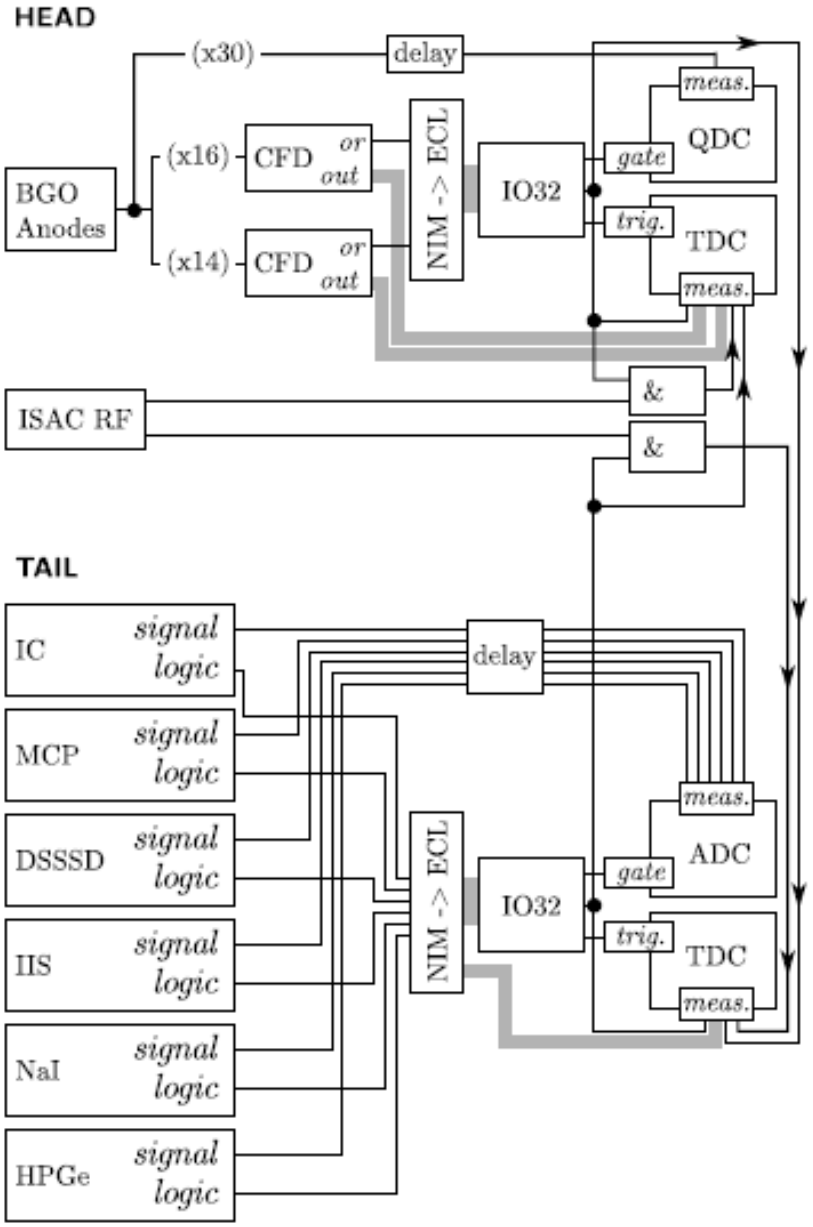

FIGURE 3.16: Block diagram of the DRAGON DAQ trigger logic [59]. The IC, NaI, and HPGe detectors were not used for the experimental work presented in the thesis. The latter two are only used for beam normalization purposes when using certain radioactive ion beams to measure beam composition. The IIS (Ion-implanted Silicon) detectors are the beam intensity monitors described in Section 3.3.2

After passing through the Caen V812 CFD [61] (constant fraction discriminator), the logical OR of the output signals are converted from NIM to ECL and are subsequently used to generate the head system trigger, and the individual outputs are fed into a Caen V1190 TDC [62] (time to digital converter). At the tail the outputs of each detector, including the beam monitoring detectors, are similarly split into signal and logic branches. The logic signals are transformed from NIM to ECL and used to generate triggers and measure timing with respect to the trigger. The analogue signals are delayed

by an appropriate amount before being sent to a Caen V785 ADC [63] (amplitude to digital converter) for measurement.

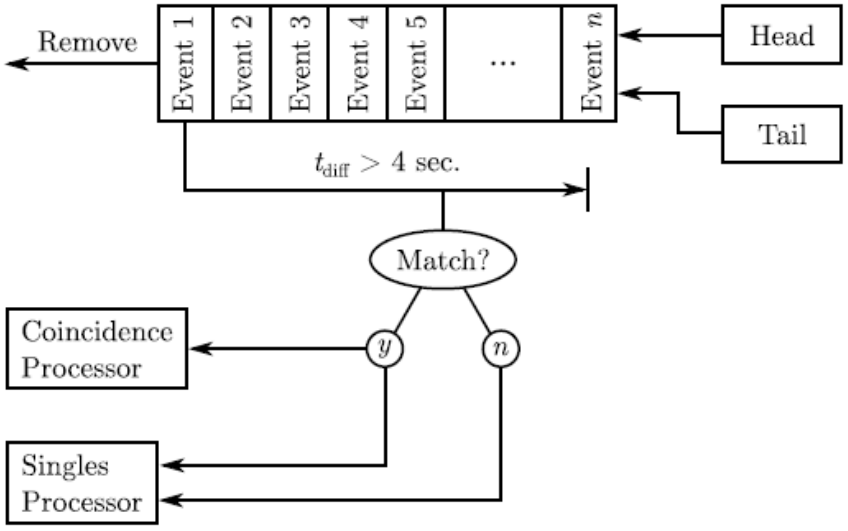

FIGURE 3.17: Flow diagram of the coincidence matching algorithm used at DRAGON [59].

The algorithm which matches coincident recoils and γ-rays is implemented in the *backend* computer, acting on the data once it has been transferred from the VME processor buffer [1]. As events are transferred to the analysis computer they are filled into a buffer ordered by their trigger time as measured by the TSC FIFO. As new events are placed in the buffer, the time between the earliest event and the latest event is calculated. If the time difference is greater than 4 seconds the entire event queue is searched for events with time stamps different by less that 10 μs. Events which pass this condition are designated as coincidences and are transferred to the coincidence processor[2]. Regardless of whether an event is designated as a coincidence or not, it will still be sent to the singles processor. After passing through the coincidence matching algorithm, the data is then sorted into histograms and written to disk. A flow diagram of the matching algorithm if shown by Figure 3.17.

In order to correctly measure the yield of a reaction the live time of the DAQ must be accounted for. The live time is defined as the fraction of run time over which the DAQ was able to accept and process new triggers. Naively, this could simply be calculated from the ratio of accepted to presented triggers. However, for the DRAGON

[1] Transfers from the VME buffer and the analysis computer are made once every second for efficiency reasons

[2] Only the earliest event will be recognized as a coincidence event, the latter event will remain in the buffer until it is eventually considered the earliest event and then subsequently sent to the singles processor and then removed

DAQ, with two independently operating system triggers each with its own singles live time, the matter of calculating the coincidence live time becomes more complex; given that coincidence events are only designated as such in the later analysis stage outlined previously. Instead the busy time (the finite time following an accepted trigger in which the DAQ is blind to incoming triggers) is used to estimate the number of events lost. For non-paralyzable dead time response[1], the number of events lost generated from a Poisson process is given by:

$$n_{lost} = \lambda \sum_{i=0}^{n} \tau_i = \lambda\tau \tag{3.8}$$

Where n is the total number of *recorded* events, λ is the rate of *generated* events, τ_i is the busy time associated with a given event i, and τ is the total busy time across the data taking run. The total number of events generated is therefore:

$$N = n + n_{lost} \tag{3.9}$$

Substituting Equation 3.8 into 3.9 and replacing λ with N/T, with T being the total run time, gives:

$$N = \frac{n}{1 - \tau/T} \tag{3.10}$$

From the definition of live time it is clear that the denominator of Equation 3.10 is the live time fraction L:

$$L = 1 - \tau/T \tag{3.11}$$

For coincidence events the total busy time τ is the time over which the head or[2] the tail is busy. In reality the generation of events does not strictly adhere to Poisson statistics, as fluctuations in beam intensity and target density make the estimator for n_{lost} inhomogeneous with time. Although, even in the presence of large beam fluctuations the difference in live time calculated assuming Poisson and non-Poisson statistics is of the order of $\pm 2\%$ maximum.

[1] DRAGON's detectors are assumed to be non-paralyzable as events occurring in the busy time do not have any appreciable affects on the detector response

[2] Note that the `OR` in this context has inclusive logic i.e. if both head and tail are busy then a coincident event will obviously not be recorded

3.3.7 γ Radiation detection and measurement

The detection of γ-rays within the DRAGON BGO array is governed by three distinct processes of energy loss. A complete description of the physics surrounding γ-ray spectroscopy is beyond the scope of this thesis, though a brief outline of the three main processes will be presented in this section, a more detailed treatment can be found in Ref [56].

Photoelectric Absorption

This interaction results in the complete disappearance of the initial photon, as all of its energy is transferred to the atoms in the absorber material. The absorbed energy liberates an electron from one of the atoms bound shells, creating a *photoelectron* with a kinetic energy described by Equation 3.12.

$$E_{e^-} = E_\gamma - E_b \tag{3.12}$$

Where E_γ is the energy of the initial γ-ray and E_b is the binding energy of the photoelectron in its original shell. The vacancy left by the photoelectron is quickly filled by either the capture of a free electron in the medium and/or by de-excitation of electrons in higher-lying shells. This re-arrangement of the bound electrons results in the emission of characteristic x-rays[1], most of which are promptly re-absorbed via photoelectric absorption. This probability of this process of occurring has a very strong dependence on the atomic number (Z) of the absorber medium; favouring high Z materials and tending to dominate for low energy γ-rays. The dominance of each of the processes outlined in this section, as a function of absorber atomic number Z and γ-ray energy, is represented by the graph on Figure 3.18.

Compton Scattering

The Compton scattering interaction occurs between the incident γ-ray and electrons in the absorber medium, whereby the incident photon is deflected through an angle θ with respect to its initial direction, therefore imparting some energy on the recoiling electron in accordance with momentum conservation. The energy of the scattered photon is given by Equation 3.13[2]:

[1] Instead of x-rays, the atomic energy can be sometimes be carried away via the emission of an Auger electron

[2] Equation 3.13 considers only scattering off a free electron at rest, hence neglecting any binding energy of the electron

$$E'_\gamma = \frac{E_\gamma}{1 + \frac{E_\gamma}{m_e}(1 - cos\theta)} \tag{3.13}$$

In principle all scattering angles (θ) are possible, giving rise to a *Compton continuum* of possible energies for the scattered photon; ranging from a head-on collision of maximum energy loss, to glancing collisions with barely any energy imparted to the absorber electrons. For an infinitely large detector of course, eventually all the initial energy of the photon will be imparted to the absorber medium, with the probability of photoelectric absorption increasing as the energy of the photon is attenuated. However, for realistic sized detectors the Compton continuum is preserved in the resulting measured spectra.

Pair Production

If the γ-ray energy exceeds twice the rest energy of an electron, another process of energy loss becomes possible. Within the Coulomb field of the nucleus an incident photon may decay into an electron-positron pair. The positron subsequently annihilates with another electron to form two 511 keV γ-rays, which are then either absorbed via the other two aforementioned processes or escape the detector entirely. If both 511 keV γ-rays escape the detector the result will be a so-called *double escape peak* located 1.022 MeV below the full energy peak (or *photopeak*). If only one escapes the detector volume however, then a *single escape peak* will form at 511 keV below the photopeak. Each of the characteristic features observed in γ-ray spectra, resulting from each of the processes mentioned in this section, is shown by Figure 3.19.

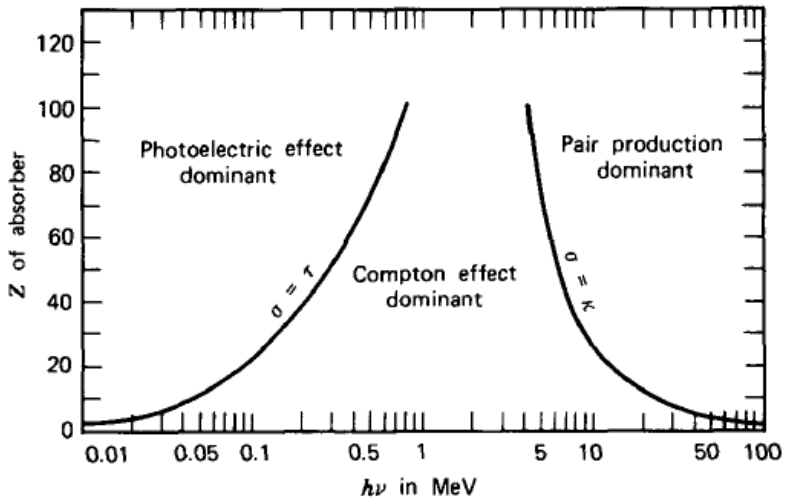

FIGURE 3.18: Chart taken from Ref [56] showing the relative importance of the three major types of gamma-ray interactions. The solid lines represent intersections where two competing effects have equal probability of occurring.

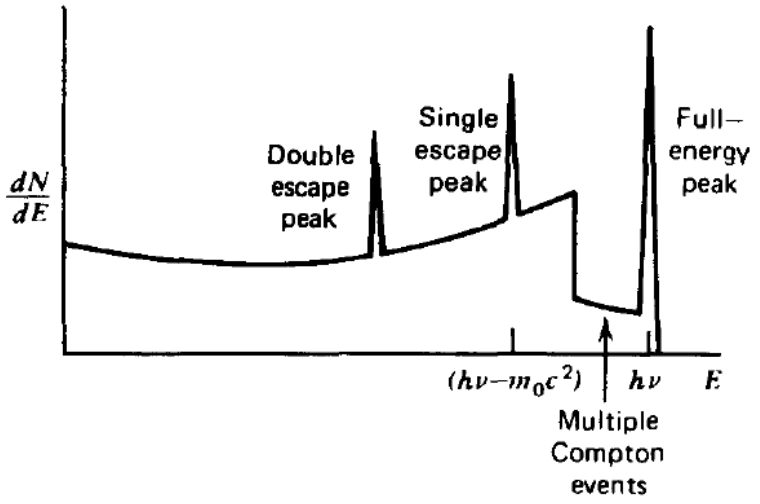

FIGURE 3.19: An idealized spectrum containing all the characteristic features expected from the three main types of gamma-ray interactions, taking place within a 'medium-sized' detector exposed to a source of mono-energetic γ-rays. Figure taken from Ref [56]

Chapter 4

The ^{22}Ne$(p,\gamma)^{23}$Na Reaction

The ^{22}Ne$(p,\gamma)^{23}$Na reaction was studied using the DRAGON recoil separator at the TRIUMF ISAC facility, in Vancouver, Canada. The aforementioned reaction plays an important role in a variety of stellar environments, strongly affecting predicted chemical abundance patterns, and therefore the conclusions drawn from observations regarding stellar evolution. An overview of the astrophysical motivation for studying this reaction is presented in Chapter 1. This chapter will firstly present a discussion of previous studies centred on this reaction, with particular attention paid to the nuclear physics uncertainties that this work aims to resolve. Then, the key components of the analysis procedure will be outlined. This is the first time that this reaction has been studied using inverse kinematics methods, and as such the results presented here are subject to different experimental challenges and sources of systematic uncertainty from those found already in the literature. A total of seven resonances were investigated, as well as the contribution from direct capture.

4.1 Previous Studies

The literature surrounding the ^{22}Ne$(p,\gamma)^{23}$Na reaction as it relates to nuclear astrophysics can be broken down into three main topics of interest:

1. Determining the properties of resonances that have a dominant influence on the reaction rate in particular astrophysical environments.

2. Absolute strength measurements of high-lying resonances that can be used as references for investigating other resonances that are experimentally more difficult to access.

3. Determining the direct capture contribution to the overall reaction rate.

Progress on the first point listed above has only been achieved fairly recently, and so this section will first focus on the last two topics before moving onto low energy resonances. Though low-energy resonances and direct capture are of more astrophysical interest, reference resonances have strong implications for the other two topics - as shall be made clear during the following discussion.

4.1.1 Reference resonances at $E_{c.m.}$ = 1222, 632, 610, and 458 keV

Reference resonances are critical for studying reaction cross sections, particularly if the stoichiometry of the target is a large source of uncertainty. This is especially important when dealing with elements that have multiple stable isotopes, such as neon, where care must be taken to identify and subtract background originating from contaminant reaction channels. The first published data concerning ^{22}Ne$(p,\gamma)^{23}$Na resonance strengths were presented by Meyer *et al.* [64]. The resonances targetted by Meyer *et al.* [64] were previously identified, though their strengths were not quantified, by earlier studies which used this reaction to determine bound state properties in ^{23}Na [65, 66]. All of these studies were performed by impinging a proton beam onto ^{22}Ne-implanted targets. The energies and strengths of several resonances above $E_{c.m.}$ = 400 keV were reported by Meyer *et al.* [64], including the important reference resonance at $E_{c.m.}$ = 458 keV. The authors state that they converted their relative strengths into absolute strengths using the $E_{c.m.}$ = 610 keV resonance, which has a strength of $\omega\gamma = 2.2\pm0.5$ eV, obtained from Du Toit and Mouton in a private communication. It should be noted that, in a publication two years previous, Du Toit *et al.* [65] allude to an experiment to determine the absolute strength of the $E_{c.m.}$ = 610 keV resonance, from which the results had yet to be published. The first reported absolute resonance strength for this reaction was performed by Keinonen *et al.* [67] pertaining to the $E_{c.m.}$ = 1222 keV resonance, for which a value of $\omega\gamma = 10.5 \pm 1.0$ eV was obtained. In that work, the amount of implanted ^{22}Ne in the carbon backed targets was found via Rutherford backscattering of alpha particles. It is perhaps worth pointing out that Keinonen *et al.* report a relative strength for the $E_{c.m.}$ = 610 keV resonance of $\omega\gamma = 2.8 \pm 0.3$ eV, which is in close agreement with the previous adopted value in a compilation by Endt & van der Leun [68].

A lack of proposed reference resonances, particularly for noble gases which often necessitate the use of implanted targets, was commented upon by Longland *et al* [69]. To remedy this, an experiment performed at the Triangle Universities LENA facility was

undertaken to measure the strong $E_{c.m.} = 458$ keV resonance strength via a novel technique involving depth profiling in aluminium. Using this technique, the amount of ^{22}Ne implanted into an aluminium substrate was determined by simultaneously measuring the $^{27}\mathrm{Al}(p,\gamma)^{28}\mathrm{Si}$ reaction, using the $E_{c.m.} = 391$ keV resonance as a reference. A fit to the yield profile from $^{27}\mathrm{Al}(p,\gamma)^{28}\mathrm{Si}$ was used to infer the stoichiometry of the target. The authors opted to use the strength value of $\omega\gamma = 8.63(53) \times 10^{-3}$ eV reported in Ref [70] for the $E_{c.m.} = 391$ keV resonance. However, this value is markedly lower than the weighted average of all literature strength values available for this resonance listed in Ref [71], which is calculated to be $\omega\gamma = 1.03(5) \times 10^{-2}$ eV. Furthermore, since secondary transitions were used to measure the ^{27}Al + p yield, contributions from other resonances must be taken into account as background. The two background resonances referred to by Longland *et al.* [69] are themselves measured relatively to the $E_{c.m.} = 391$ keV reference resonance. Therefore, a change in the absolute strength for the $E_{c.m.} = 391$ will alter the background subtraction for that measurement in a fashion that is non-trivial to account for without the possible need for re-analysis of the data.

The primary direct to ground-state transition was used by Longland *et al.* to measure the $^{22}\mathrm{Ne}(p,\gamma)^{23}\mathrm{Na}$ yield, using the branching ratio quoted in Refs [64, 66] which have no quoted uncertainties. This branching ratio was later re-measured by Kelly *et al.* to give a new revised strength for the 458 keV resonance [72]. A 10-13 % decrease in the ground state branch resulted in a 10% increase in the strength of the 458 keV resonance to $\omega\gamma = 0.583(43)$ eV. The ratio of the 458 keV and 1222 keV resonance strengths was later measured by Depalo *et al.* [73], and found to be consistent with the existing literature. A summary of all the resonance strengths discussed so far is set out in Table 4.1. It is worth emphasizing that all of the aforementioned studies concerned with the 458 keV resonance were carried out with neon implanted targets, and all used the literature strength value for another resonance to determine target stoichiometry. One of the main results presented in this thesis is a set of new absolute strength measurements for key resonances in $^{22}\mathrm{Ne}(p,\gamma)^{23}\mathrm{Na}$ calculated independently from the existing literature. The present work is also independent of issues relating to target stoichiometry and semi-empirical calculators such as `SRIM`, since the stopping power is directly measured by determining the incoming and outgoing beam energies (see Section 4.2.1).

4.1.2 Direct capture

At temperatures relevant for the NeNa cycle in AGB stars the direct capture (DC) process can contribute to the $^{22}\mathrm{Ne}(p,\gamma)^{23}\mathrm{Na}$ reaction rate. The direct capture cross-section was determined over a large range of energies by Görres *et al.* [75], proceeding

$E_{c.m.}$ (keV)	$\omega\gamma(eV)$			
	Depalo [73]	Kelly [72]	Keinonen [67]	Meyer [64]
417.1(8)	$7.9(6) \times 10^{-2}$	$8.8(10) \times 10^{-2}$	-	-
458.3(8)	$6.05(61) \times 10^{-1}$	$5.83(43) \times 10^{-1}$	-	-
610.4(3)	$2.45(18) \times 10^{0}$	-	$2.8(3) \times 10^{0}$	$2.2(5) \times 10^{0}$
631.6(4)	$3.2(10) \times 10^{-2}$	-	-	$2.85(86) \times 10^{-1}$
1222.1(4)	$1.08(7) \times 10^{1}$	-	$1.05(10) \times 10^{1}$	-

TABLE 4.1: Literature strengths for $^{22}\mathrm{Ne}(p,\gamma)^{23}\mathrm{Na}$ resonances with $E_{c.m.} > 400$ keV. The resonance energies are taken from Endt (1990) [74].

from a smaller study by Rolfs *et al* [76]. These studies covered an energy range of $E_{c.m.} \approx 520 - 1530$ keV and were extrapolated down to lower energies by normalizing to DC model predictions [77]. The results were found to be consistent with a constant astrophysical S-factor of $S(E) = 62$ keV b. A 40% uncertainty was later ascribed to this result by Hale *et al.* [78], estimated by combining the quoted statistical measurement uncertainty, choice of optical model input parameters, and quality of the fits to the data. In addition to investigating several low-energy resonances, Kelly *et al.* [79] also performed a direct capture yield measurement at $E_{c.m.} = 406$ keV, finding an effective S-factor in close agreement with previous work. This thesis extends the available data for direct capture more than 100 keV lower in energy, approaching the Gamow window for hot bottom burning (HBB) in AGB stars.

4.1.3 Low-energy resonances at: $E_{cm} = 248$, 181, and 149 keV

Given the high level density in ^{23}Na just above the proton threshold, there has been a consistent expectation that narrow resonances will dominate the $^{22}\mathrm{Ne}(p,\gamma)^{23}\mathrm{Na}$ reaction rate within the Gamow window for the NeNa cycle occurring in AGB stars. The primary purpose of the publications by Görres *et al.* [82] and Hale *et al.* [78] were to investigate, by direct and indirect methods respectively, the presence of strong low energy resonances. However, both of these studies were only able to place upper limits on resonances bellow $E_{c.m.} = 400$ keV, each respectively suffering from either a lack of sensitivity or influence from contaminant reaction channels. More recently, the landscape of this reaction was drastically changed by the discovery of three new low energy resonances at $E_{c.m.}$ =149, 181 and 248 keV, reported by Cavanna *et al.* [83], making use of the ultra low-background environment available at the LUNA (Laboratory for Underground Nuclear Astrophysics) facility, in Gran Sasso, Italy [84]. A windowless gas target filled with isotopically enriched ^{22}Ne gas was used in combination with two HPGe detectors to measure the $^{22}\mathrm{Ne}(p,\gamma)^{23}\mathrm{Na}$ reaction yield over a range of proton

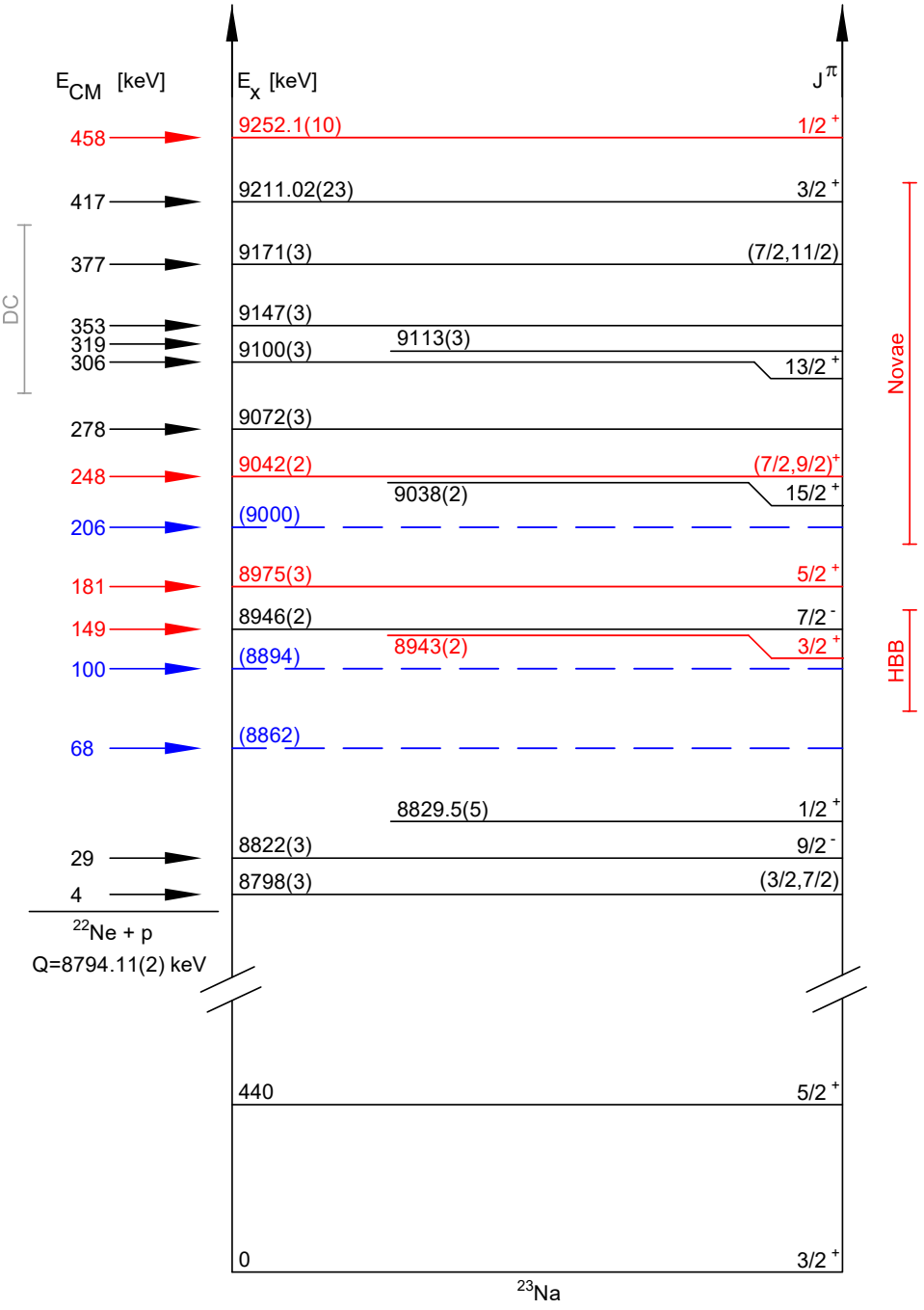

FIGURE 4.1: Partial level scheme of ^{23}Na with labelled ^{22}Ne $+p$ centre of mass resonance energies. The excitation energies, spin-parity assignments, and reaction Q-value were taken from Refs [80–82]. The levels marked with dashed blue lines represent tentative resonances, whereas the red solid lines indicate the resonances considered in this work. The direct capture measurements presented in this work are contained within the grey bracket shown to the left of the diagram (labelled as 'DC'). The Gamow windows corresponding to HBB in AGB stars (100 MK) and for ONe classical novae (400 MK) are indicated by the orange brackets.

energies. While new strengths were found for the aforementioned resonances, no yield was observed from tentative resonances at $E_{c.m} = 68$, 100, and 206 keV [85]. These newly reported resonances resulted in an increase by more than a factor of 10 in the reaction rate at HBB temperatures, with respect to the STARLIB-2013 reaction rate compilation [86].

Results confirming the 149 keV and 181 keV resonances were later published from a separate experiment using the LENA (Laboratory for Experimental Nuclear Astrophysics) $\gamma\gamma$-coincidence spectrometer [87]. Unlike the absolute measurements presented by the LUNA collaboration, the resonance strengths reported by Kelly *et al.* [79] are measured relative to the 458 keV resonance strength. The strengths reported by LENA are considerably higher than the LUNA values, considering the reported uncertainties. However, it was noted by the authors of the LENA study that the measurement uncertainties reported by LUNA do not appear to be compatible with the quoted systematic uncertainties in their experiment, and the statistical uncertainties suggested by the displayed γ-ray spectra; this facet is discussed in more detail during the next chapter in light of the present work.

$E_{c.m.}$ (keV)	$\omega\gamma(eV)$	
	Cavanna *et al.* (2015) [83]	Kelly *et al.* (2017) [79]
149.4(7)	$1.48(10) \times 10^{-7}$	$2.03(39) \times 10^{-7}$
181.2(7)	$1.87(6) \times 10^{-6}$	$2.32(32) \times 10^{-6}$
248.3(6)	$6.89(16) \times 10^{-6}$	-

TABLE 4.2: Literature strengths for low-energy ^{22}Ne$(p,\gamma)^{23}$Na resonances. The resonance energies are taken from Cavanna *et al.* [83].

4.2 Analysis

To directly determine the cross section of a given reaction experimentally, three main quantities must be obtained. Firstly the total integrated number of incident ions must be measured; the method for this employed at DRAGON will be detailed in the next sub-section. Secondly the number density of the target nuclei must be known, which at DRAGON is simply determined from the central pressure and temperature of the gas target and the effective length of the target [49]. Finally the total number of recoil events (N_r^{tot}) arising from the reaction of interest must be inferred from the number of detected recoils (N_r^{det}), taking into account the various efficiencies that affect the detection system. These efficiencies consist of: the BGO γ-ray efficiency $\varepsilon_{\mathrm{BGO}}$, the separator transmission ($\varepsilon_{\mathrm{tran}}$), the charge state fraction ($\varepsilon_{\mathrm{CSF}}$), transmission through

the MCP detectors ($\varepsilon_{\mathrm{MCP}}$), and the DSSSD geometric efficiency ($\varepsilon_{\mathrm{DSSSD}}$). The first two are determined via simulation, whereas the others are directly obtained from prior experiments. The total number of recoils and the reaction yield is given by Equations 4.1 and 4.2 below as:

$$N_r^{tot} = \frac{N_r^{det}}{\varepsilon_{\mathrm{BGO}} \cdot \varepsilon_{\mathrm{tran}} \cdot \varepsilon_{\mathrm{CSF}} \cdot \varepsilon_{\mathrm{MCP}} \cdot \varepsilon_{\mathrm{DSSSD}}} \tag{4.1}$$

$$Y = \frac{N_r^{tot}}{N_b} \tag{4.2}$$

This experiment was carried out over two separately scheduled beam-times undertaken in July and November 2016. Resonance strengths and energies were measured for the six resonances at $E_{c.m.}$ =181, 248, 458, 610, 632 and 1222 keV. Additionally, the direct capture contribution was measured between $282 \leqslant E_{c.m.} \leqslant 530$ keV in the centre-of-mass. Together this is the widest range of energies over-which the $^{22}\mathrm{Ne}(p,\gamma)^{23}\mathrm{Na}$ reaction has been measured by a single experiment, and the first time this reaction has been measured in inverse kinematics. As previously mentioned, the analysis procedure for beam normalization and recoil identification is the same for all the yield measurements performed. For succinctness the E_r = 458 keV resonance will be put forward as a representative example to showcase the important analysis milestones.

4.2.1 Beam Normalization

The total number of incident beam ions is determined by relating hourly Faraday cup readings, taken before and after each data taking run, to the number of elastically scattered protons detected in two silicon surface barrier (SSB) detectors. As described in Section 3.3.2, the DRAGON gas target contains two SSB detectors mounted at 30° and 57° relative to the beam axis. The number of elastically scattered protons is measured over a short time period Δt (nominally 2 minutes) immediately before and after a Faraday cup reading, during which time the beam intensity is approximately constant. From these measurements the so-called Rutherford normalization parameter (or R-factor) is constructed, given below as:

$$R = \frac{I}{eq}\frac{\Delta t}{N_p}\frac{P}{E_b^2} \tag{4.3}$$

Where I is the beam current, scaled by the transmission through the target[1], read by a Faraday cup immediately downstream of gas target. The charge state of the incoming beam ions (q) was 4^+ for all runs. The pressure P and energy of the beam E_b enter into this equation since the Rutherford scattering yield is linearly proportional to the target thickness, and inversely proportional to the square of the energy. By including these terms the R-factor can be applicable to any target pressure or beam energy. The product of the mean R-factor for each yield measurement and the total elastically scattered protons, scaled by the pressure and energy, gives the total number of ^{22}Ne ions on target:

$$N_b = \frac{RN_pE_b^2}{P} \tag{4.4}$$

The primary advantage of this method of beam normalization is to account for small fluctuations in beam intensity throughout individual runs. The typical uncertainty associated with beam normalization for this experiment was on the order of 3%. The beam energy is measured by converting the field of the first dipole magnet (B) as recorded by its NMR probe, using Equation 4.5.

$$\frac{E}{A} = c_{mag}\Big(\frac{qB}{A}\Big)^2 - \frac{1}{2uc^2}\Big(\frac{E}{A}\Big)^2 \tag{4.5}$$

Where E, $A \cdot u$, q are the kinetic energy, mass, and charge state of the beam ions, u is the atomic mass unit (amu), and $c_{mag} = 48.07$ MeV T^2 is a constant related to the effective bending radius of the first dipole magnet [88]. The second term is a relativistic correction that is very small for the beam energies considered for this experiment. If the magnetic rigidity of the incoming beam exceeds the maximum rigidity of the fist dipole magnet, the incident beam energy can be inferred by recording the NMR value with gas in the target at various pressures, and then extrapolating to zero pressure.

4.2.2 Recoil Identification

The ^{23}Na recoils of interest must be separated from scattered or charge-exchanged beam ions that make it through the separator; these are termed 'leaky beam' events. The first stage of recoil identification is to remove any events not correlated with the time structure of the incoming beam (see Section 3.1.2). The RF signal from the RFQ pre-buncher is discriminated and fed into a TDC located in the tail section of the DRAGON DAQ

[1]The gas target transmission is checked after any alteration in the beam-tune delivered to DRAGON. This is done by simply recording the difference in beam current measured immediately upstream and downstream of the target. Typically the transmission is expected to be at least 90%.

system. Since the incident beam ions arrive in bunched packets, the timing of heavy ion events are correlated with the RF signal. This correlation can be visualized by constructing the so-called RF-TOF (radio frequency time of flight) parameter: the time difference between the leading-edges of the RF signal and a timing signal from a heavy ion detector. Normally this parameter is constructed using one of the MCP detectors, which have excellent timing resolution. However, excessive levels of noise rendered the MCPs unusable for this experiment.

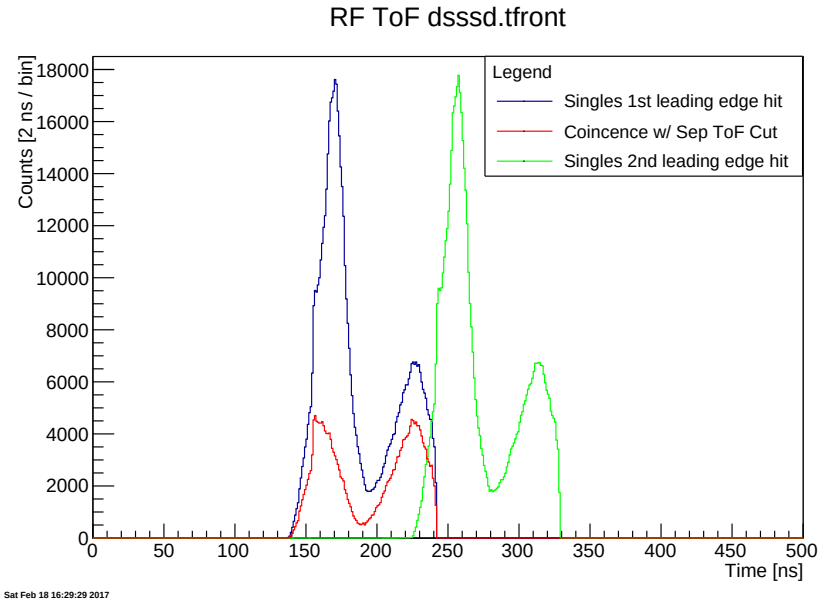

FIGURE 4.2: RF time of flight (RF-TOF) spectrum using the timing signal from the DSSSD front strips. The time difference between the first leading edge hit and a DSSSD hit is shown in blue for singles and red for coincidence events. Shown in green is the same RF-TOF parameter, but instead constructed using the second leading-edge hit.

The RF-TOF parameter using the timing from the DSSSD front strips is shown on Figure 4.2 for the $E_{c.m.} = 458$ keV yield measurement. The distribution is very wide, completely covering the 86 ns period of the RF signal. Candidate ^{23}Na recoils (red) are revealed by making a cut on the separator time of flight, which will be discussed later. The double peak feature is due to the recoil distribution being wide enough such that later events become associated with the next leading edge hit of the RF - note the cut off at 242 ns. Unfortunately the portion of the recoil distribution that is cut-off lies underneath the strong leaky-beam component (for singles events) associated with the next RF pulse. To summarize, Figure 4.2 demonstrates that the focal plane DSSSD lacks the necessary timing resolution to distinguish leaky-beam from recoils. Therefore, without the MCPs extracting the number of recoils obtained in singles using only time-of-flight is not possible.

Distinguishing recoils from leaky-beam background in singles (i.e. a heavy ion detection without a corresponding γ-ray) is perhaps the most challenging aspect of DRAGON data

analysis. For coincident events the task of identifying genuine recoils is made significantly easier by using the *separator time of flight*, i.e. the time difference between a γ-ray and heavy ion detection (Section 3.3.6 provides a more detailed description of coincident events). The separator TOF spectrum provides an unambiguous and extremely clean recoil signal, shown in Figure 4.3. The recoil cut on the separator TOF brackets a region of $\pm 1.5\tau_{RF}$ from the peak centroid, where τ_{RF} is the RF-period of the pulsed beam (86 ns). This cut is chosen in order to include all events that could potentially be beam-correlated.

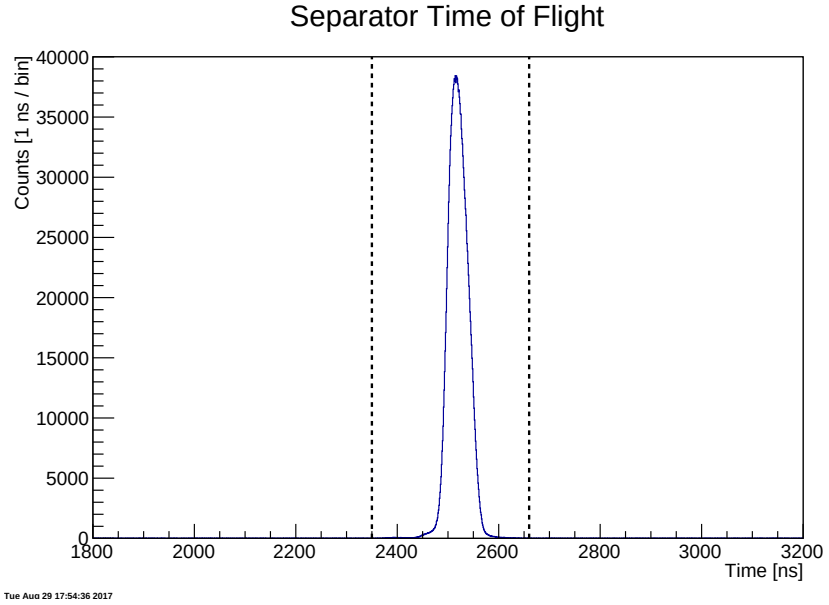

FIGURE 4.3: Separator time of flight spectrum for $E_r = 458$ keV without any applied cuts.

Returning to singles events, without adequate separation in time of flight, the next parameter to explore is the energy loss in the focal plane silicon detector. The calibrated pulse height spectrum for the front strips of the DSSSD is shown on Figure 4.4 for the $E_{c.m.} = 458$ keV yield measurement. From the singles events indicated by the black solid line, three distinct features are clear - highlighted by fitting with a triple Gaussian. The main peak is evidently associated with the recoils of interest, since it persists for coincident events gated on the separator TOF. In contrast, the higher energy peak observed in singles is entirely removed by this cut, which strongly indicates that these events are associated with leaky beam background. Indeed, the un-reacted beam is expected to appear at higher energies than the ^{23}Na recoils. The additional feature at slightly lower energy originates from the extra energy loss incurred by ions traversing an aluminium grid, which covers 2% of detector's surface area [89]. The geometric efficiency for the focal plane DSSSD is $(96.15 \pm 0.15)\%$ [90]. This efficiency accounts for losses from the full-energy peak due to inter-strip gap events, whereby charge is shared between adjacent strips, resulting in incomplete energy collection.

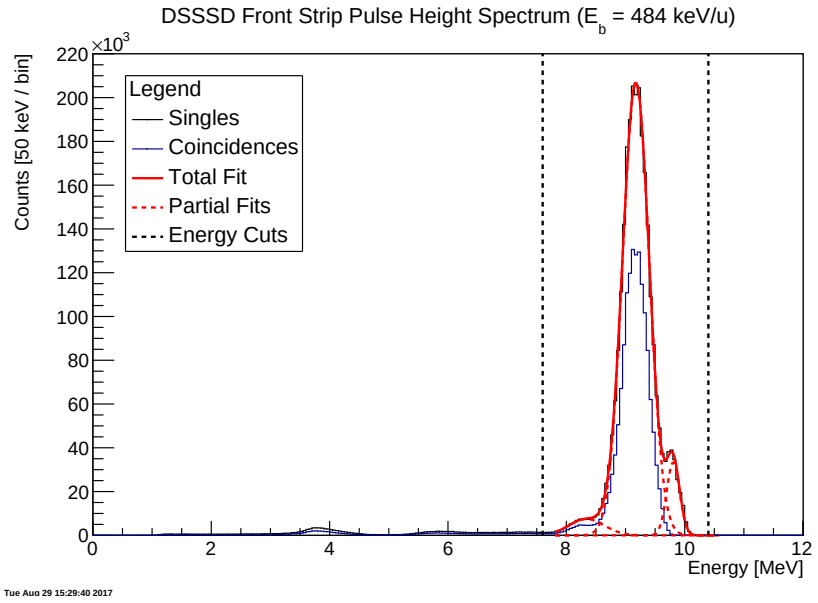

FIGURE 4.4: Pulse height spectrum for the front strips of the DSSSD obtained from the $E_{c.m.} = 458$ keV yield measurement. The energy cuts are imposed around the recoil full-energy peak. The cut is widened towards lower energies so as to include the small number of events passing through the 2% aluminium grid. Losses due to incomplete energy collection caused by events occurring between strips are subsequently accounted for in the analysis by utilizing the $(96.15 \pm 0.15)\%$ geometric efficiency of the DSSSD [90].

4.2.3 Charge State Distribution

Both beam and recoils will exit the gas target with a distribution of charge states. As discussed in Section 3.3, electromagnetic separators such as DRAGON are tuned to transmit ions of a particular m/q to the focal plane. Only one charge state is transmitted, so it is necessary to measure the charge state distribution at the relevant outgoing energies after the recoils pass through the target. The charge state fraction for the transmitted recoils enters into the overall efficiency of recoil detection (see Equation 4.1).

The charge state distributions of ^{23}Na ions passing through the gas target with various incident energies were measured prior to the experiment. The beam energies were chosen to mirror the predicted outgoing energies of ^{23}Na recoils from the $^{22}\text{Ne}(p,\gamma)^{23}\text{Na}$ reaction. The first dipole magnet was then used to scan over the charge state distribution, with the transmitted current measured by a downstream Faraday cup. The distribution of charge states as a function of energy is displayed in Figure 4.5.

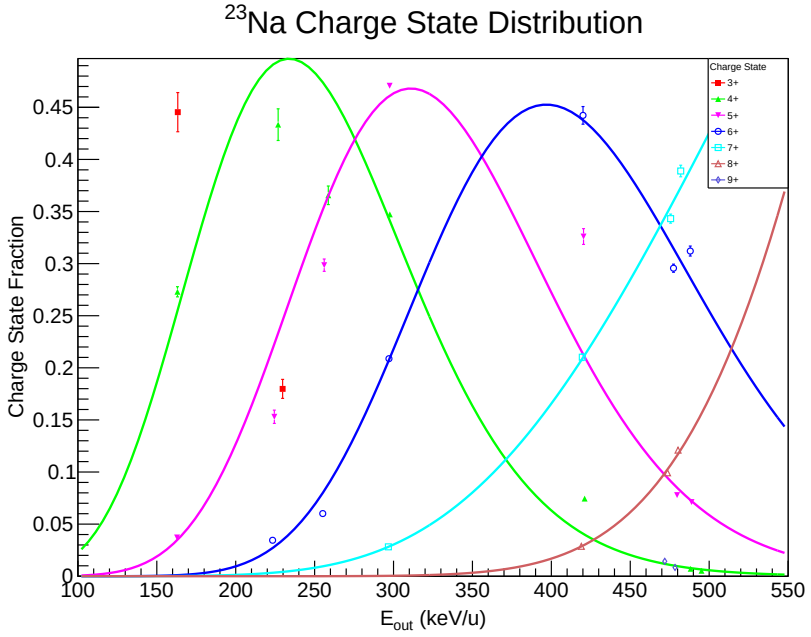

FIGURE 4.5: Measured ^{23}Na charge state distribution determined as a function of outgoing energy from the gas target.

4.2.4 BGO array Efficiency

The efficiency of detecting coincident events must be determined via simulation. A comprehensive simulation of the DRAGON separator and BGO array was created in GEANT3 in order to determine both the BGO efficiency and transmission through the separator. By modifying the input decay scheme, the effect on the BGO array efficiency can be investigated with respect to the characteristics of the γ-decay cascade from the resonance under consideration. The γ-ray detection efficiency is primarily affected by the γ-ray energy and multiplicity. Detection of high energy γ-rays suffers from lower photo-peak efficiency, but if the energy is below the set thresholds then no γ-ray will be detected. Conversely, high multiplicity favours a greater overall detection efficiency as the probability of detecting any one of the emitted γ-rays is high.

The task of accurately simulating the reaction is very straight forward if the decay scheme from the compound nucleus is known. All of the resonances studied in this work have been measured in forward kinematics experiments, in which the γ-rays of interest are directly observed along with their associated branching ratios. A comparison between the observed and simulated γ-ray energy spectra for the 458 keV resonance is shown in Figure 4.6. In the case of resonant capture the intensities of the primary γ-ray transitions were taken from already published data [72, 73, 79]. For direct capture however, the intensities of the primary transitions are unknown and cannot be measured using the DRAGON BGO array due to poor energy resolution. As mentioned in Section 4.1, prior

forward kinematics experiments have measured the contributions of several lower lying states to the direct capture process [75, 79]. The direct capture model described in Ref [77], and the spectroscopic factors found by Görres *et al.* [75], were used to find the relative contributions of the six[1] strongest primary transitions at a given centre of mass energy. These partial cross sections were re-normalized to calculate a branching ratio for each of the contributing states. These primary decay branches, along with subsequent decays taken from Ref [91], were fed into the simulation to determine the coincidence efficiency.

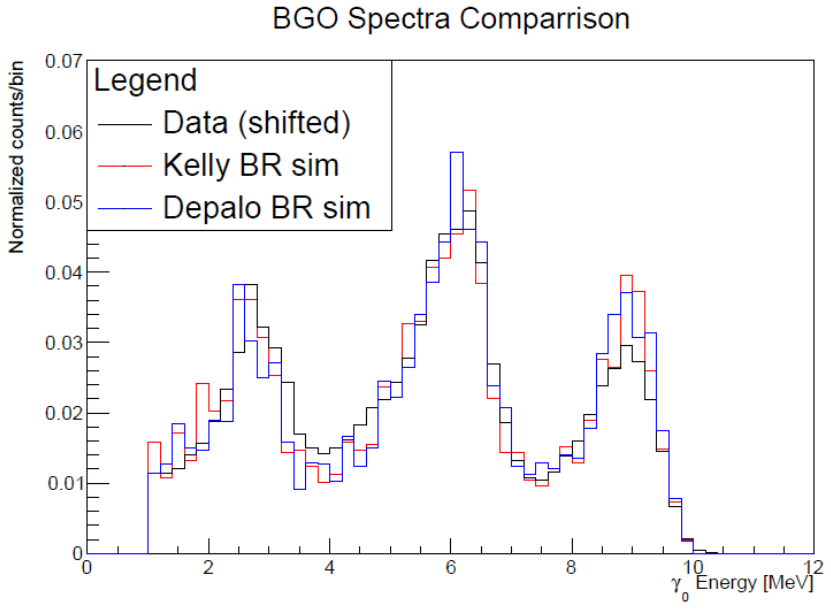

FIGURE 4.6: Comparison between experimental and simulated γ-ray spectra for the $E_{c.m.} = 458$ keV resonance. Two simulated spectra are shown, using the branching ratios determined by Kelly *et al.* (Ref [72]) and Depalo *et al.* (Ref [73]) respectively. The total number of counts in each spectrum is normalized to one for easier comparison.

The uncertainty associated with the extracted partial cross sections was assumed to be commensurate with the 40% relative uncertainty that Hale *et al.* ascribes to the direct capture model inputs, experimental uncertainty, and extracted fit parameters used by Görres *et al.* An in-depth description of how the input primary decay branches were generated is set out in Appendix B. Summarizing here, the BGO efficiency was determined for each DC energy with a total of 30 simulations each. A larger sample of simulation results was deemed unnecessary given that the standard deviation in the acquired coincidence efficiency after 30 samples was already considerably smaller than the systematic uncertainty associated with the simulation itself.

[1] Unfortunately the GEANT3 simulation can only handle upto 6 γ decay branches from the same state

4.2.5 Measuring Resonance Energy

With sufficient statistics it is possible to measure the energy of a resonance at DRAGON from its location within the target inferred from the BGO array hit pattern. A brief overview of how this is done will be set out in this section, though a complete desciption can be found within Ref [88]. As incident beam ions pass through the gas target they lose energy as a function of distance. The pressure of the gas target and the beam energy are selected such that, provided that the resonance in question is narrow, most reactions will occur within a small volume in the centre of the target. The counts observed by each BGO scintillator can be used to form a profile of the reaction vertices along the beam axis. From comparison with experiment, the mean longitudinal position (z_{BGO}) is empirically related to the true location of the resonance (z_{true}) by Equation 4.6. The second term in Equation 4.6 accounts for an asymmetry in the array introduced if the most upstream detectors are pulled back to accommodate additional lead shielding. The lead shielding is only employed for radioactive beam experiments, and hence the second term can be neglected here.

$$z_{BGO} = 0.79 z_{true} + 0.57\ cm \tag{4.6}$$

At the beginning of each yield measurement, the energy loss of the beam across the target was determined by measuring the beam energy before and after filling the gas target. The fraction of the gas target traversed by the beam is defined as:

$$f = 0.5 + {}^{z_{true}}/_{L_{eff}} \tag{4.7}$$

Where L_{eff} is the effective length of the gas target of 12.3 ± 0.5 cm. Note that the above relation only holds within the centre of the gas target, where the target density is approximately uniform. Using the above definition, the beam energy after passing through a fraction f of the target is given by Equation 4.8.

$$E_f = (1-f)E_i + fE_o - f(1-f)\frac{(E_i - E_o)^2}{E_i + Eo}\mathcal{R} \tag{4.8}$$

Where E_i and E_o are the incoming and outgoing beam energies respectively, and $\mathcal{R}$ describes the energy dependence of the stopping power, given as $\mathcal{R} = ({}^{E}/_{S})({}^{\Delta E}/_{\Delta S})$. The stopping power factors for each of the energies considered were calculated using SRIM-2013. The BGO hit pattern observed for the 458 keV resonance is shown in Figure 4.7.

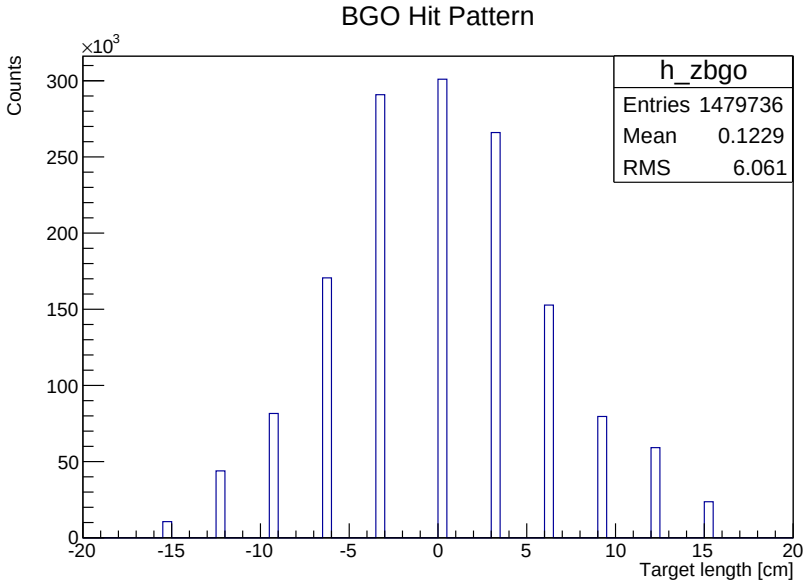

FIGURE 4.7: BGO hit pattern for the $E_{c.m.} = 458$ keV resonance. All coincidence cuts have already been applied.

Chapter 5

^{22}Ne$(p,\gamma)^{23}$Na Results and Discussion

This chapter will present and discuss the results obtained from the first inverse kinematics study of the ^{22}Ne$(p,\gamma)^{23}$Na reaction. Final results from yield measurements of reference resonances, lower energy resonances, and direct capture will first be presented and discussed in the context of the existing literature. A new thermonuclear reaction rate, calculated from the resonance strengths and non-resonant astrophysical S-factor adopted herein, will then be put forward. This will be followed by an assessment of the astrophysical impact, covering both classical novae and AGB star nucleosynthesis. Discussion of the impact will centre around the predicted final abundances, determined through hydrodynamical models concerning each of these astrophysical environments.

5.1 Resonance Strength Measurements

5.1.1 Reference Resonances

Several resonances with centre of mass energies above 400 keV were investigated. Though in most astrophysical environments these resonances are well above the associated Gamow window for important nucleosynthesis processes, they can carry significant influence if used as references to study lower energy resonances. The benefits of performing relative measurements using well known reference resonances is emphasized in Section 4.1. Absolute yield measurements of four such resonances were performed at $E_{c.m.}$ = 1222, 632, 610, and 458 keV. The deduced strengths for each of these resonances, from both singles and coincidence data, as well as existing literature values, are given in Table 5.1.

$E_{c.m.}$ (keV)	$\omega\gamma$ (eV)			
	Literature	Singles	Coincidences	Adopted
458	0.605 ± 0.061 [73] 0.583 ± 0.043 [72]	0.463 ± 0.018	0.473 ± 0.024	0.467 ± 0.014
610	2.45 ± 0.18 [73] 2.8 ± 0.3 [67] 2.2 ± 0.5 [64]		2.79 ± 0.40	2.8 ± 0.24
632	$0.032^{+0.024}_{-0.009}$ [73] 0.285 ± 0.086 [64]	0.581 ± 0.050	0.572 ± 0.027	0.574 ± 0.027
1222	11.03 ± 1.0 [73] 10.5 ± 1.0 [67]	11.7 ± 1.4	12.72 ± 0.74	11.5 ± 0.5

TABLE 5.1: Table of results for ^{22}Ne$(p,\gamma)^{23}$Na resonances with $E_{c.m.} > 400$ keV. The adopted values for the 458 and 632 keV resonance strengths are based on weighted averages of the singles and coincidence measurements presented in this work. The adopted strength values for the 610 and 1222 keV resonances are obtained from a weighted average between the values presented in this work (only coincidences available for the 610 keV resonance) and the only other absolute measurement found in the literature, which was performed by Keinonen *et al.* [67]. Other literature values were not included, since they are all relative measurements that utilize reference resonance strengths that are discrepant with respect to the present work (see text for further discussion). It is important to note the good agreement between singles and coincidence measurements, which gives confidence to measurements where a singles analysis is not possible due to high background.

The adopted strength for the $E_{c.m.} = 1222$ keV resonance was calculated by taking the weighted average between the singles and coincidence measurements presented in the work, and the value put forward by Keinonen *et al.* [67]. The strength value published by Depalo *et al.* [73] was not included, given that the authors normalize their target stoichiometry using a strength for the 458 keV resonance that is discrepant with respect to the present work. Similarly, only the absolute measurements for the 610 keV resonance, performed here and by Keinonen *et al.* [67], were used to calculate its respective adopted strength. Both literature strengths for the 632 keV resonance disagree significantly with the results presented here, and also with each other, particularly the result from Depalo *et al.* [73] which is more than an order of magnitude lower than the previous and current reported values. The authors speculate that the significantly stronger value determined by Meyer *et al.* [64] could have been impacted by contribution from the nearby strong resonance at $E_{c.m.} = 610$ keV. To be confident that the result presented in this work was free from this source of contamination, separate yield measurements were performed with three different gas pressures in the target. If a nearby resonance were heavily influencing the yield then this should be sensitive to target pressure, as well as producing observable artefacts in the data. Table 5.2 indicates no effect on the calculated resonance strength with respect to pressure.

The measured resonance energy for each target pressure, determined via the method

Target Pressure	5 Torr	3 Torr	2 Torr
Singles $\omega\gamma$ (eV)	0.580 ± 0.048	0.548 ± 0.042	0.600 ± 0.049
Coincidences $\omega\gamma$ (eV)	0.581 ± 0.050	0.509 ± 0.040	0.563 ± 0.048

TABLE 5.2: Resonance strengths derived from singles and coincidence data for the $E_{c.m.} = 632$ keV resonance at three different gas pressures.

outlined in Section 4.2.5, is also consistent. The presence of a strong resonance at the entrance or - as would be the case here - exit of the target would skew the resonance energy determined from the BGO hit pattern (displayed in Figure 5.1) as a function of pressure. The resonance energies calculated for each pressure are given in Table 5.3, from which an average of $E_{c.m.} = 631.9(4)$ keV is obtained. This value is in excellent agreement with the literature resonance energy of 631.6(8) keV [74]. The associated error for the present value is conservatively assigned to the total range of measured resonance energies listed in Table 5.3. For completeness, the calculated resonance energy for the 610 keV resonance is listed in Table 5.3, which is also good agreement with the literature [74].

E_{in} (keV/u)	E_{out} (keV/u)	Z_{BGO} (cm)	$E_{c.m.}$ (keV)
660.53(24)	645.22(23)	-1.417	631.7(1)
	650.90(23)	-0.025	632.1(1)
	653.16(24)	1.298	632.0(1)
643.15(23)	627.92(23)	1.525	610.1(1)

TABLE 5.3: $E_{c.m.} = 632$ keV resonance energies determined for three different gas pressures using the BGO hit pattern technique. The average value is calculated to be $E_{c.m.} = 631.9(4)$ keV. The calculated resonance energy for the 610 keV resonance is also shown for completeness.

Furthermore, simple calculations from the measured beam energy loss through the gas target show that, even at the highest pressure used of 5 Torr, the 610 keV resonance is calculated to be 9 cm further downstream of the end of the gas target[1].

The two resonances are further distinguished by their very different γ-decay schemes from their respective excited states in ^{23}Na. For instance, the $E_x = 9404.8$ keV state which gives rise to the 610 keV resonance has a very strong direct-to-ground state branch (78.7%) [91]. Whereas the $E_x = 9426.1$ keV state has a comparatively weak direct-to-ground state branch. The recoil gated BGO spectra for the highest energy γ-rays observed from the two resonances are displayed in Figure 5.2. Clear differences are prevalent in the γ-ray yield around the 8-9 MeV region. Simulated spectra for both resonances are also displayed, which appear to qualitatively reproduce the locations of

[1]This simple calculation assumes a uniform gas pressure over the effective target length and neglects the energy dependence of the stopping power, which is assumed to be a relatively small correction.

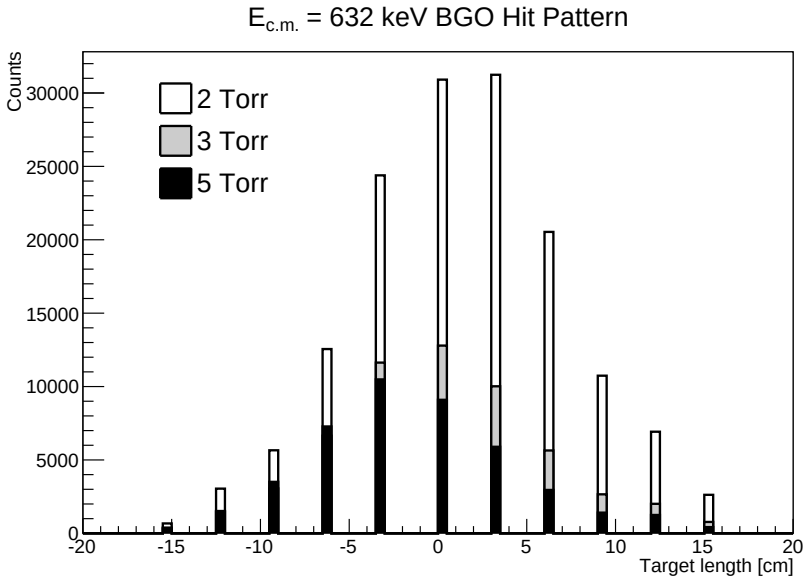

FIGURE 5.1: BGO hit pattern for $E_{c.m.} = 632$ keV with three different target pressures.

the main peaks observed in the data. Taking all of this information into consideration, the adopted value for the $E_{c.m.} = 632$ keV resonance is calculated as the weighted average of the singles and coincidence results obtained from this work. The large discrepancy with respect to the result obtained by Depalo *et al.* [73] is not easily reconciled, given that most systematic effects would impact results from other resonances such as the $E_{c.m.} = 610$ keV where good agreement is found. The strength taken from Meyer *et al.* [64] is measured relatively to the 610 keV resonance strength of $\omega\gamma = 2.2 \pm 0.5$ eV. By re-normalising to the $\omega\gamma = 2.79 \pm 0.4$ eV strength found here then one finds a strength of 0.37 ± 0.11 eV, which lies within 2σ agreement the present value obtained from coincidence data. Unfortunately, contamination from a strong leaky-beam component in the DSSSD energy spectra prevented a singles result from being obtained for this resonance.

The strong narrow resonance at $E_{c.m.} = 458$ keV, in addition to contributing significantly to the thermonuclear rate at temperatures relevant for ONe novae nucleosynthesis, has been proposed as an ideal choice as a reference resonance [69]. Indeed, it has recently been used to infer the strengths of lower energy $^{22}\mathrm{Ne}(p,\gamma)^{23}\mathrm{Na}$ resonances [79]. As discussed in the previous chapter, these newly discovered low energy resonances impact significantly upon the thermonuclear reaction rate at temperatures relevant for Na production in AGB stars undergoing HBB [83]. Therefore it is important that the adopted strength for this resonance is derived from consistent results obtained using a variety of experimental techniques.

The singles and coincidence strengths for the $E_{c.m.} = 458$ keV resonance are given in

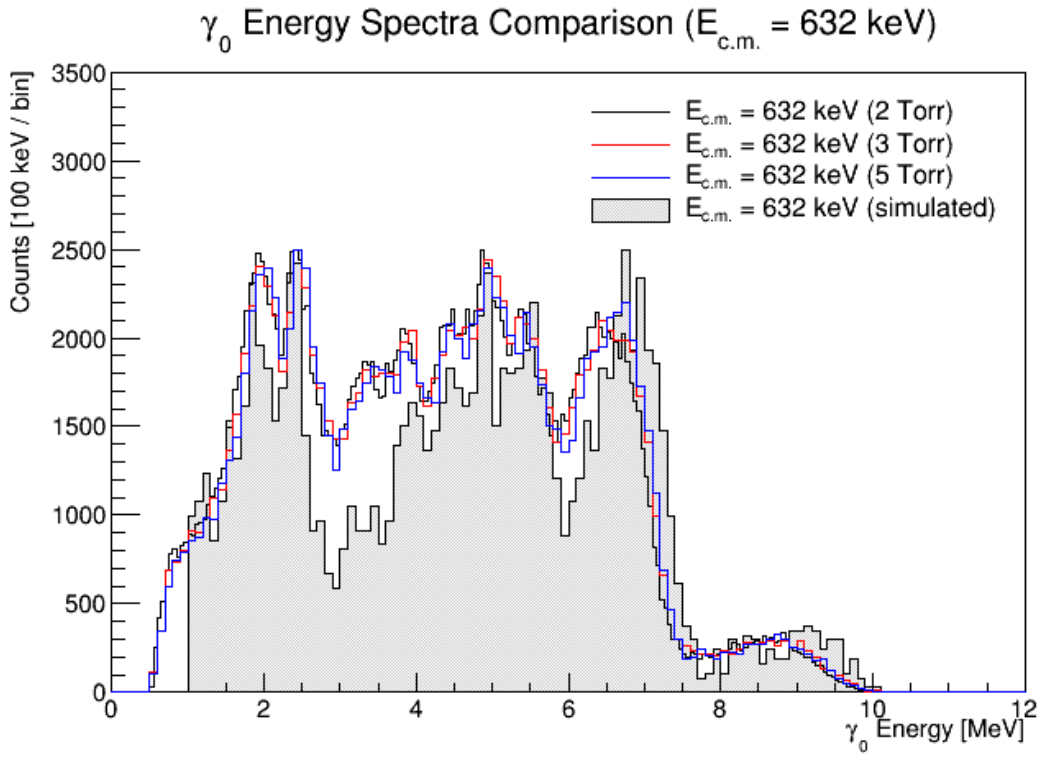

(A) $E_{c.m.} = 632$ keV resonance

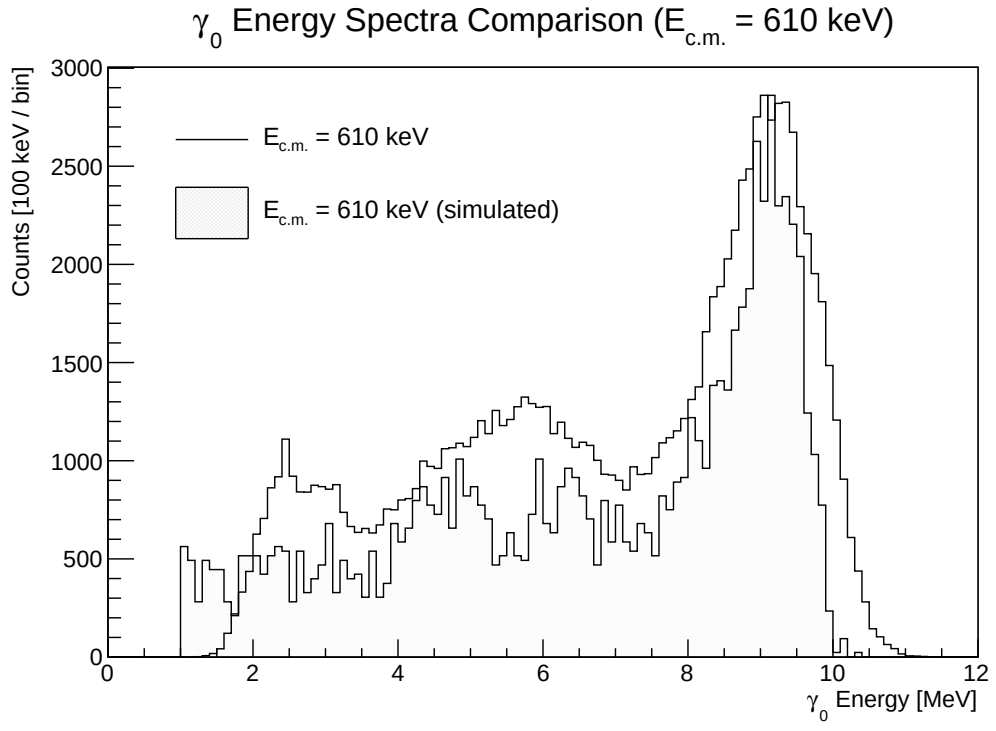

(B) $E_{c.m.} = 610$ keV resonance

FIGURE 5.2: Comparison between simulated and detected highest energy γ-rays for: (A) the $E_{c.m.} = 632$ keV resonance with various target pressures (B) the $E_{c.m.} = 610$ keV resonance.

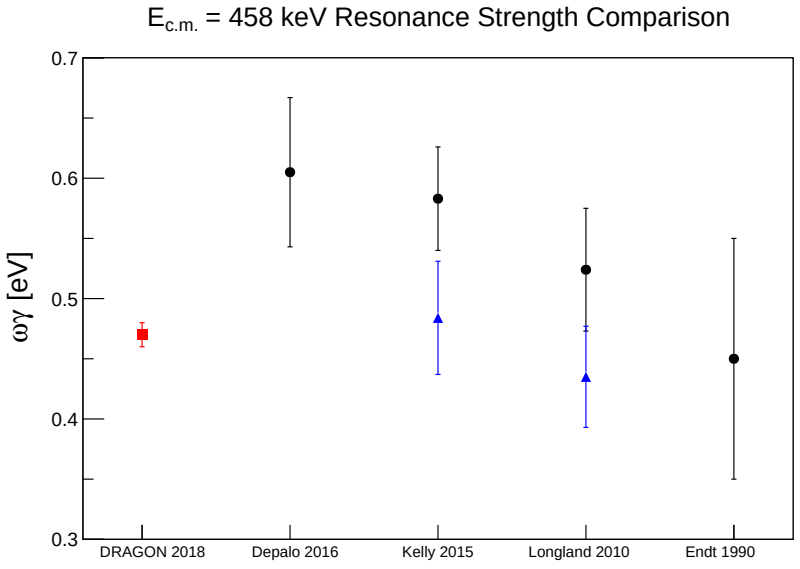

FIGURE 5.3: Comparison of current and previous measurements of the $E_{c.m.}$ = 458 keV resonance strength. The black circles indicate previously published results and the red square shows the current measurement. The blue triangles are the Kelly and Longland results after re-normalising the original Longland result to account for the updated strength for the $E_{c.m.}$ = 391 keV ^{27}Al + p resonance, see text for a detail explanation.

Table 5.1; the average of these is displayed alongside previous measurements on Figure 5.3. The present result is in agreement with the compilation by Endt *et al.* [74], but disagrees significantly with recently published results by Depalo *et al.* [73] and Kelly *et al.* [72]. As stated in Section 4.1, Longland *et al.* [69] uses the $E_{c.m.}$ = 391 keV ^{27}Al + p resonance reported in Ref [70] to determine the target stoichiometry via a novel depth profiling technique. However, the value found in Ref [70] differs significantly from a weighted average of all the published strengths available for this resonance, which can be found in Ref [71]. If one assumes that the depth profiling technique allows for a linear re-normalization of the inferred target content then, using the $\omega\gamma = 0.104(5)$ eV strength from Ref [71], their result is shifted down to $\omega\gamma = 0.435(42)$ eV. Applying the new branching ratio found by Kelly *et al.* [72] for the direct to ground state transition, which is used by Longland *et al.* to identify the ^{22}Ne$(p,\gamma)^{23}$Na events, the 458 keV resonance strength is re-calculated as $\omega\gamma = 0.484(47)$ eV. This value is in excellent agreement with this work for both singles and coincidence measurements in Table 5.1. The adopted strength for the 458 keV resonance of $\omega\gamma = 0.467(14)$ eV was calculated as the weighted average of the singles and coincidence results presented in this work.

The resonance energy was calculated, using the BGO hit pattern method, for each of the seven individual runs comprising this yield measurement. Each run, lasting approximately one hour, contained at least 2×10^5 good coincident recoils and less than 300 estimated background counts within the separator TOF region of interest. This

quality of statistics allows for the resonance energy to be calculated on a run-by-run basis, thereby giving a reasonable account of the point-to-point systematic errors that might arise due to the target pressure and/or beam energy drifting over the entire yield measurement. The BGO hit pattern centroids and calculated resonance energies are listed in Table 5.4. From these results, an average centre-of-mass energy of 457.7(3) keV is calculated. The associated error is conservatively assigned to be the total range of calculated energies.

Run ID	Z_{BGO} (cm)	$E_{c.m.}$ (keV)
1	0.17	457.60
2	0.08	457.75
3	0.15	457.63
4	0.11	457.70
5	0.20	457.55
6	0.12	457.68
7	0.03	457.83

TABLE 5.4: BGO hit pattern centroids and calculated resonance energies for the $E_{c.m.} = 458$ keV resonance. The average is calculated to be $E_{c.m.} = 457.7 \pm 0.3$ keV. The incident beam energy was 483.3 keV/u and the outgoing energy was 466.75 keV/u at an average gas target pressure of 5 Torr.

5.1.2 Low Energy Resonances at $E_{c.m} = 149, 181, 248$ keV

Three new low-energy resonances at $E_{c.m} = 149, 181, 248$ keV were identified by Cavanna *et al.* [83], two of which ($E_{c.m} = 149, 181$ keV) were later remeasured by Kelly *et al.* [79]. The observed resonance strengths from this work, along with those quoted in the literature are listed in Table 5.5. Unfortunately, without functioning MCP detectors to further distinguish recoils of interest, measurements from singles data were not possible for these resonances due to excessive leaky beam background. Tuning at low beam energies is also extremely difficult with DRAGON due to relatively larger beam emittance, which makes scattering off the gas target apertures more likely. This, along with the larger recoil cone angle, stretches the limits of DRAGON's acceptances in energy and angle, leading to lower beam suppression and more uncertain recoil transmission efficiency. Therefore only a coincidence analysis was possible, through which recoils of interest were identified by their characteristic separator time-of-flight signal, along with additional gates on the DSSSD and BGO energy spectra. Even with the application of coincidence cuts, the excessive background meant that no absolute value could be obtained for the strength of the 149 keV resonance, since no signal was observed above background. In fact, this yield measurement was abandoned during the experimental run in favour of additional data collecting on the 181 keV resonance. A request made

by the author and other spokes persons for additional beam time to measure the 149 keV resonance was approved by the TRIUMF experiment evaluation committee and is currently awaiting scheduled beam time.

$E_{c.m.}$ (keV)	$\omega\gamma$ (eV)		
	Literature	This work	Adopted
248	$6.89(16) \times 10^{-6}$ [83, 85]	$8.81(1.35) \times 10^{-6}$	$7.85(1.36) \times 10^{-6}$
181	$1.87(6) \times 10^{-6}$ [83, 85] $2.32(32) \times 10^{-6}$ [79]	$1.41(43) \times 10^{-6}$	$1.70(26) \times 10^{-6}$
149	$1.48(10) \times 10^{-7}$ [83, 85] $2.03(40) \times 10^{-7}$ [79]	-	$1.56(11) \times 10^{-7}$

TABLE 5.5: ^{22}Ne$(p,\gamma)^{23}$Na resonance strengths for low energy resonances at $E_{c.m.}$ = 248, 181, and 149 keV. The adopted values are based on unweighted averages between the present work, LUNA values, and re-normalized LENA values (see Table 5.6).

The 248 keV resonance corresponds to the 9042 keV state in ^{23}Na which was reported as a doublet with another level at 9038 keV [80]. The latter state was assigned a $J^\pi = 15/2^+$ spin-parity, whereas the resonant state in question was assigned to be either $7/2^+$ or $9/2^+$. Two prior direct and indirect studies placed upper limits of $\omega\gamma \leqslant 2.6 \times 10^{-6}$ eV and $\omega\gamma \leqslant 1.3 \times 10^{-6}$ eV respectively [78, 82]. The indirect experiment carried out by Hale *et al.* [78] extract their upper limit assuming the state to have a spin parity of $J^\pi = 7/2^+$. The result presented here is more than 6 times higher than the most recent of these upper limits, but within 2σ agreement of the LUNA result, thus supporting a higher resonance strength than the previously assigned upper limits. As noted by Depalo *et al.* [85], the direct study performed by Görres *et al.* [82] may have missed this narrow resonance due to an insufficient number of energy steps. The authors of the indirect study caution that their assumption of a first order direct process may not be valid for this resonance, thereby calling into question their extracted spectroscopic factor. The adopted strength for this work was therefore calculated as the average of the results presented here and by Depalo *et al.* [85].

The strength reported here for the 181 keV resonance is lower than the previous values reported by the LUNA [83, 85] and LENA [79] groups, albeit much closer to the LUNA value which lies slightly outside of 1σ agreement. In order to extract the total number of detected recoils, reasonably conservative cuts were imposed on the separator TOF and BGO spectra. The separator TOF spectra for both yield measurements centred on the 181 keV and 248 keV resonances are shown by Figure 5.4. Since the 8975 keV state, corresponding to the 181 keV resonance, γ-decays predominantly via the E_x = 6618 keV state to produce a 2357 keV γ-ray; a software-imposed threshold cut at $E_\gamma > 2.0$ MeV largely quenches the leaky beam background. The resulting separator TOF was

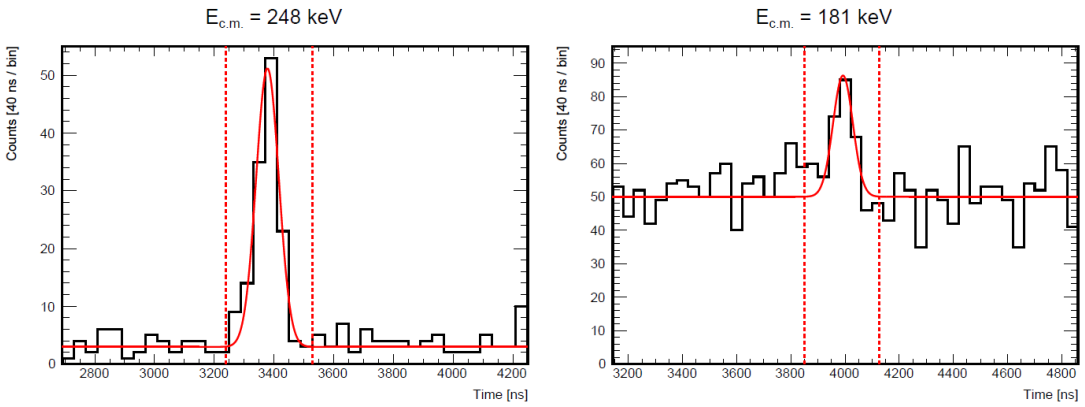

FIGURE 5.4: Separator TOF spectra for the $E_{c.m.} = 248$ keV resonance (left) and the $E_{c.m.} = 181$ keV resonance (right). The red dotted lines indicate cuts bounding the signal region. The separator TOF spectra are each fitted with Gaussian functions over a constant background.

fitted with a Gaussian above a constant background, from which the latter was used to estimate the total background over the signal region. The `TRolke` class in `ROOT` was then used to calculate the 68% confidence limits using the Poisson background model, for a detailed explanation of the Rolke method see Ref [92].

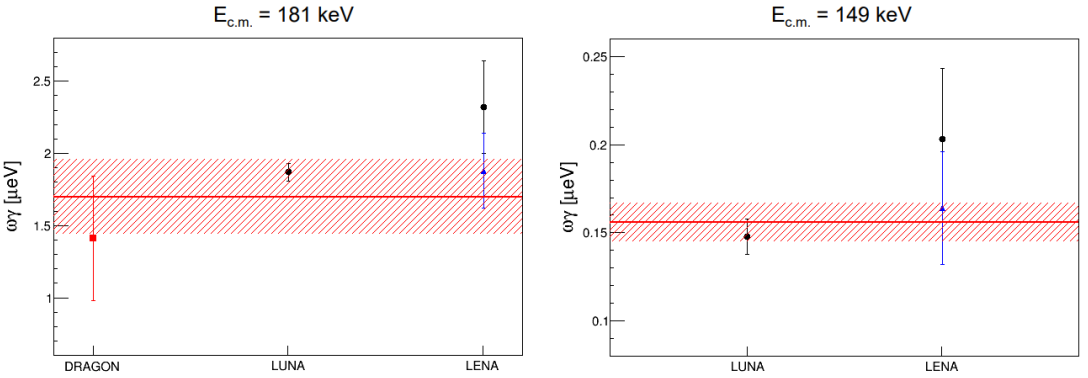

FIGURE 5.5: Strength comparison for the $E_{c.m.} = 181$ keV (left) and $E_{c.m.} = 149$ keV (right) resonances. Previously published values are displayed by black circles, the 181 keV strength determined through this work is shown by the red square, and the blue triangles are the results of Kelly *et al.* after re-normalization to the 458 keV resonance strength adopted in this work of $\omega\gamma = 0.467(14)$ eV. The horizontal red line indicates the adopted value for each resonance given in Table 5.5, with the surrounding hatched region covering their respective 1σ confidence regions.

In light of the significant deviation between the 458 keV resonance strength found in this work and in the literature, it is necessary to reconsider the values put forward by Kelly *et al.* for both the 181 keV and 149 keV resonances [79]. In that work, the strengths associated with these two resonances were determined relatively to the 458 keV resonance strength adopted in Ref [72]. As discussed in the previous sub-section, the reported strength for the 458 keV resonance utilized by Kelly *et al.* may be a significant over-estimation. Re-normalization to the currently adopted 458 keV strength brings the

results obtained by Kelly *et al.* for both the 149 keV and 181 keV resonances into much closer agreement with the LUNA and DRAGON measurements. The re-normalized strengths for the 149 keV and 181 keV resonances are listed in Table 5.6 and plotted on Figure 5.5 (blue triangles). Despite the closer agreement, it is worth reiterating here the issues Kelly *et al.* [79] highlight with regards to the quoted uncertainties in the LUNA measurements. This criticism stems from a comparison between the overall uncertainty (3.2%) and the quoted systematic uncertainties of 3, 1.1 and 1% for the γ-ray detection efficiency, effective gas density, and integrated beam current respectively, yielding an overall systematic uncertainty of 3.3%. This implies a negligible statistical uncertainty, which does not appear to be commensurate with their enclosed γ-ray spectra for both the 149 and 181 keV resonances [83, 85]. Moreover, the authors state that the yield obtained from separate analysis of the two HPGe detectors used in their experiment are only consistent to within 3-14% statistical uncertainty. Therefore the strength adopted for the 181 resonance is calculated from unweighted averages of the DRAGON, LUNA and re-normalized LENA values. The adopted 149 keV resonance strength listed in Table 5.5 is calculated from the unweighted average of the LUNA and re-normalized LENA value.

$E_{c.m.}$ (keV)	$\omega\gamma$ (eV)	
	Kelly (original) [79]	Kelly (re-normalized)
181	$2.32(32) \times 10^{-6}$	$1.88(26) \times 10^{-6}$
149	$2.03(40) \times 10^{-7}$	$1.64(32) \times 10^{-7}$

TABLE 5.6: The strengths for the $E_{c.m.} = 181$ and 149 keV resonances as originally published by Kelly *et al.* and re-normalized values based upon the 458 keV strength found through this work.

5.2 Direct Capture Measurements

In addition to on-resonance yield measurements, several off-resonance data points were recorded in order to determine the non-resonant contribution to the reaction rate. These data points were taken at $E_{c.m.} = 511$, 400, 397, 377, 353, 319, 309, 282 keV, extending the available data for direct capture by more than 100 keV lower in energy than ever previously measured for this reaction, approaching the Gamow window for hot bottom burning in AGB stars. The data points collected at $E_{c.m.} = 377$, 353, 319 and 309 keV correspond to known excited states in ^{23}Na however, no resonant contribution was observed, as is shown by both Figures 5.6 and 5.7.

Unfortunately, no singles analysis was possible for any of the direct capture data points, since the leaky beam contamination at the focal plane was too strong to distinguish

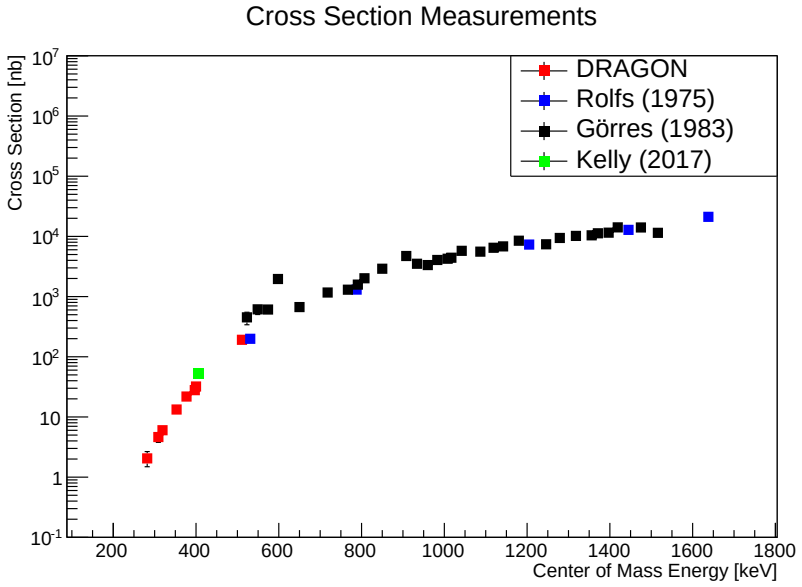

FIGURE 5.6: Plot showing cross section measurements vs energy for the ^{22}Ne$(p,\gamma)^{23}$Na reaction. Literature values are taken from Görres *et al.* (black), Rolfs *et al.* (blue), and Kelly *et al.* (green). The results from this work are displayed in red.

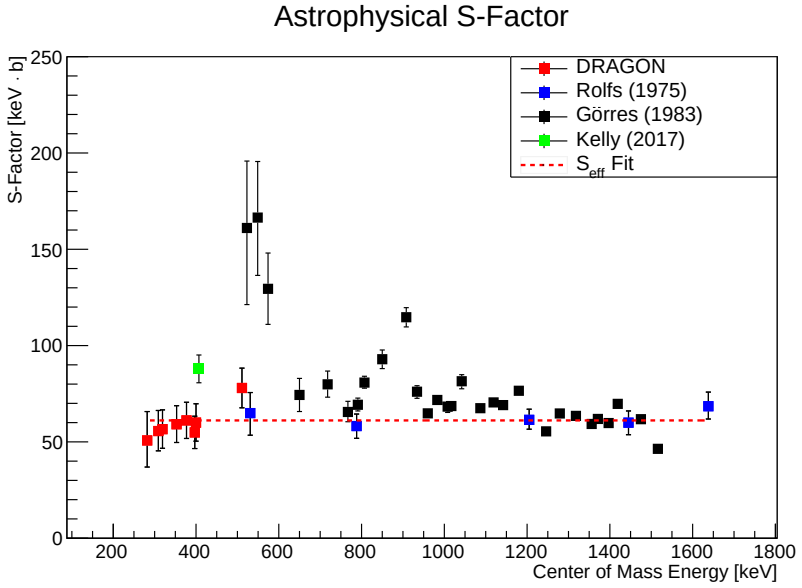

FIGURE 5.7: Plot showing the astrophysical S-factor vs energy for ^{22}Ne$(p,\gamma)^{23}$Na reaction. Literature values are taken from Görres *et al.* (black) [75], Rolfs *et al.* (blue) [76], and Kelly *et al.* (green) [79]. The results from this work are displayed in red.

genuine recoils. Therefore the recoils were instead identified by gating on the separator time-of-flight for recoils and γ-rays detected in coincidence. This necessitated a somewhat different approach towards generating the input decay scheme for the DRAGON simulation in order to estimate the coincidence efficiency. Instead of taking well known decay schemes from the literature (as would be the case for the on-resonance yield measurements), the intensities of the primary γ-ray transitions were instead estimated by

using the direct capture model described in Ref [77] to extrapolate from existing data points published by Görres *et al.* [75] to lower energies. In contrast to resonant capture, the cross section for direct capture is not well localized within the target. So instead of placing a resonance within the target, a 'virtual' resonance was set at some arbitrarily high energy such that the probability of reactions occurring would be uniform across the target length. It is important to do this in order to replicate the transmission through the separator as closely as possible, which strongly depends on the recoil cone angle. A more detailed description of how direct capture is considered for estimating coincidence efficiencies with the DRAGON simulation is outlined in Appendix B.

The non-resonant S-factors found in this work, as well as those found by Kelly *et al.* [79] and Rolfs *et al.* [76] were fit with a constant effective S-factor. The data obtained from Görres *et al.* [75] were excluded from the fit due to anomalous features in the data. The observed fluctuations in the Görres data set were attributed by the author to Ericson fluctuations, which arise due to an interference between direct capture and a sub-threshold resonance [93]. The authors note that these fluctuations were only observed in the direct-to-ground state transition, while no fluctuations were observed for other transitions, which would be unexpected if Ericson fluctuations were responsible. These fluctuations do not appear to persist in the data presented here, nor in any of the other published data sets. The effective S-factor is found to be $S(0)_{eff} = 61.1 \pm 2.2$ keV·b which is consistent with the results found in Refs [75, 76, 79]. The advantage of performing direct capture reactions with the inverse kinematics techniques employed here is that unique identification of γ-ray transitions from direct capture is unnecessary. Assuming that there are no contaminating resonances present in the target, the total number of detected recoils is reflective of the entire yield from direct capture, and so does not require additional interpretation provided by direct capture models to estimate the fraction of yield flowing through lower intensity transitions, which could be lost underneath background. Though it should be noted that the data collected for this case shows that the previous forward kinematics studies were not significantly affected by lost or misidentified transitions.

5.3 Calculating the Reaction Rate

The thermonuclear reaction rate was calculated using the `RATESMC` code [94]. Since there are no interfering resonances to consider, the total reaction rate is given by the sum of the contributions from each resonance as well as direct capture. The input resonance strengths were updated with those listed under 'This Work' in Table 5.1 and 5.5. For results obtained with both coincidence and singles analysis, a weighted average of the

two was used for the rate calculation. In the case of the 149 keV resonance, since no result could be directly obtained from this study, the re-normalized LENA value listed in Table 5.6 was utilized instead. The new strengths for the reference resonances were used to adjust the strengths of higher-lying resonances where needed. The constant S-factor previously employed in the STARLIB-2013 reaction library was updated with the result presented here of $S(0)_{eff} = 61.1 \pm 2.2$ keV·b in order to reflect the much reduced uncertainty obtained through this work. The `RATESMC` code calculates the log-normal parameters μ and σ that together define the reaction rate probability distribution at a given temperature.

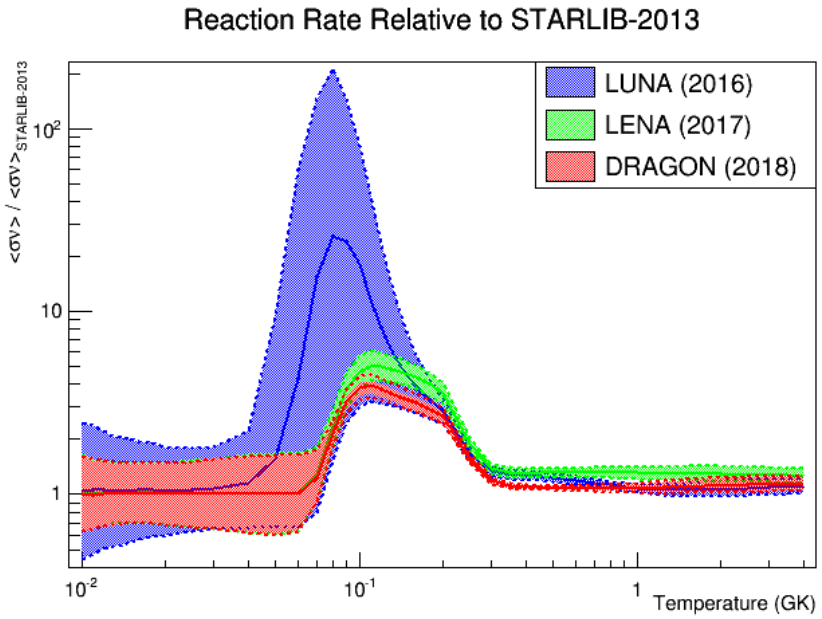

FIGURE 5.8: Comparison of $^{22}\mathrm{Ne}(p,\gamma)^{23}\mathrm{Na}$ reaction rates expressed as a ratio relative to the STARLIB-2013 compilation.

The new reaction rate calculated from this work is plotted relative to the STARLIB-2013 rate in Figure 5.8, alongside the rates published by Depalo *et al.* [85] and Kelly *et al.* [79]. The new reaction rate maps closely with that published by Kelly *et al.*, albeit slightly lower with a peak enhancement over the STARLIB rate of only a factor of 4 instead of 5. It should be pointed out here that the factor of 20 enhancement over the STARLIB rate referred to by Kelly *et al.* is incorrect. Close inspection of the tabulated rate and Figure 19 within Ref [79] reveals that the two rates are not the same. Indeed private communications with the authors revealed that the tabulated rate is the correct rate, and the comparison with the STARLIB rate drawn from their figure is erroneous. Although, the authors stress that the subsequent analysis of abundance predictions were performed using the correct tabulated rate. The large enhancement seen in the LUNA rate in Figure 5.8 is down to the inclusion of tentative resonances at $E_{c.m.} = 68$ and 100 keV, for which only upper limits have been extracted [85].

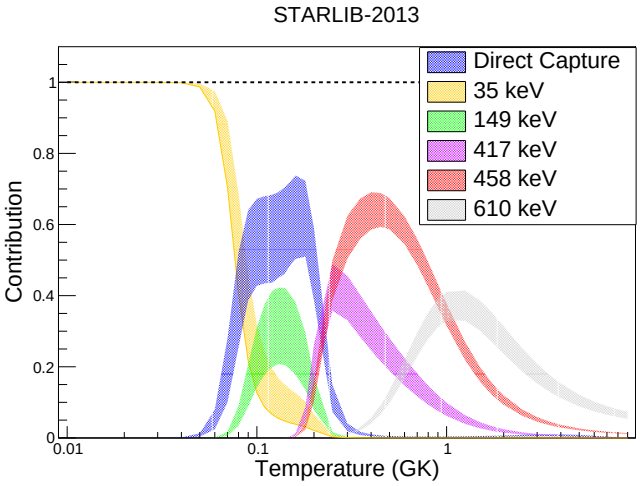

(A) STARLIB-2013 Rate

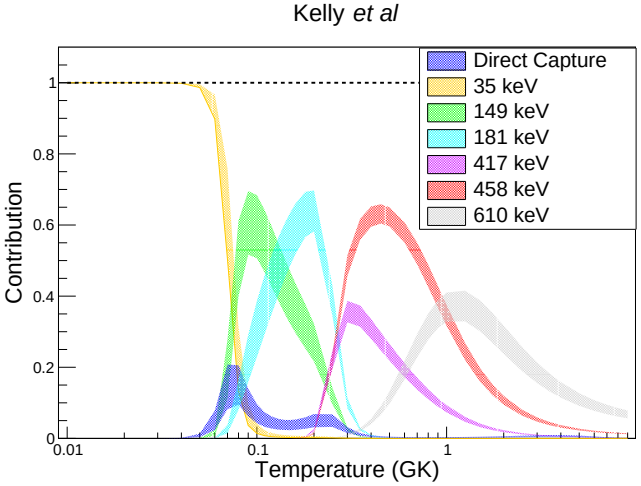

(B) LENA Rate

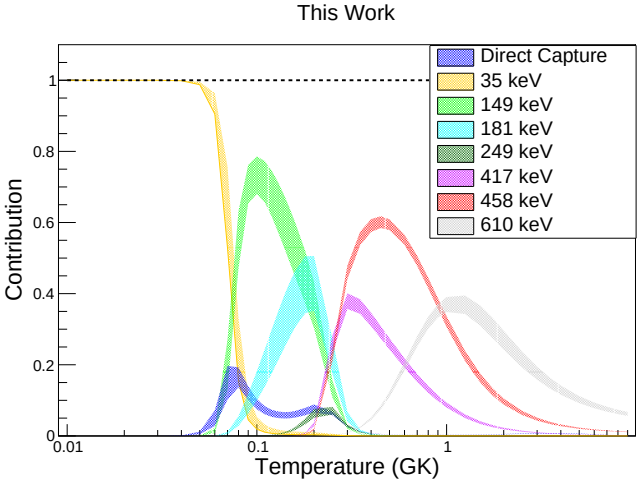

(C) DRAGON Rate

FIGURE 5.9: Relative contribution of resonances to the total ^{22}Ne$(p,\gamma)^{23}$Na reaction rate: (A) STARLIB-2013, (B) Kelly *et al.*, and (C) This Work.

The relative contribution of each resonance to the total reaction rate, including direct capture, is shown by Figure 5.9. Similarly to the results of Kelly *et al.*, the results here show that the contribution of direct capture is much reduced with respect to that suggested by the STARLIB rate.

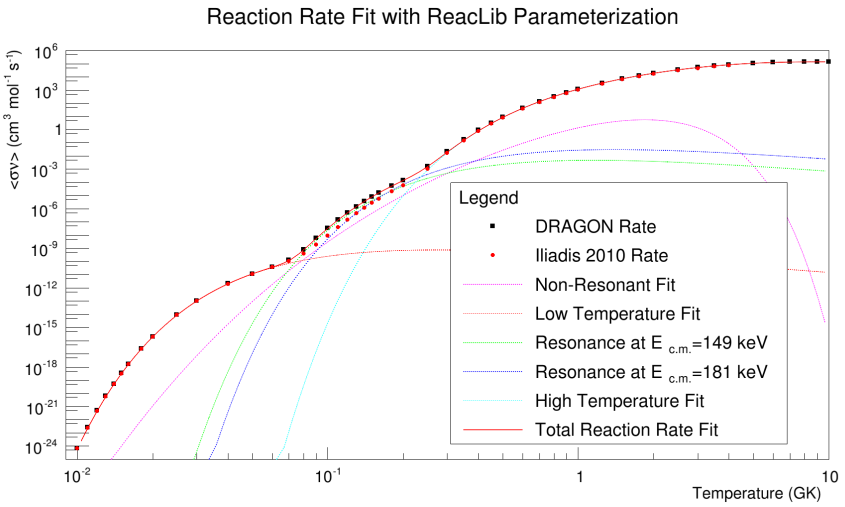

FIGURE 5.10: Fit of the ^{22}Ne$(p,\gamma)^{23}$Na medium reaction rate. Four fit components were necessary to produce the total fit; three resonant components at low, medium and high energy; and one non-resonant component.

In order for the new reaction rate to be implemented into astrophysical models it must first be parametrized in the ReacLib format. The equation for the ReacLib rate parametrization as a function of temperature (T_9) is given by Equation 5.1.

$$\lambda = \exp\left[a_0 + \sum_{i=i}^{5} a_i T_9^{\frac{2i-5}{3}} + a_6 \ln T_9\right] \tag{5.1}$$

Suggested values for each of the constants (a_i) are given on the ReacLib website [95]. The low temperature ($\leqslant 0.065$ GK) behaviour of the rate is largely unaffected, and so the low temperature fit parameters were fixed to those already listed on the ReacLib website. The non-resonant fit function was updated with the slightly lower S-factor found through this work. As indicated by Figure 5.8, significant departure from the previous rate occurs in the temperature range of $0.065 < T_9 < 0.3$ GK. Two resonances corresponding to $E_{c.m.} = 149$ and 181 keV were used to fit the total rate in this temperature region. Initial start parameters for the high temperature fit parameters were taken from those listed on the ReacLib website, and were subsequently allowed to vary by one order of magnitude up and down. The final parameters for the median rate are given by Table 5.7. The tabulated values for the rate agree with the total fit function to within a maximum residual of 6%, which is an acceptable level of error in the context of uncertainties in the final rate (see Appendix C).

	a_0	a_1	a_2	a_3	a_4	a_5	a_6
Low T	-21.4329	-0.4117	0	0	0	0	-1.5
Res 149	-3.62356	-1.73371	0	0	0	0	-1.5
Res 181	-1.47081	-2.10041	0	0	0	0	-1.5
High T	2.26025	-4.40901	0	10.4317	-1.2804	0.0822378	-1.5
Non-res	20.7661	0	-19.431	0	0	-1	-0.6667

TABLE 5.7: Fit parameters used to fit the median ^{22}Ne$(p,\gamma)^{23}$Na rate.

5.4 Astrophysical Impact

5.4.1 Classical Novae

The new ^{22}Ne$(p,\gamma)^{23}$Na reaction rate proposed in this work was implemented in a variety of classical nova models in order to assess the impact on the final predicted abundances contained in the ejected envelope. A total of four models were used: two carbon-oxygen (CO) novae with underlying white-dwarf (WD) masses of 1.0 and 1.15 $M_{\odot}$, and two oxygen-neon (ONe) novae with WD masses of 1.15 and 1.25 $M_{\odot}$. The calculations presented here were not performed by the author, and a detailed description of the nova model used is beyond the scope of this thesis. A detailed description regarding the mechanics of the hydrodynamical code used for these calculations, and the associated inputs for each of these models is provided in Ref [24]. The author gratefully acknowledges the work of Professor Jordi José, of the Universitst Politécnica de Catelunya, for undertaking these calculations, the results of which will be the focus of this discussion.

Nuclide	Mass Fraction			
	STARLIB 2013 [86]	Low Rate	Medium Rate	High Rate
^{20}Ne	1.28×10^{-3}	1.37×10^{-3}	1.35×10^{-3}	1.34×10^{-3}
^{21}Ne	1.45×10^{-7}	1.53×10^{-7}	1.52×10^{-7}	1.51×10^{-7}
^{22}Ne	2.50×10^{-3}	2.32×10^{-3}	2.36×10^{-3}	2.39×10^{-3}
^{22}Na	6.97×10^{-7}	7.32×10^{-7}	7.26×10^{-3}	7.20×10^{-7}
^{23}Na	2.61×10^{-5}	6.58×10^{-5}	5.83×10^{-5}	5.22×10^{-5}
^{24}Mg	1.36×10^{-5}	1.44×10^{-5}	1.43×10^{-5}	1.43×10^{-5}
^{25}Mg	4.02×10^{-4}	4.39×10^{-4}	4.32×10^{-4}	4.26×10^{-4}
^{26}Mg	4.17×10^{-5}	4.22×10^{-5}	4.21×10^{-5}	4.20×10^{-5}
^{26}Al	3.25×10^{-5}	3.46×10^{-5}	3.42×10^{-5}	3.39×10^{-5}
^{27}Al	8.21×10^{-5}	8.33×10^{-5}	8.30×10^{-5}	8.29×10^{-5}

TABLE 5.8: Predicted ejecta mass fractions for a 1.0M$_{\odot}$ CO nova model in the Ne-Al region. Total mass of the ejected envelope is 6.67×10^{28} g or 3.35×10^{-5} M$_{\odot}$. Calculation results assuming the present ^{22}Ne$(p,\gamma)^{23}$Na rate are compared to the STARLIB-2013 median rate [86].

These calculations show that the most wide-spread changes in the ejecta abundances occur for the $M = 1.15 M_{\odot}$ CO novae model, which exhibits changes of more than 10% for ^{20}Ne, ^{21}Ne, ^{22}Ne, ^{22}Na, ^{23}Na, ^{25}Mg, ^{26}Mg, ^{26}Al, and ^{27}Al. The most significant abundance change of any single isotope was ^{23}Na, with approximately a factor of 2 enhancement for both CO nova models. For the ONe nova models, the ^{22}Ne content is reduced by almost a factor of 2 in both cases, while only modest changes are predicted for all other isotopes considered, with the exception of ^{24}Mg which is enhanced by $\sim 15\%$ in the 1.25 $M_{\odot}$ ONe nova model.

Nuclide	Mass Fraction			
	STARLIB 2013 [86]	Low Rate	Medium Rate	High Rate
^{20}Ne	1.42×10^{-3}	1.67×10^{-3}	1.64×10^{-3}	1.60×10^{-3}
^{21}Ne	2.52×10^{-7}	2.96×10^{-7}	2.88×10^{-7}	2.82×10^{-7}
^{22}Ne	2.52×10^{-3}	1.80×10^{-3}	1.87×10^{-3}	1.83×10^{-3}
^{22}Na	7.52×10^{-7}	8.69×10^{-7}	8.50×10^{-3}	8.34×10^{-7}
^{23}Na	1.73×10^{-5}	3.61×10^{-5}	3.32×10^{-5}	3.07×10^{-5}
^{24}Mg	6.13×10^{-6}	6.64×10^{-6}	6.27×10^{-6}	6.22×10^{-6}
^{25}Mg	1.93×10^{-4}	2.69×10^{-4}	2.58×10^{-4}	2.49×10^{-4}
^{26}Mg	1.40×10^{-5}	1.68×10^{-5}	1.63×10^{-5}	1.60×10^{-5}
^{26}Al	5.33×10^{-5}	7.12×10^{-5}	6.86×10^{-5}	6.63×10^{-5}
^{27}Al	2.44×10^{-4}	2.95×10^{-4}	2.87×10^{-4}	2.80×10^{-4}

TABLE 5.9: Predicted ejecta mass fractions for a 1.15 $M_{\odot}$ CO nova model in the Ne-Al region. Total mass of the ejected envelope is 2.86×10^{28} g or 1.44×10^{-5} $M_{\odot}$. Calculation results assuming the present $^{22}Ne(p,\gamma)^{23}Na$ rate are compared to the STARLIB-2013 median rate [86].

Particular attention should be paid to the magnesium isotopic ratios ^{25}Mg/^{24}Mg and ^{26}Mg/^{25}Mg. These ratios have been studied as possible means of identifying pre-solar grains of putative classical nova origin, and to provide model constraints on important factors such as the peak temperature achieved during the outburst. In the case of CO novae, synthesis of Mg is very sensitive to the peak temperature reached, and hence the underlying WD mass [96]. The sensitivity study performed by Iliadis *et al.* [28] showed that the predicted final abundances of ^{24}Mg and ^{25}Mg for the 1.15 $M_{\odot}$ CO nova model change by up to a factor of 5, as a result of varying the $^{22}Ne(p,\gamma)^{23}Na$ rate within its prior uncertainties. The newly determined rate drastically limits the reaction rate uncertainty in the relevant temperature range ($T_{\rm peak} = 170$ MK). Indeed, varying the current rate within its respective low and high uncertainty limits only results in changes of less than 7% for all the Mg isotope mass fractions.

Furthermore, the new rate seems to accentuate differences in the Mg isotope ratios between the 1.0 and 1.15 $M_{\odot}$ models. Compared to the STARLIB-2013 rate, the calculations performed with the new $^{22}Ne(p,\gamma)^{23}Na$ rate result in a 24% increase and a 13%

Nuclide	Mass Fraction			
	STARLIB 2013 [86]	Low Rate	Medium Rate	High Rate
^{20}Ne	1.76×10^{-1}	1.76×10^{-1}	1.76×10^{-3}	1.76×10^{-1}
^{21}Ne	3.89×10^{-5}	3.89×10^{-5}	3.89×10^{-5}	3.89×10^{-5}
^{22}Ne	6.51×10^{-4}	3.20×10^{-4}	3.58×10^{-4}	3.93×10^{-4}
^{22}Na	1.42×10^{-4}	1.42×10^{-4}	1.43×10^{-4}	1.42×10^{-4}
^{23}Na	1.01×10^{-3}	1.01×10^{-3}	1.04×10^{-3}	1.00×10^{-3}
^{24}Mg	1.44×10^{-4}	1.42×10^{-4}	1.52×10^{-4}	1.42×10^{-4}
^{25}Mg	3.52×10^{-3}	3.57×10^{-3}	3.56×10^{-3}	3.54×10^{-3}
^{26}Mg	2.98×10^{-4}	3.01×10^{-4}	3.04×10^{-4}	2.98×10^{-4}
^{26}Al	9.94×10^{-4}	1.01×10^{-3}	9.98×10^{-4}	1.01×10^{-3}
^{27}Al	8.54×10^{-3}	8.63×10^{-3}	8.59×10^{-3}	8.62×10^{-3}

TABLE 5.10: Predicted ejecta mass fractions for a 1.15 $M_\odot$ ONe nova model in the Ne-Al region. Total mass of the ejected envelope is 4.89×10^{28} g or 2.46×10^{-5} $M_\odot$. Calculation results assuming the present ^{22}Ne$(p,\gamma)^{23}$Na rate are compared to the STARLIB-2013 median rate [86].

decrease in the ^{25}Mg/^{24}Mg and ^{26}Mg/^{25}Mg isotopic ratios respectively for the 1.15 $M_\odot$ model[1]. However, no significant change is seen for the Mg isotopes in the 1.0 $M_\odot$ model. This result could potentially be of interest for using Mg isotopic ratios in pre-solar grains as a thermometer for the peak temperatures reached during the outburst. Further work should be undertaken to reassess the sensitivity of magnesium isotopic ratios in CO novae to current nuclear reaction rate uncertainties in the Ne-Al region, incorporating the new ^{22}Ne$(p,\gamma)^{23}$Na rate and associated uncertainties.

Enhanced Neon content in meteoritic samples has historically been proposed as a fingerprint for identifying pre-solar grains of classical nova origin, particularly in terms of excess ^{22}Ne content associated with the decay of ^{22}Na [97]. The ^{20}Ne/^{22}Ne isotopic ratio is also of interest for distinguishing between CO and ONe novae; the latter are expected to have very large ratios of ^{20}Ne/^{22}Ne > 100, whereas CO novae models yield ratios of ^{20}Ne/^{22}Ne < 1 [96]. The present rate leads to more efficient destruction of ^{22}Ne by approximately a factor of 2 over the previous rate, while leaving the mass fraction of ^{22}Na released in the ejecta completely untouched. Therefore, enhancement of ^{22}Ne in pre-solar grains is predicted to be even more clearly associated with the decay of ^{22}Na from a nucleosynthesis standpoint, while also resulting in a ^{20}Ne/^{22}Ne ratio that is even more anomalous relative to the solar isotopic ratio of ^{20}Ne/^{22}Ne = 14.

[1]The isotopic ratios calculated for the 1.15 $M_\odot$ CO model with the previous rate were: ^{25}Mg/^{24}Mg $\approx$ 31 and ^{26}Mg/^{25}Mg $\approx$ 0.07. The ratios calculated with the new rate are: ^{25}Mg/^{24}Mg $\approx$ 41 and ^{26}Mg/^{25}Mg $\approx$ 0.06.

Nuclide	Mass Fraction			
	STARLIB 2013	Low Rate	Medium Rate	High Rate
^{20}Ne	1.78×10^{-1}	1.79×10^{-1}	1.79×10^{-3}	1.79×10^{-1}
^{21}Ne	3.64×10^{-5}	3.64×10^{-5}	3.64×10^{-5}	3.64×10^{-5}
^{22}Ne	1.30×10^{-3}	7.53×10^{-4}	8.23×10^{-4}	8.89×10^{-4}
^{22}Na	1.74×10^{-4}	1.74×10^{-4}	1.75×10^{-4}	1.74×10^{-4}
^{23}Na	1.11×10^{-3}	1.13×10^{-3}	1.15×10^{-3}	1.12×10^{-3}
^{24}Mg	1.08×10^{-4}	1.09×10^{-4}	1.24×10^{-4}	1.13×10^{-4}
^{25}Mg	2.27×10^{-3}	2.33×10^{-3}	2.32×10^{-3}	2.30×10^{-3}
^{26}Mg	1.67×10^{-4}	1.74×10^{-4}	1.77×10^{-4}	1.71×10^{-4}
^{26}Al	5.76×10^{-4}	5.76×10^{-3}	5.71×10^{-4}	5.77×10^{-3}
^{27}Al	4.53×10^{-3}	4.51×10^{-3}	4.50×10^{-3}	4.52×10^{-3}

TABLE 5.11: Predicted ejecta mass fractions for a 1.25 $M_\odot$ ONe nova model in the Ne-Al region. Total mass of the ejected envelope is 3.75×10^{28} g or 1.89×10^{-5} $M_\odot$. Calculation results assuming the present ^{22}Ne$(p,\gamma)^{23}$Na rate are compared to the STARLIB-2013 median rate [86].

5.4.2 AGB Stars

The rate calculated through this work was implemented in a series of nucleosythesis network calculations performed using the NuGrid multi-zone post-processing code `MPPNP` [98]. Three stellar models were considered for this work, each generated using the stellar evolution code `MESA` [99] and evolved up to the AGB phase. The author gratefully acknowledges the work of Dr Umberto Battino of the University of Edinburgh for generating these calculations.

The $5M_\odot$ ($z = 0.006$) model was used to assess the impact of the present rate, using the STARLIB-2013 rate as the control [86], for hot bottom burning in thermally pulsing AGB stars. Additional simulations of low mass AGB stars were also performed to assess the impact of the presemt rate on the formation of the so-called sodium pocket [100, 101]. In low mass AGB stars of solar metallicity recent stellar models predict that the sodium pocket should be a major source of ^{23}Na, and overproduction of ^{23}Na is thought to be related to ingestion of the sodium pocket during third dredge-up [100].

Despite a factor of 4 enhancement at $T = 100$ MK over the previous rate, there appears to be very little impact on ^{23}Na production during HBB in the $5M_\odot$ TP-AGB star model. This is in contrast with the significant enhancement (factor 3) obtained from similar calculations using the LUNA rate, which was investigated by Slemer *et al.* [102]. This is most likely a consequence of including the upper limits for the $E_{c.m.} = 68$ and 100 keV

[1] S-process elements include all stable isotopes of Sr, Y, Zr, Ba, La, Nd, and Sm. The abundances of s-process elements are essentially measures of time spent along the AGB as neutrons are provided by the ^{13}C$(\alpha,n)^{16}$O and ^{22}Ne$(\alpha,n)^{25}$Mg reactions between thermal pulses.

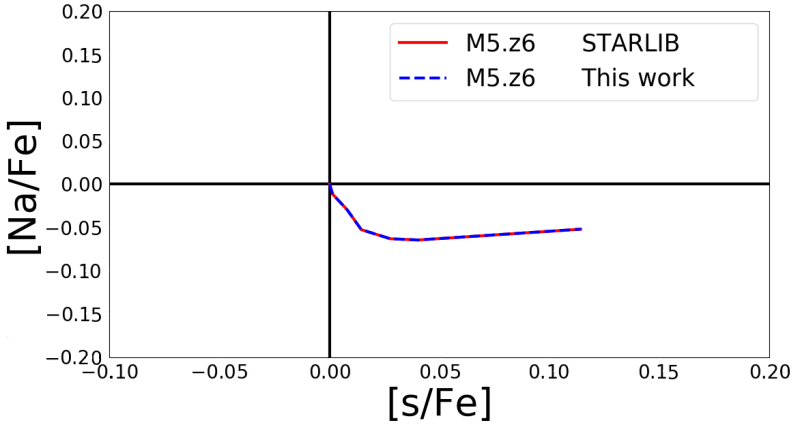

FIGURE 5.11: Predicted surface [Na/Fe] abundance ratio plotted as a function of S-process element abundances[1] [s/Fe] for a $5M_{\odot}$ ($z = 0.006$) AGB star.

resonances in the LUNA rate. The upper limit was included in their rate calculation by sampling Poisson distributions of the signal and background separately, and excluding negative values when taking the difference. Though this method would indeed produce a probability density distribution, and therefore a median rate to implement, it is not clear how the total 'signal' yield was evaluated without the ability to identify any of the primary γ-rays from the resonance in question. The current rate can however provide a more robust lower limit for the ^{22}Ne$(p,\gamma)^{23}$Na reaction. Efforts towards improving the current uncertainties on the ^{22}Ne$(p,\gamma)^{23}$Na reaction rate should focus on obtaining resonance parameters associated with the 68 and 100 keV resonances.

The formation of the sodium pocket also appears to be negligibly affected by the change in the ^{22}Ne$(p,\gamma)^{23}$Na rate. Figure 5.12 shows the mass fraction of various elements as a function of mass co-ordinate, calculated with the SRARLIB-2013 rate for the $2M_{\odot}$ Z=0.006 model. The orange dash-dotted line shows the sodium pocket calculated with the present rate, which is barely changed from the previous rate. The resulting small effect on the surface [Na/Fe] ratio is shown by Figure 5.13. No discernible difference in the surface Na abundance could be seen for the lower metallicity (Z=0.001) model.

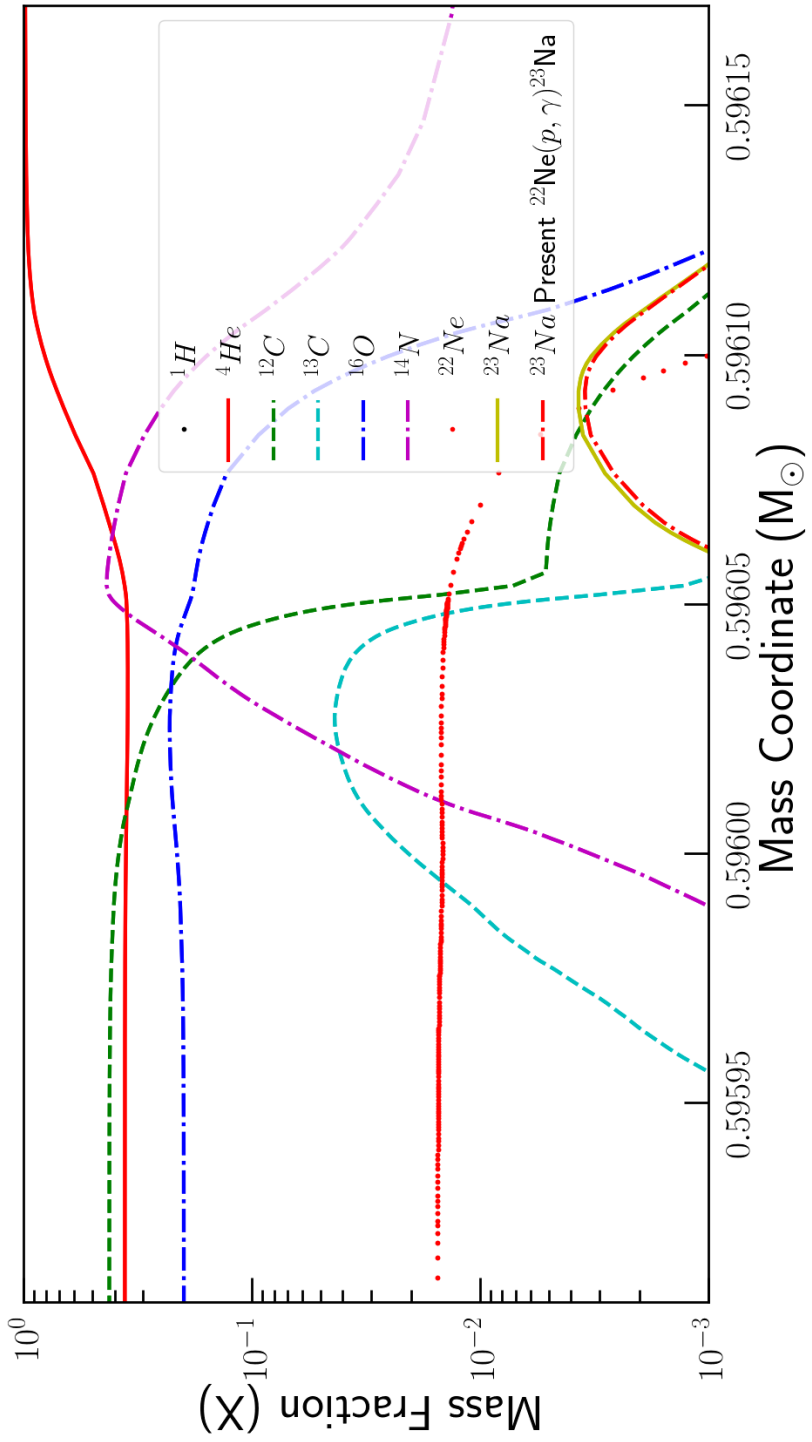

FIGURE 5.12: Mass fractions as a function of mass co-ordinate for a variety of isotopes calculated for a $2M_{\odot}$ ($z = 0.006$) AGB star using the STARLIB-2013 rate. Two ^{23}Na mass fractions are shown, one associated with the previous rate (yellow) and the other calculated for the present rate (orange). The difference in the sizes of the ^{23}Na pockets between the two rate inputs is minuscule.

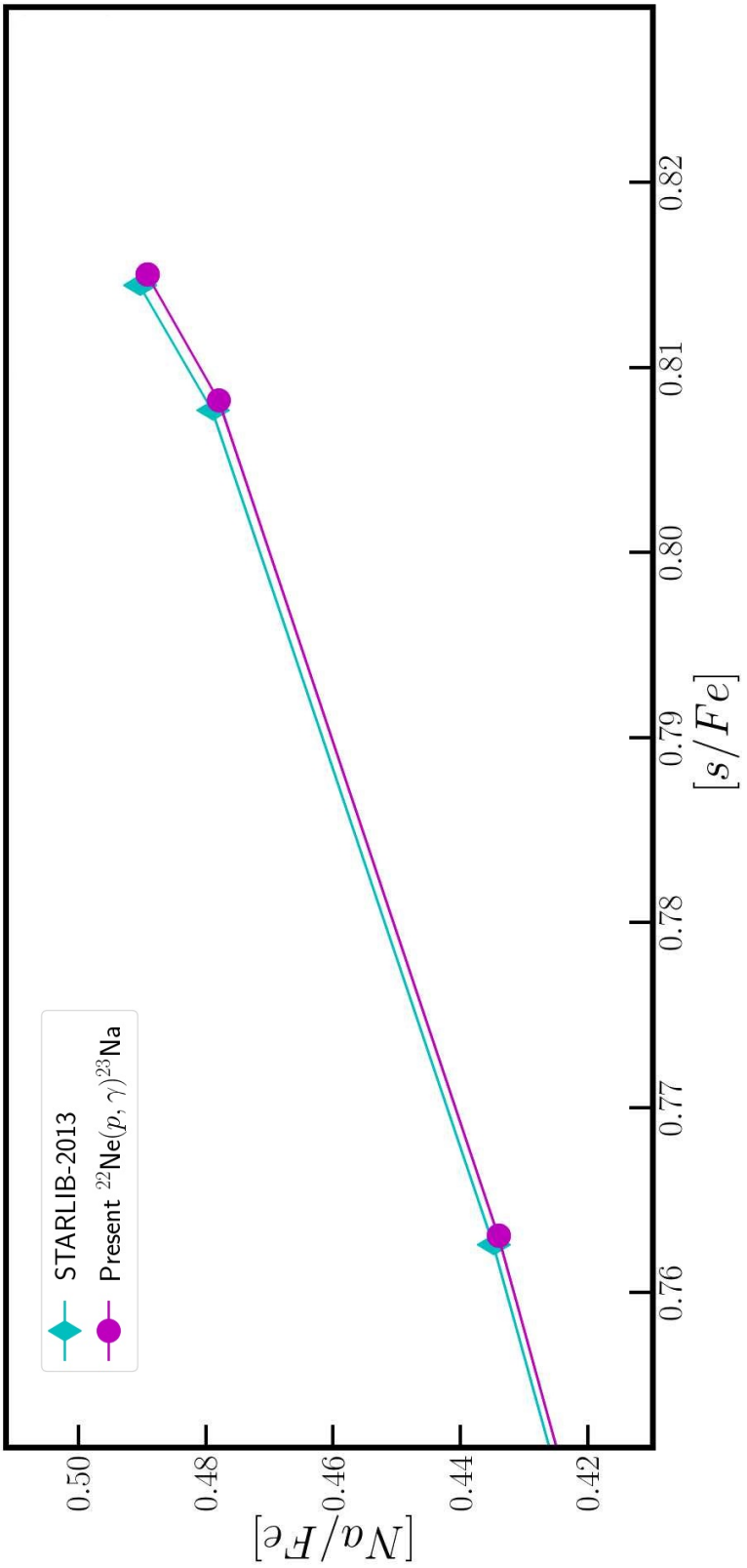

FIGURE 5.13: Predicted surface [Na/Fe] abundance ratio plotted as a function of S-process element abundances [s/Fe] for a $2M_{\odot}$ ($z = 0.006$) AGB star.

Chapter 6

Commissioning of EMMA

The Electromagnetic Mass Analyser (EMMA) was commissioned in a series of alpha source measurements, as well as in-beam testing, between December 2016 and the submission date of this thesis, with further commissioning tests planned for the summer of 2018. The purpose of these tests is to compare the performance of the spectrometer with its design expectations [42]. The design expectations were calculated with the ion optics code GIOS [45]. Experimentally important quantities were measured as part of this work, including: the mass/charge (m/q) acceptance and resolving power, angular and energy/charge (E/q) acceptances, and beam suppression. During the course of these measurements, several investigations were undertaken to optimise the ion optics. For instance, altering the location of the magnetic dipole with respect to the beam axis, adjusting the strength of the dipole fields to better centre ions on the optical axis, and changing the quadrupole field strengths.

This chapter begins by presenting the most up to date results from alpha source testing after optimization of the ion optics. It is these results contained in Section 6.1 which will ultimately be used to estimate realistic transmission efficiencies for future EMMA experiments. The first in-beam commissioning exercise, which preceded alpha source testing, is then discussed in Section 6.2. Results obtained from a more extensive in-beam elastic scattering experiment are discussed in Section 6.3. The performance of EMMA in a fusion evaporation experiment, which also involved the first radioactive ion beam delivered to EMMA, is presented in Section 6.4. Finally, the procedure and results from the previously mentioned ion optics optimization exercises are outlined in Section 6.5.

6.1 Alpha source test studies

6.1.1 Mass dispersion and acceptance

EMMA is designed to separate the products of nuclear reactions and disperse them on to the focal plane in accordance with their respective mass/charge (m/q) ratio. This allows for the identification of reaction channels of interest and suppression of unwanted background. The spatial dispersion of these products at the focal plane is designed to be linear with respect to their deviation from the central m/q setting. With default tune settings, the m/q dispersion at the focal plane is designed to be 10 mm / %[1]. The fractional m/q deviation with respect to the central tune is given by equation 6.1.

$$\delta m = \frac{(m/q) - (m/q)_0}{(m/q)_0} \tag{6.1}$$

Where $(m/q)_0$ is the central m/q setting corresponding to transmission along the optic axis, and (m/q) is the mass/charge ratio of the transmitted ions.

The dispersion can be readily measured using an alpha source at the target location and purposefully mis-tuning the spectrometer with respect to the m/q of the alpha particles. Figure 6.1 shows the mean horizontal position of transmitted alpha particles as a function of δm. The data of Figure 6.1 were fit with a third order polynomial, from which a dispersion of (10.14 ± 0.04) mm/% is found. The slightly non-linear behaviour at large δm is likely a consequence of the reduced transmission at the limits of the m/q acceptance.

All mass spectrometers have a finite mass acceptance limited by the dimensions of the spectrometer, whereby ions that deviate in m/q by more than a certain amount with respect to the central tune will collide with the walls of the device and be lost. According to initial design specifications the m/q acceptance of EMMA should be approximately $\pm 4\%$ [42]. The transmission as a function of δm was measured simultaneously with the dispersion test by recording the count rate for each run. The count rate relative to the central tune is shown by Figure 6.2, which clearly illustrates the limits of EMMA's m/q acceptance.

The m/q transmission is almost uniform in the range of $\pm 3\%$, but then drops off beyond this. It is important to note that the data used for both Figure 6.1 and 6.2 were collected with no restricting aperture at the entrance of EMMA. Therefore the angular distribution of the alpha particles entering EMMA will exceed the angular acceptance.

[1] The focal plane mass dispersion can be varied by altering the strength of Q4 and changing the other quadrupole field strengths to compensate.

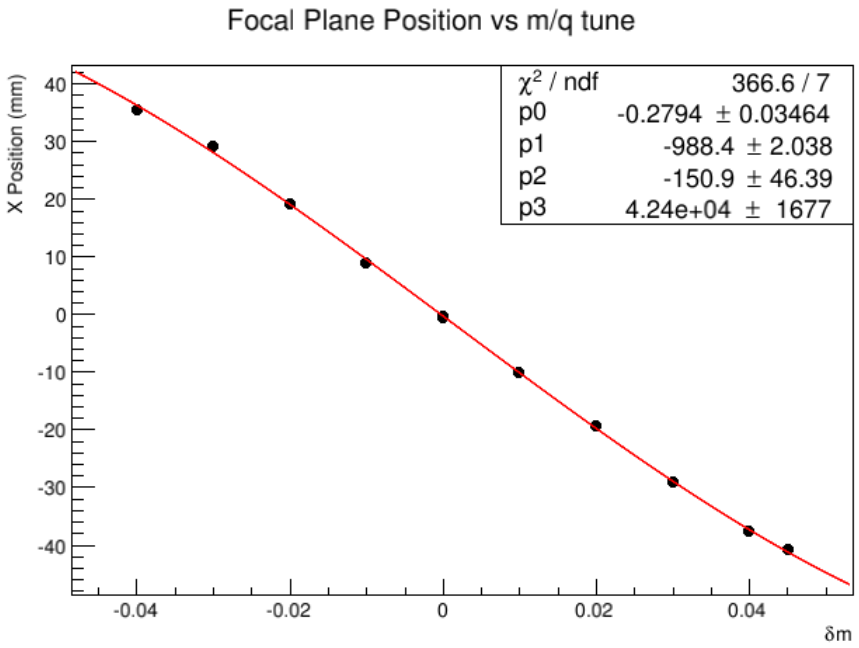

FIGURE 6.1: Plot showing the mean horizontal focal plane position of transmitted α-particles vs m/q tune setting δm

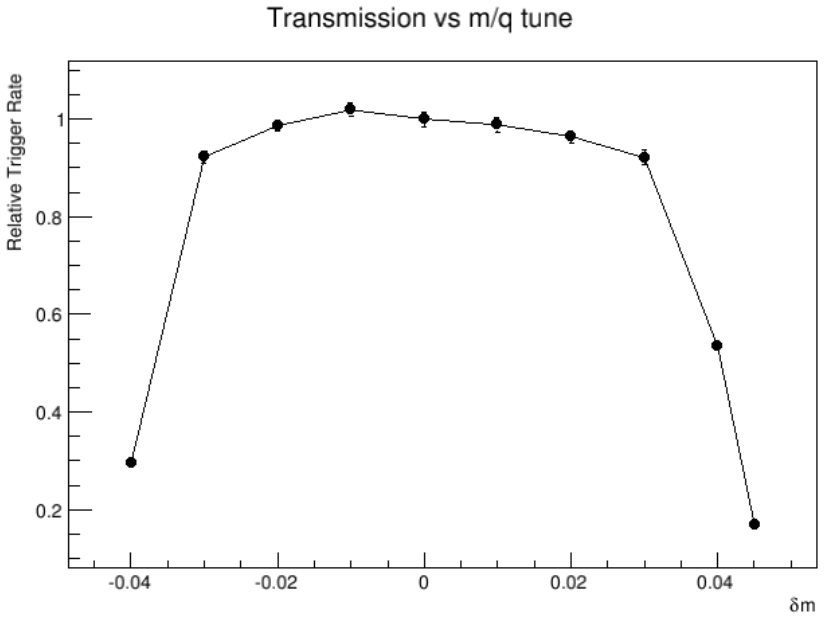

FIGURE 6.2: Transmission efficiency of α-particles vs m/q tune setting δm. The transmission efficiency is estimated using the count rate measured by the PGAC anode.

This can have the effect of smearing out the edges of the transmission efficiency close to the limits of the m/q acceptance, since some proportion of alpha particles that are still within the m/q acceptance will be instead lost due to their large azimuthal angle, with losses increasing as a function of the deviation from the central m/q tune.

6.1.2 Energy and angular acceptances

In addition to m/q, the transport efficiency through EMMA will change as a function of the energy deviation from the central tune, as well as the angle of the particles with respect to the optical axis. The transport efficiency as a function of energy and angle can be mapped out by using several entrance apertures, of various angular acceptances, and then measuring the transmission at several energy settings (E/q) with each aperture. The energy mis-tune δE is defined by Equation 6.2. A total of six apertures were used: full, centre, left, right, top and bottom. The dimensions of each of these apertures are listed in Table 6.1.

$$\delta E = \frac{(E/q) - (E/q)_0}{(E/q)_0} \tag{6.2}$$

Aperture	$\theta_{\min}$ [deg]	$\theta_{\max}$ [deg]	$\phi_{\min}$ [deg]	$\phi_{\max}$ [deg]	Solid Angle [msr]
Full	-3	+3	-3	+3	11.04
Centre	-1.2	+1.2	-1.2	+1.2	1.77
Left	-3	-0.6	-1.2	+1.2	1.77
Right	0.6	+3	-1.2	+1.2	1.77
Top	-1.2	+1.2	+0.6	+3	1.77
Bottom	-1.2	+1.2	-3	-0.6	1.77

TABLE 6.1: Aperture dimensions used during EMMA commissioning. The derivation of the solid angle subtended by a rectangular plate, for both the on-axis and off-axis cases, is set out in Ref [103]

The absolute transmission is calculated by dividing the number of alpha particles detected in the focal plane silicon detector by the expected number of counts; the latter is calculated based on the activity of the source, the solid angle of each aperture, and the duration of each run. The transmission efficiency as a function of energy/charge for each aperture is shown by Figure 6.3.

Comparing the data in Figure 6.3 with the GIOS predictions shows good agreement for at least the central and right apertures; however the others show noticeable disagreement in the transmission integrated over the entire energy distribution. The left aperture data shows reduced transmission when EMMA is tuned to energies lower than the alpha source, compared with expectation. However, much larger reductions in transmission appear to be found for the top and bottom aperture data, indicating that EMMA has a lower acceptance in vertical angle ϕ than expected. The losses in transmission as a function of ϕ likely explain much of the reduced transmission in the full aperture data compared with its respective GIOS predictions. The source of the reduced vertical

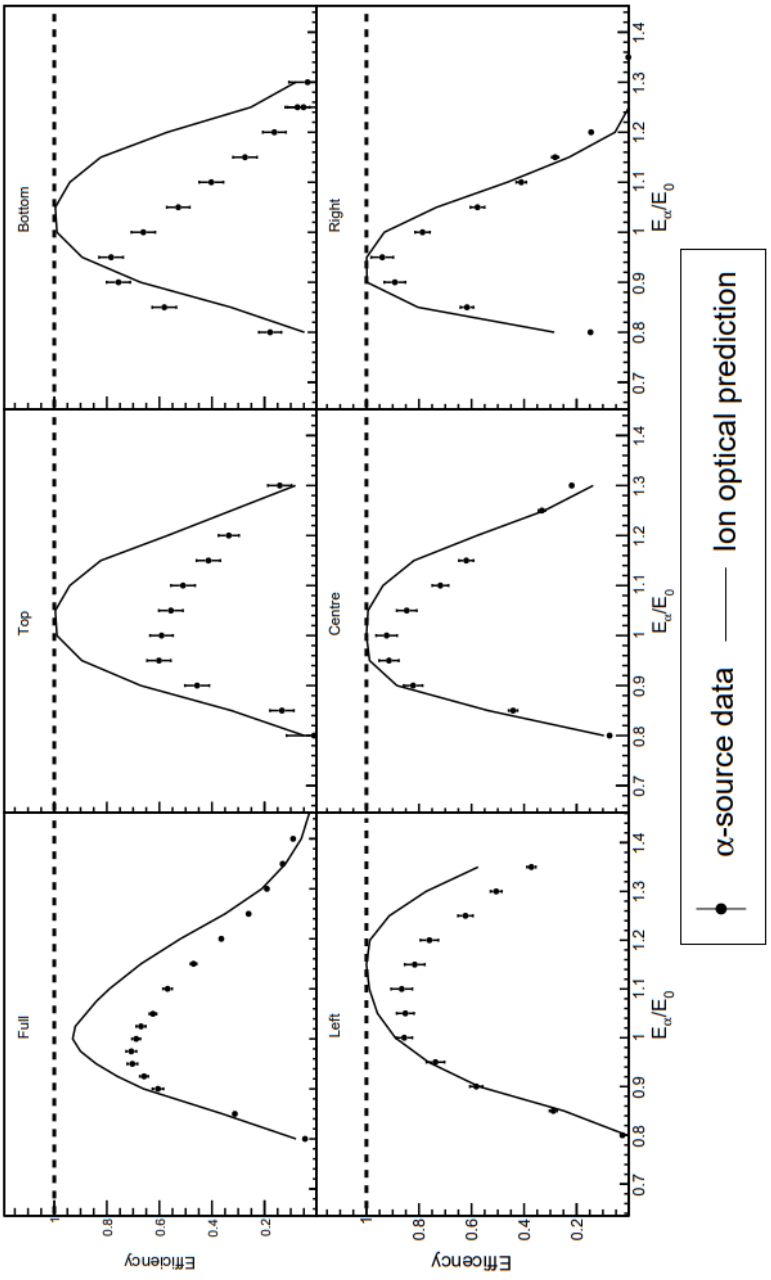

FIGURE 6.3: EMMA transport efficiency as a function of energy mis-tune for each of the apertures listed in Table 6.1. Note that the transmission has been corrected for the 94% transparency of the PGAC. The x-axis is the alpha source energy ($E_\alpha = 3.183$ MeV) divided by the tuned energy setting (E_0). The filled circles represent the real data, whereas the solid lines are the simulated transmission in GIOS.

angle (ϕ) acceptance is at present not fully understood and warrants further study. It is possible that there is some vertical restriction in the beam line (e.g. beam pipe entrance/exit flanges) that are not accounted for in the simulation. There was also some concern, noticed during final alignment of the EDs, that the ED1 support structure may have buckled inwards slightly during installation. More investigation via simulation is

required to conclude whether these possibilities could realistically explain the observed behaviour.

6.2 First in-beam test

The first in-beam test took place in December 2016, during which an 80 MeV ^{36}Ar beam was impinged onto a 4.46 μm gold foil. The goal of this initial test was to carry out a full diagnostic of the spectrometer control systems, detectors, and DAQ electronics. Encouragingly, without any prior testing with an alpha source, several beam charge states were transmitted to the focal plane. Figure 6.4 displays the PGAC position spectrum obtained when EMMA was tuned to accept both the 12^+ and 13^+ beam charge states. The horizontal separation of 81.5 mm between the two charge states is almost exactly in-line with the expected m/q dispersion of 10 mm / % discussed in Section 6.1.1.

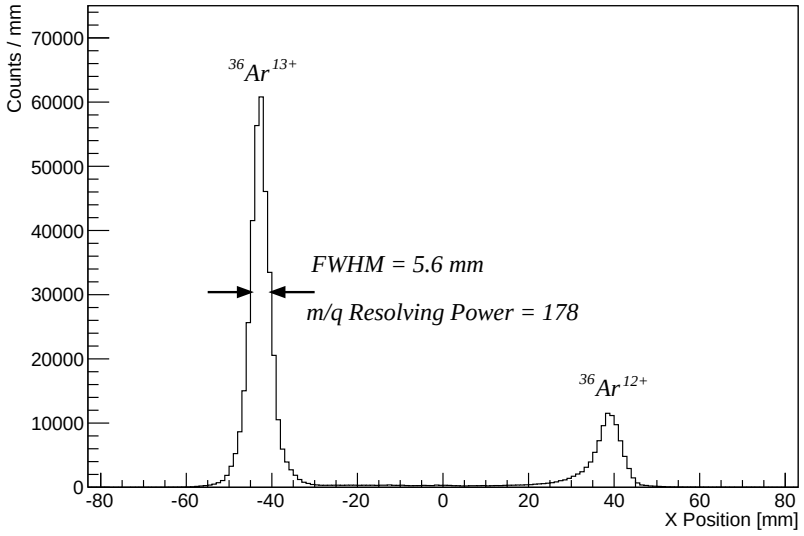

FIGURE 6.4: m/q spectrum taken during the first EMMA in-beam test. Two beam charge states are labelled, along with the FWHM and m/q resolving power calculated for the ^{36}Ar^{13+} peak.

The focal plane silicon detector energy spectrum, shown in Figure 6.5, indicates a relative energy spread of over 40% for the scattered beam ions. This suggests that close to the entire energy acceptance of EMMA is being filled. The predicted asymmetry of the energy acceptance is also qualitatively reflected in the energy distribution. Note that the detector resolution, of 55 keV FWHM for 5.486 MeV alpha particles, has a negligible effect on the total observed energy spread.

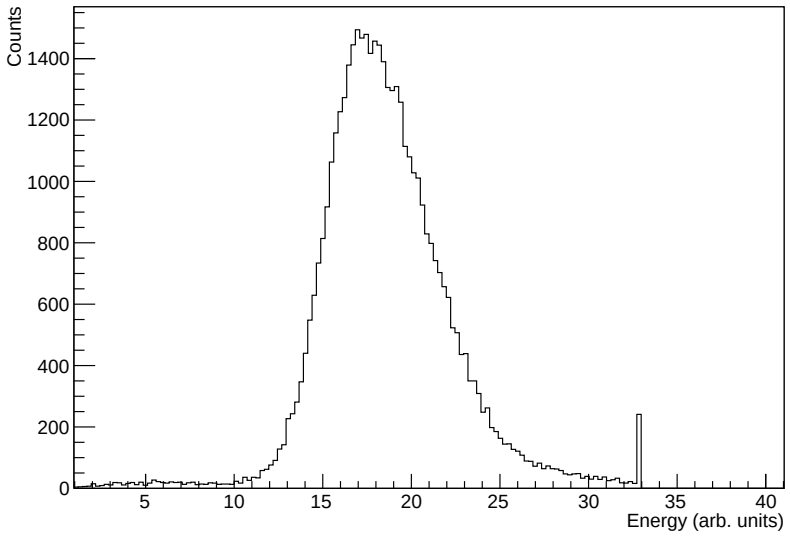

FIGURE 6.5: Focal plane silicon spectrum taken during the first EMMA in-beam test. Channel 33 contains overflow events. Note that the scattered beam energy, which EMMA was tuned to, was 18.8 MeV

Ion optical calculations performed in GIOS, assuming the observed energy spread, predicted angular distribution, and realistic assumptions of the beam spot size, predict an m/q resolving power $m/\Delta m = 175$ (FWHM = 5.7 mm). This compares favourably with the observed resolving power of $m/\Delta m = 178$ (FWHM = 5.6 mm). This resolving power is understandably less than the design first-order resolving power limit of $m/\Delta m = 550$, since the calculated resolving power quoted here includes the effects of chromatic and geometric aberrations. Improvements in the measured resolving power could be obtained by using a thinner target foil in order to reduce the energy and angular spread of the transmitted ions. For this reason, a much thinner 150 μg/cm^2 gold foil was utilized for the elastic scattering test discussed in Section 6.3.

6.3 Elastic scattering test

Further characterization of EMMA was not resumed until September 2017 in the form of another in-beam elastic scattering test, during which an 120 MeV ^{40}Ar beam was impinged onto a thin 150 μg/cm^2 ^{197}Au target. The purpose of this test was to map the angular, energy and mass acceptances using backscattered gold ions passing through various sized apertures, the dimensions of which are listed in Table 6.1.

6.3.1 Beam normalisation

In order to measure the absolute transmission efficiency one must be able to calculate the total integrated beam current over each data taking run. Before discussing the normalisation procedure however, it is first necessary to describe how the beam tune is optimized for delivery to EMMA. The EMMA target chamber contains its own Faraday cup that is co-planar with the target location, and can be manually rotated onto the beam axis during tuning. A tantalum plate with a 1 mm diameter aperture covers the Faraday cup, through which the beam must be tuned. Limiting the horizontal extent of the beam spot to 1 mm or less is highly important for EMMA experiments, since the resolving power will be degraded as a function of beam spot size due to magnification of the focal plane image. Simultaneous measurements of the current on both the cup and aperture help optimize the tune by minimizing the aperture current whilst maximising the cup current. After successful tuning, further periodic beam current measurements can be more conveniently taken with another Faraday cup located approximately 1 m upstream of the EMMA target chamber (in beam-line SEBT3B), instead of needing to repeatedly manually rotate the EMMA cup in and out of position.

In addition to an internal Faraday cup, the EMMA target chamber also contains elastic scattering monitors in the form of two silicon surface barrier (SSB) detectors held at 20° to the beam axis downstream of the target. These can be used to measure the beam current by the absolute yield from Rutherford scattering, or can be used in a fashion more similar to the DRAGON beam normalization procedure (Section 4.2.1), whereby the elastic scattering rate is measured relative to the absolute beam current through periodic Faraday cup measurements. The extremely high rate of scattered beam necessitated the placement of caps with 0.5 mm apertures in front of each SSB monitor in order to protect the detectors from damage. Since even a small discrepancy in the size and location of these apertures would result in large changes in the calculated yield from Rutherford scattering, it was decided that the more empirical approach to beam normalization should instead be taken. Though for completeness, the Rutherford scattering yield through one of the elastic scattering monitors for this experiment is calculated to be $6.4(1.4) \times 10^{-9}$ per incident beam ion. The 22% uncertainty comes from a ± 0.1 mm uncertainty in the aperture diameter, a $\pm 5\%$ uncertainty in the target thickness, and a ± 1mm discrepancy in the distance from the target.

The empirically measured elastic scattering yield per incident beam ion, the latter measured with the SEBT3B cup, is shown for each run on Figure 6.6 plotted against the ratio of counts measured in the left and right detector. While no clear correlation is

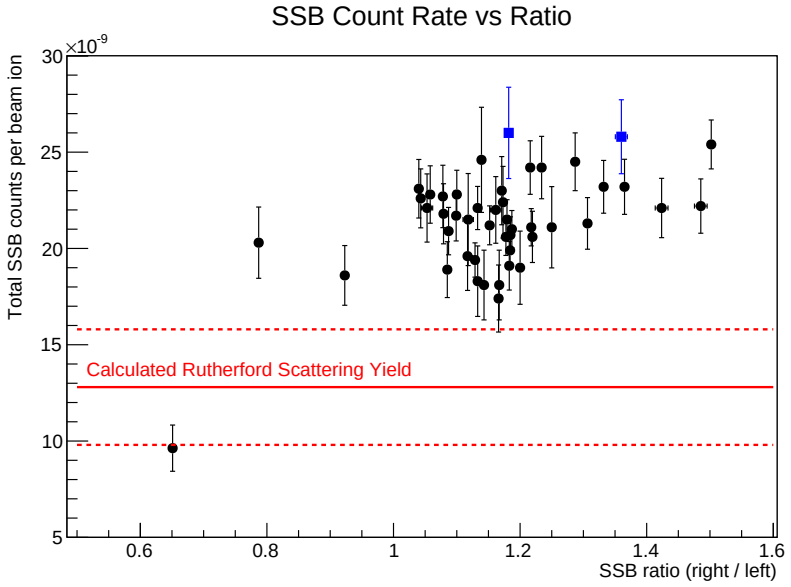

FIGURE 6.6: The total number of SSB counts per incident beam ion vs ratio of counts between the left and right SSB detectors vs; inferred from the beam current measured by the SEBT3B Faraday cup. The red solid line indicates the calculated Rutherford scattering yield, bound by its uncertainties indicated by the red dotted lines. The blue square data points were taken immediately after a beam tune optimization.

observed between the right/left ratio vs total scattering yield[1], there is significant overall spread in the total yield. The changing measured scattering yield strongly indicates that the SSB rate is highly dependent on the beam tune. Given that the apertures are smaller than the beam spot itself, and are thicker than they are wide, it is not in hindsight unexpected that this would be the case. If the SSB rate is indeed sensitive to minor changes in the beam tune, then it would be incorrect to simply average all the data points on Figure 6.6 to obtain the true scattering rate, since this is a changing systematic effect in the data.

The two points highlighted in blue on Figure 6.6 were taken from runs immediately proceeding a re-tuning exercise. These two runs appear to exhibit the largest measured scattering yield, which suggests that changes in the beam tune such as an off-centred beam spot result in a systematic reduction of the scattering yield. Therefore a value of $2.60(24) \times 10^{-8}$ is adopted as the SSB scattering yield assuming perfect transmission to the EMMA cup. The yield of backscattered gold ions passing through the EMMA entrance apertures listed in Table 6.1 must be calculated via Rutherford scattering however, which for the central aperture amounts to $8.5(5) \times 10^{-10}$ scattered gold ions per incident beam ion, and for the full aperture becomes $5.3(3) \times 10^{-9}$. The associated

[1]From the Rutherford scattering formula, a finite incident beam angle will produce an asymmetry between the left and right detectors. At small angles however, this will not significantly impact the total number of counts

uncertainty is smaller for this case since the relative uncertainty in the solid angle subtended by the EMMA apertures is much smaller than the SSB apertures. Combining these two ratios gives the expected number of gold ions passing through the aperture per count measured in the SSB detectors, which is calculated as 0.033(4) for the central aperture and 0.20(2) for the full aperture[1]. These ratios enable the absolute yield to be calculated independently of fluctuations in beam current.

6.3.2 Identifying ^{197}Au ions and background subtraction

The transmitted gold ions are focussed into clearly identifiable peaks in the focal plane position spectra. However, as is shown by the 'no cuts' spectrum in Figure 6.7, there is clearly a significant beam induced background. Much of this background can be removed by imposing an energy cut on events in the high energy peak of the focal plane silicon detector energy spectrum shown in Figure 6.9. The effectiveness of this energy cut is demonstrated by Figure 6.7. However, this cut loses efficiency at large displacement from the centre of the focal plane, due to the smaller active area of silicon detector compared to the PGAC. This poses a problem when measuring transmission efficiency as a function of δm, since the peak of interest is displaced across the focal plane and outside the active area of the silicon.

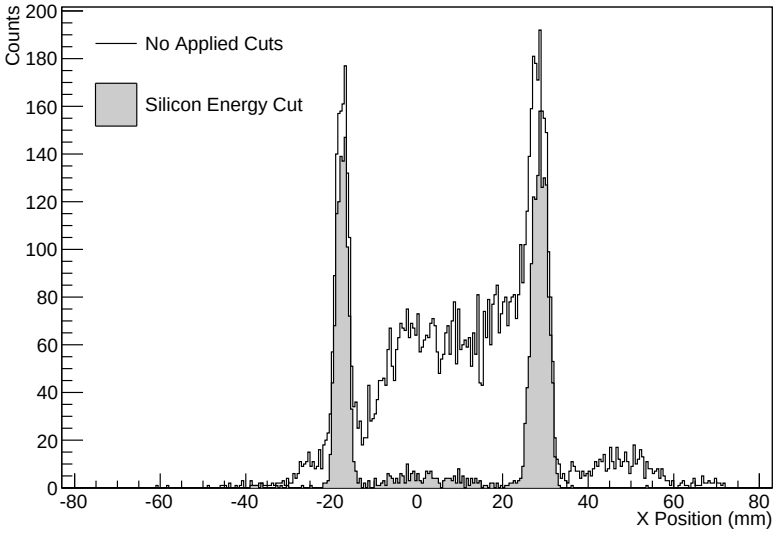

FIGURE 6.7: X-position spectrum with cuts that discriminate gold recoils from scattered beam.

[1]The off-axis apertures were not utilized for this test. However, their associated scattering yield ratio is effectively the same as for the central aperture due to their very similar solid angle coverage, and the relatively constant Rutherford differential cross section at backward angles.

The mass mis-tune data sets therefore require an alternative approach for handling the background. Figure 6.8 shows a 2D position spectrum of $q = 22$ gold ions centred at the focal plane. The background due to scattered beam is not uniform with respect to horizontal distance along the focal plane, but appears de-focussed and uniform with respect to vertical position in the vicinity of the recoil focus. The signal region containing the $q = 22^{+}$ gold ions is highlighted with a green bounding box. The background within the signal region can be estimated by sampling above and below the signal region. The background-subtracted signal with associated statistical errors is then extracted using the Rolke method assuming a Poisson background model [92].

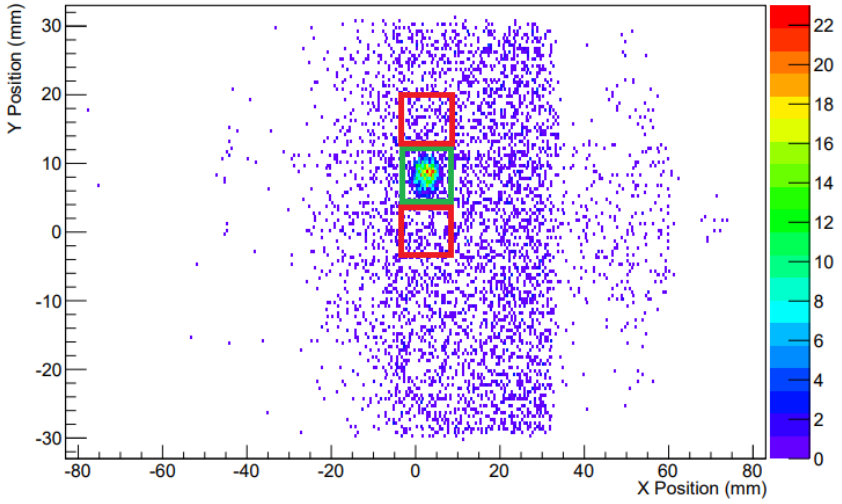

FIGURE 6.8: 2D focal plane position spectrum showing gold recoils focused in the middle of the focal plane in the midst of a scattered beam background. The signal region is highlighted with a green bounding box. The background within this region was estimated by sampling above and bellow the recoil focus (highlighted with the red bounding boxes), and using an average of the two samples. Note the +8 mm vertical misalignment of the focal plane image; see text for discussion of possible explanations.

An interesting feature exhibited in the 2D focal plane spectra, as shown in Figure 6.8, is an apparent vertical offset in the focal plane image. This off-set of approximately +8 mm is thus far not understood and requires further investigation. A simple explanation could be related to a mechanical alignment of the PGAC itself with respect to the focal plane. This should first be ruled out before investigating more complicated ion optical explanations, such as imperfect alignment of the electrostatic dipoles, that could be related to losses in acceptance in the non-dispersive direction, as noted in the alpha particle tests.

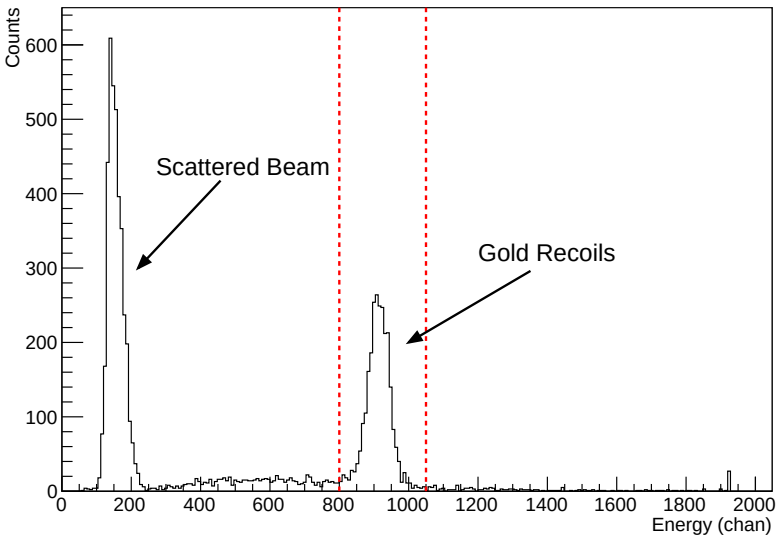

FIGURE 6.9: Focal plane silicon detector energy spectrum of ions reaching the EMMA focal plane. The scattered Ar beam and gold peaks are labelled. A cut can be placed on the gold peak to remove much of the scattered beam background. The effectiveness of this cut can be seen in Figure 6.7.

6.3.3 Charge State Distribution

A key component of absolute normalization is to measure the charge state distribution of gold recoils. The spectrometer was therefore set to transmit several charge states from 20^+ to 27^+. Using the previously discussed ratio of 0.033(4) gold ions per SSB count for the central aperture, the absolute charge state fraction can be plotted for each charge state. The resulting charge state distribution shown in Figure 6.10 was fit with a Gaussian. The total transmission efficiency can then be estimated by integrating the Gaussian distribution over all charge states, which amounts to $(99.7 \pm 4.2)\%$. This includes corrections for the transparency of the PGAC wire grids (see Table 3.2), and the finite DAQ live-time[1].

6.3.4 Results and discussion

The absolute transmission efficiency as a function of δm and δE was measured for both the full and central apertures. Unfortunately there was insufficient time to complete measurements with the off-axis apertures. Plots displaying the transmission vs δm and δE for each aperture are shown in Figures 6.11 and 6.12 respectively.

[1]The DAQ live-time for each run was estimated by dividing the number of accepted triggers by presented triggers as recorded by a scaler module. This typically gives a relatively small correction of $0 - 2\%$.

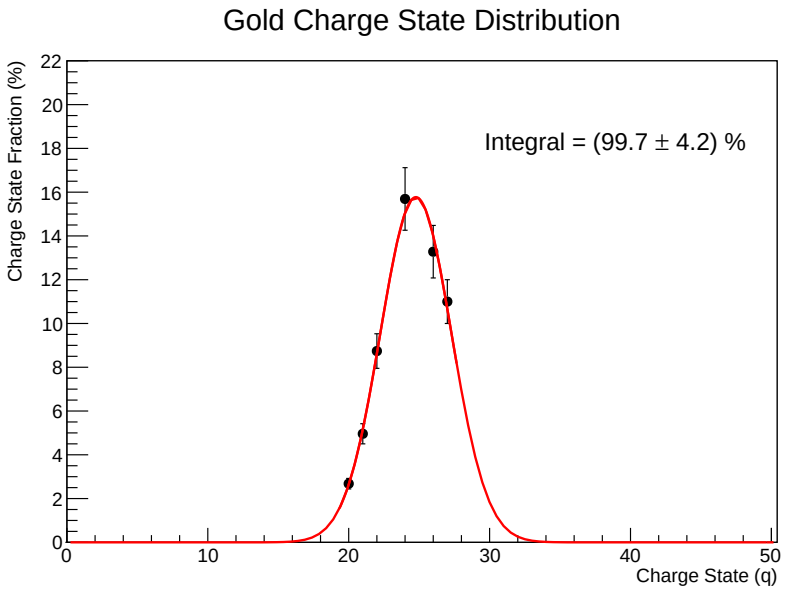

FIGURE 6.10: Charge state distribution of elastically scattered gold ions. The distribution was fit with a Gaussian, for which the integral over all charge states amounts to $(99.7 \pm 4.2)\%$. The data include corrections for the 94% transparency of the the PGAC wire grids and a small correction for the DAQ live-time.

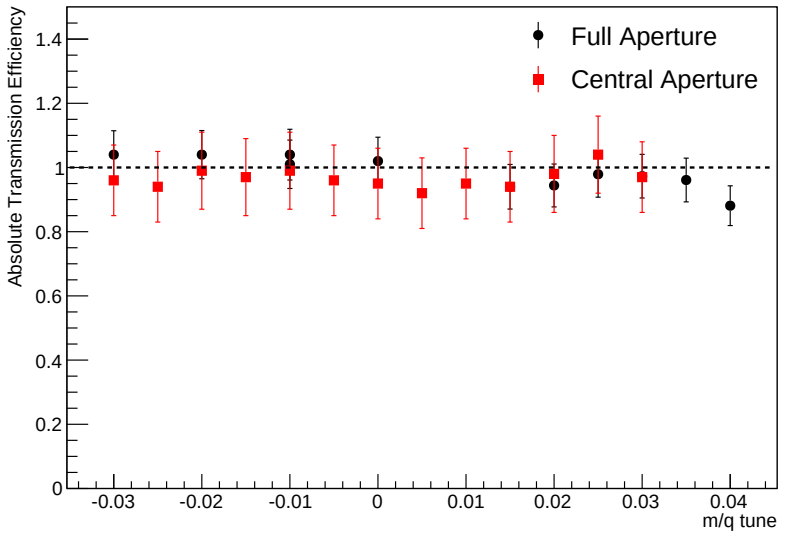

FIGURE 6.11: Transmission efficiency vs δm for the elastically backscattered gold measurements taken with the full (black circles) and central (red squares) apertures.

The transmission for both the full and central apertures, as a function of δm, appears to be uniform over the range studied and consistent with 100% transmission efficiency, albeit within a significant error margin on each data point of $10-15\%$. The typical error budget associated with the data points include a 3% statistical error and 11% point-to-point systematic error. The systematic error derives from the 0.033(4) transmitted gold ion per SSB count, which reflects the sensitivity of the SSB normalization procedure

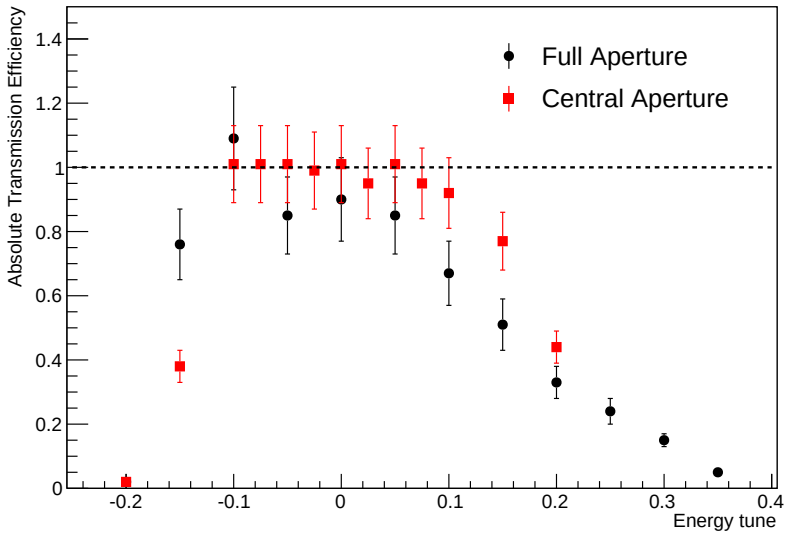

FIGURE 6.12: Transmission efficiency vs δE for the elastically backscattered gold measurements taken with the full (black circles) and central (red squares) apertures.

to beam tune variations. The global systematic error, associated with the charge state fraction of 22^+ gold ions $(8.74 \pm 0.79)\%$, is not included in any of the transmission plots, since this particular uncertainty affects all points simultaneously.

The observed m/q transmission is consistent with the expectation that it should be uniform over the acceptance range of $\pm 4\%$. Further determination of the transmission efficiency from this experiment is somewhat limited, partly by the large systematic uncertainty associated with the beam normalization, but primarily due to the absence of any data taken with the off-axis apertures.

In addition to measuring the transmission, the mean X-positions were also recorded as a function of δE. Plotting the mean X-position vs δE, as is shown in Figure 6.13, reveals that the energy dispersion cancellation was not perfect. Indeed, investigating this issue was the primary motivation for the optimization exercises in Section 6.5.

Significant geometric aberrations were observed to be present by comparing the focal plane position spectra taken with the central and full apertures. At nominal tune settings, the resolution degrades significantly with the full aperture in place compared with the central, as is demonstrated in Figure 6.14. Efforts to improve the resolving power were subsequently investigated by varying the quadrupole field strengths, the results of which are detailed in sub-section 6.5.2.

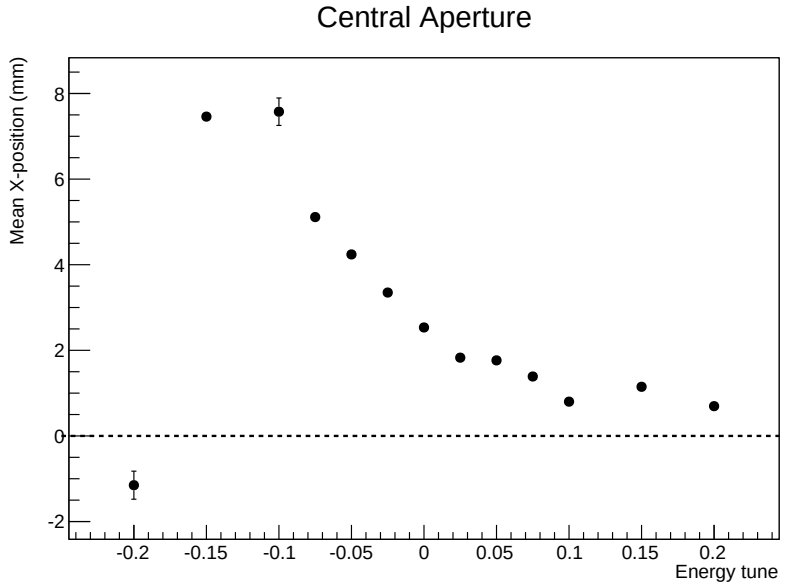

FIGURE 6.13: Mean x-position vs δE.

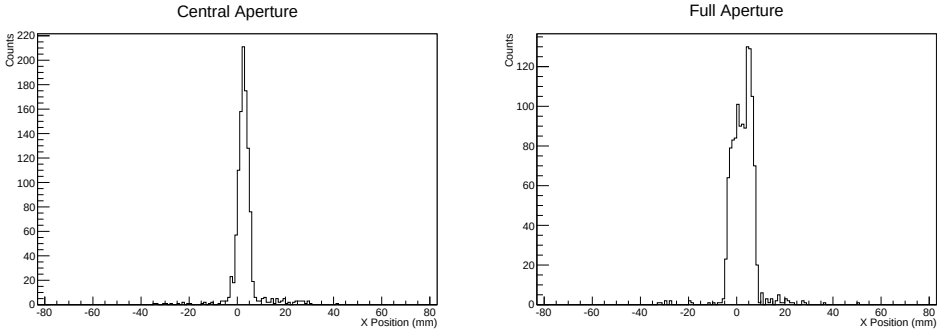

(A) (B)

FIGURE 6.14: X-position spectra taken with the central and full apertures at nominal tune settings, i.e., no mass or energy mis-tune. Significant aberrations are evident in the full aperture data. The observed FWHM resolving power for the central aperture is calculated as $m/\mathrm{d}m = 220$ (4.54 mm). This is less than the predicted resolving power for this experiment of $m/\mathrm{d}m = 330$. The large aberrations noted in the full aperture study result in a FWHM resolving power of $m/\mathrm{d}m = 90$ (11.12 mm). The incident ^{40}Ar beam energy was 120 MeV, the backscattered ^{197}Au ($q = 23^{+}$) recoils emerge from the 150 μg/cm^2 target with a central energy of 66 MeV.

6.4 Fusion evaporation test

The design of EMMA was optimized for the study of both fusion evaporation reactions and single particle transfer in inverse kinematics. Fusion evaporation products emerge from the target with relatively broad angular and energy distributions, which depend on the ratio of masses between the beam and recoil, the compound nucleus excitation energy, and the number of light particles evaporated. Fusion evaporation studies therefore require large acceptances in both angle and energy, while not compromising the

m/q resolution required to identify the heavy ion products. The performance of EMMA for fusion evaporation studies was assessed during an in-beam test, which took place in November 2017.

The brief (four day) test run used stable and radioactive ^{23}Na and ^{24}Na beams incident on a 1 μm thick ^{nat}Cu target. Spectrometer settings were explored for the $A = 79 - 84$ mass range, with charge states of $q = 9^+ - 11^+$, and central energy settings of between 15.6 and 18.4 MeV. The fusion evaporation code PACE4 was used to predict optimal settings prior to the run [104]. Figure 6.15 shows m/q spectra for both a stable and a radioactive beam run. Similar performance is seen for both the stable and radioactive beam runs, with several clearly identifiable m/q peaks. Suppression of the un-reacted beam was optimal during this test, with no (or negligible) scattered beam background apparent in the focal plane m/q spectra. The beam suppression factor is defined as the number of incident beam ions divided by the number of transmitted beam ions. For the stable ^{23}Na run, shown in Figure 6.15, the total number of incident beam ions on target was approximately 2×10^{12}. This implies a beam suppression ratio in at least the 10^{12} range for this example.

The fewer counts obtained by requiring a hit on the silicon detector is mostly due to the smaller area coverage compared to the PGAC. This is particularly noticeable for the $A = 76$ peak in the top panel of Figure 6.15; while recoils with this mass are still within the acceptance of EMMA, most do not impact the silicon detector. Many incident recoils also lie outside the vertical coverage of the silicon detector; the 2D focal plane spectrum for a stable beam run is shown on Figure 6.16. The previously observed vertical offset of +8 mm is also apparent from Figure 6.16. The excess of counts beyond -60 mm seen in the lower panel of Figure 6.15 is due to a small line-of-slight exposure to an alpha source in the focal plane vacuum box, which was not removed ahead of this test, though its presence is only noticeable over long periods of data taking.

This test demonstrates that EMMA is capable of selecting fusion evaporation residues produced from radioactive ion beams. By coupling EMMA to the TIGRESS HPGe array, experiments to produce and study more exotic radioisotopes will now become feasible at ISAC through greatly increased selectivity of weakly populated reaction channels.

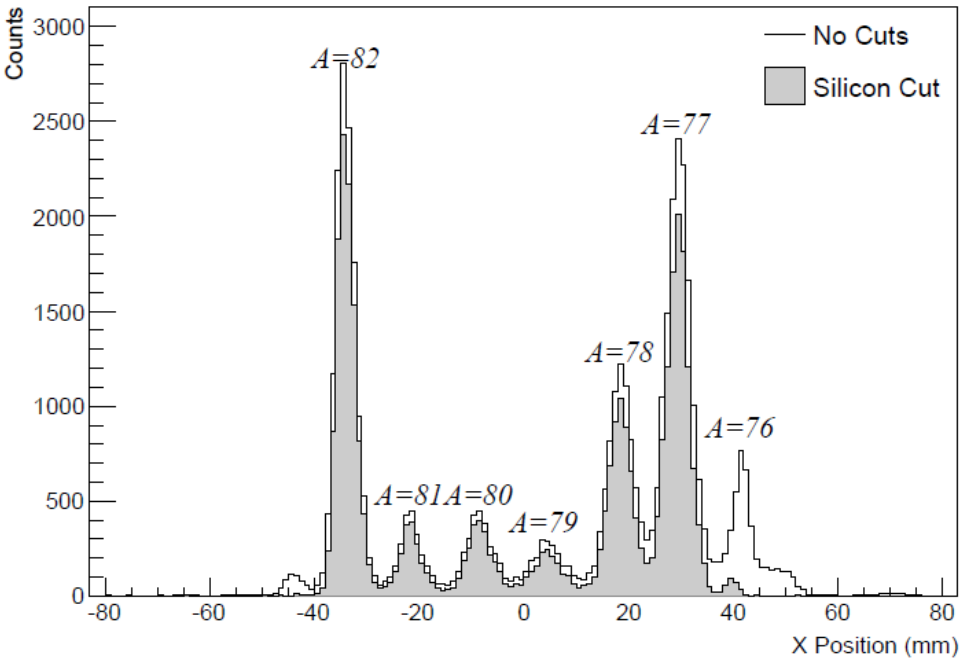

(A) Stable ^{23}Na beam run

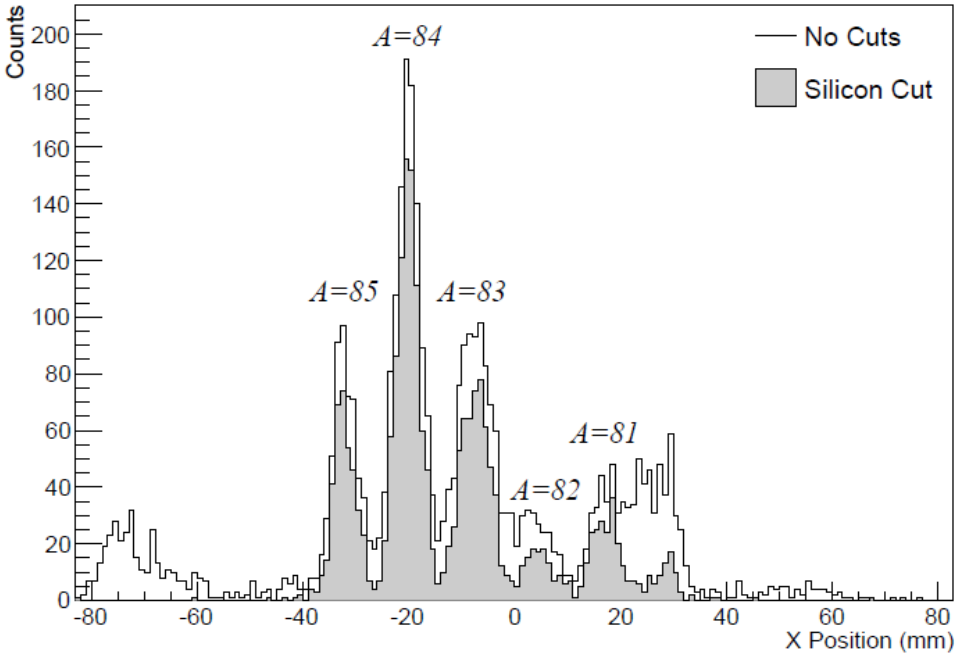

(B) Radioactive ^{24}Na beam run

FIGURE 6.15: Comparison between focal plane position spectra for fusion evaporation residues produced from stable ^{23}Na (top) and radioactive ^{24}Na (bottom) reacting on a ^{nat}Cu target. The shaded histogram indicates events which also hit the silicon detector downstream of the PGAC. The maximum resolving power achieved in this test was $m/\mathrm{d}m = 238$ (4.2 mm FWHM), which pertains to the A=82 peak shown in the stable ^{23}Na beam run (A).

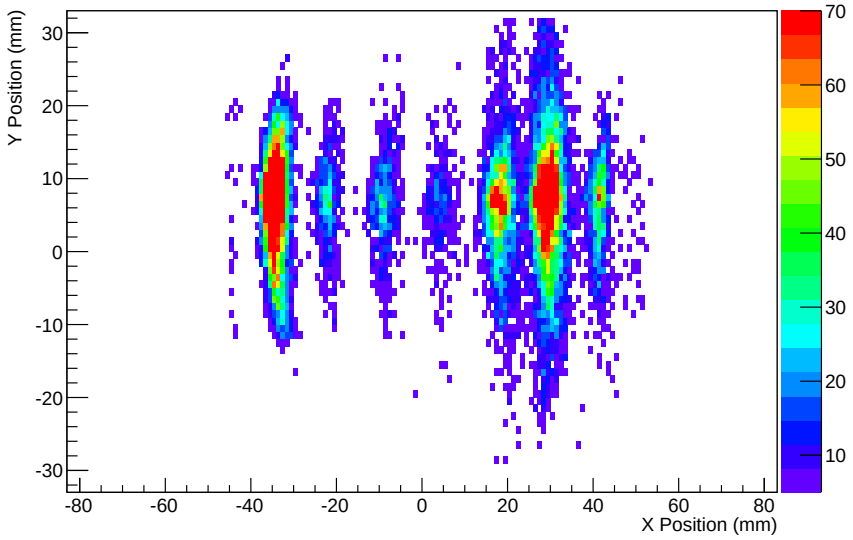

FIGURE 6.16: Focal plane 2D-position spectrum of fusion evaporation residues from ^{23}Na + ^{nat}Cu. Note the persistent +8 mm offset in the vertical direction, which was discussed in Section 6.3.2. The masses of the detected recoils are the same as those indicated on Figure 6.15(A).

6.5 Optimizing the Ion Optics

6.5.1 Re-positioning the Dipole Magnet

During the course of initial testing, and most notably during the September in-beam commissioning, several adverse features in the spectrometer's performance were noted. Of particular concern was the sub-optimal energy dispersion cancellation at the focal plane. The energy dispersion cancellation depends on the relative strengths of, lengths of, and spacing between the dipole field elements. The location of each field element along the optical axis is based on the spacing between their effective field boundaries. However, the ion trajectories will of course be bent by some amount within the fringe fields before reaching the effective field boundary[1]. The fringe fields of the EMMA dipole magnet in GIOS are described by a standard set of Enge function coefficients based on the geometry of the magnet. Comparison between the theoretical field profile and the measured field map of the dipole revealed that the GIOS Enge function coefficients should be adjusted to more accurately describe the true field. After adjusting the field parameters, it was found theoretically that the MD position should be moved 14 mm in the direction pointing away from the centre of the radius of curvature (Westwards in the experimental hall co-ordinates).

[1] A complete description of the effects of fringing fields on charged particle trajectories is beyond the scope of this thesis, but can be readily found in Ref [45]

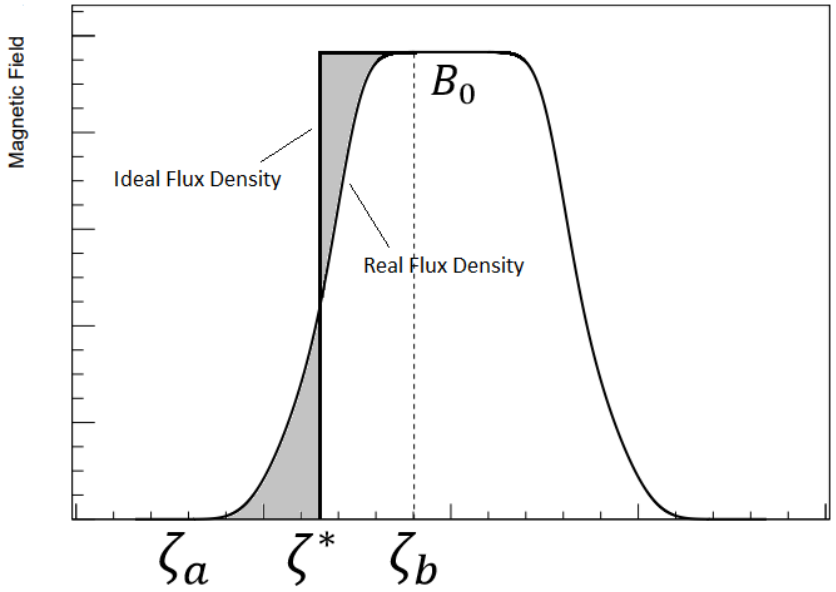

FIGURE 6.17: Diagram of fringe fields and effective field boundaries in a dipole magnet. ζ_a is located at the start of the fringe field region, ζ_b marks the beginning of the uniform field region, and ζ^* is the effective field boundary. The gray shaded areas between the real and ideal flux densities cancel.

The energy dispersion cancellation was measured after moving the dipole to a series distances from its nominal locations. The structure upon which the dipole is situated was specially designed to allow for such adjustments. Once the dipole had been aligned to a new location, by use of precision laser tracker measurements, the mean focal plane position of transmitted alpha particles was measured for several energy mis-tunes. An optimum location of +12 from the nominal location was empirically determined.

6.5.2 Quadrupole tune optimization

The quadrupole settings were also explored in order to see if the resolving power could be further improved. These studies were somewhat limited in scope since the parameter space for modifying the settings of all four quads is very large. Initially, just the first two quadrupole magnets were used to obtain a focus before moving on to exploring settings with all four quads in operation. Figures 6.18 and 6.19 show the FWHM and transmission efficiency respectively for varied Q1 and Q2 field strength ratios. These studies show that better resolving power can be obtained for a greater Q2/Q1 field ratio, but the transmission is reduced as a result. Since no simultaneous maxima were observed for the resolving power and transmission; this study was taken to indicate that nominal tune settings for the first two quads offer the best compromise. Tunes with varied Q3 and Q4 field strengths were not exhaustively explored, however since no

significant improvements could be observed for the first two quads it is not expected that studies of Q3 and Q4 would yield much improvement either.

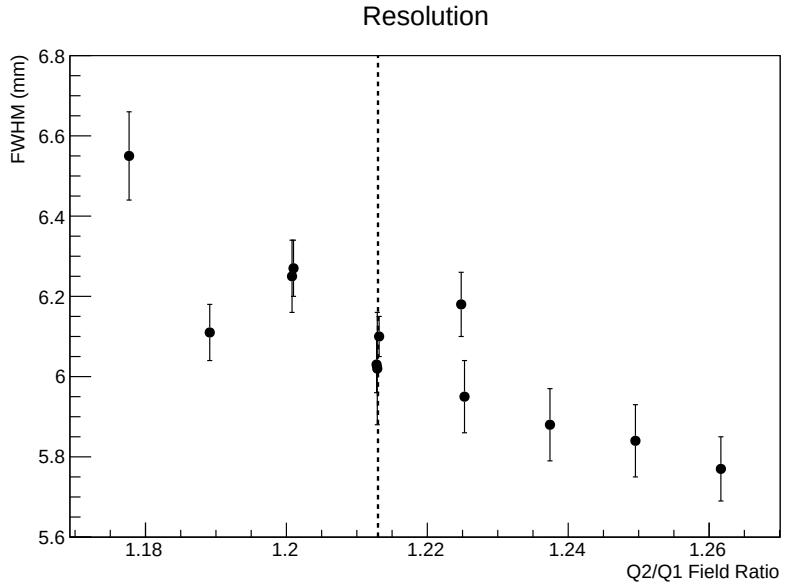

FIGURE 6.18: Plot showing the effect of varying Q1 and Q2 field strength on resolving power (inversely proportional to the horizontal extent of the image) at the focal plane. The dashed line indicates the nominal Q2/Q1 field ratio.

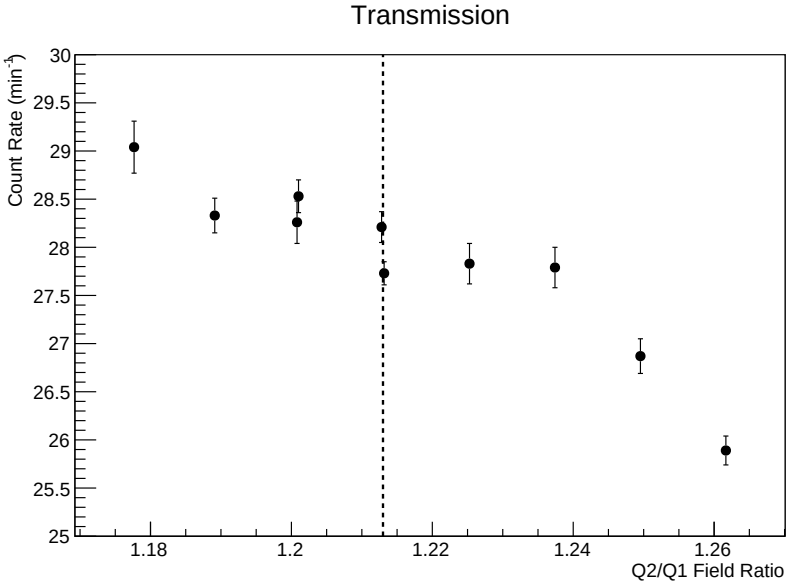

FIGURE 6.19: Plot showing the effect of varying Q1 and Q2 field strength on transmission efficiency (proportionate to count rate) at the focal plane. The dashed line indicates the nominal Q2/Q1 field ratio.

6.5.3 Slit transmission studies

During the initial alpha source testing and in-beam testing it was noticed that the maximum transmission was not located at the nominal energy ($\delta E = 0$). This is unexpected for the central and full apertures, and perhaps indicative that the ions are not exiting the electrostatic deflectors on-axis. The distribution of alphas exiting ED1 and the MD can be coarsely measured by asymmetrically closing the pairs of slits located immediately upstream and downstream of the MD. i.e. one can measure the transmission with the slits open more on the left side than on the right, and vice versa. The measured focal plane event rate obtained with the left side open vs the right can then be compared with the predicted ratio from GIOS to ascertain whether the alphas are being over or under steered by the dipole elements. The procedure was performed twice, first investigating ED1 using the pair of slits before the MD (`xslit20`), and then with the MD using the slits immediately downstream of the MD (`xslit21`). The distribution of alphas after the second ED is of course directly measured by the PGAC at the focal plane.

The positions of the slit plates were set such that the total gap between the left and right plates is kept constant at 120 mm, but the centre point between the plates is offset by 30 mm either to the left or the right. i.e. for the 'left side open' measurements the left plate edge is moved to +90 mm from the centre, and the right plate edge is moved -30 mm[1]. The other slit, which is not being used to perform the measurement, must be fully opened so as not to impact the results. With the aforementioned slit locations for `xslit20` (before the MD), GIOS calculations show that the count rate when the centre of the opening is to the left of the optic axis is 2.5% larger compared with the right side. The measured count rate vs ED1 voltage scale factors is shown in Figure 6.20. The polynomial fit to the data suggests that an increase in the ED1 field strength by 1.9% with respect to the nominal value produces the best match to the centred alpha distribution according to GIOS. The same plot but instead optimising through the MD using `xslit21` (downstream of the MD) shows that a 1.3% increase in the MD field is most appropriate. A 3% increase in the ED2 field is then needed to recentre the alphas at the focal plane.

After the completion of this tuning exercise, the latest data for energy mis-tune studies covered in Section 6.1.2 show that the maximum transmission is now at or very close to the nominal tune for the full and centre apertures. The field scale factors for each dipole element can now be changed within the ion optics controls page, and are taken into account when scaling all fields to the desired ion mass, kinetic energy and charge state.

[1]Positive slit locations in the EMMA controls pages are defined as 'beam-left', negative are 'beam-right'.

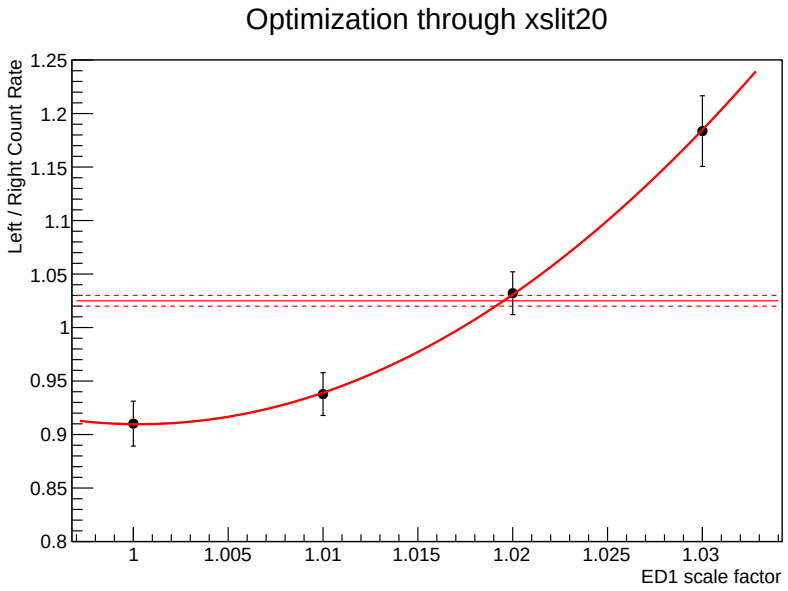

FIGURE 6.20: Optimisation of the ED1 voltage scale factor for tuning through `xslit20`. The solid red line indicates the predicted ratio from GIOS, with the dotted line representing the statistical errors in the simulation. A second order polynomial gives the best fit, which intersects the GIOS prediction when the ED1 field is scaled upwards by 1.9% from the nominal field strength.

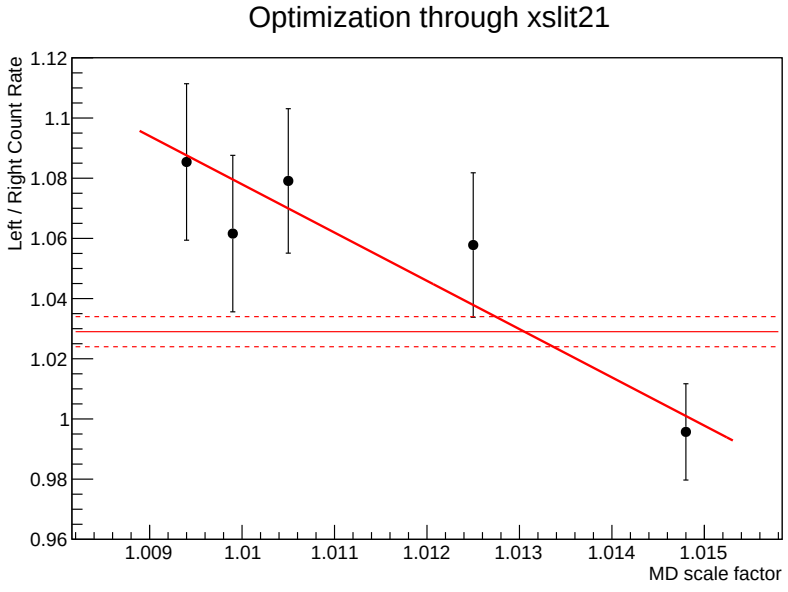

FIGURE 6.21: Optimisation of the MD field scale factor for tuning through `xslit21`. The solid red line indicates the predicted ratio from GIOS, with the dotted line representing the statistical errors in the simulation. A first order polynomial gives the best fit, which intersects the GIOS prediction when the MD field is scaled upwards by 1.3% from the nominal field strength.

Chapter 7

Conclusions

This thesis presents results obtained from the first inverse kinematics study of the $^{22}\mathrm{Ne}(p,\gamma)^{23}\mathrm{Na}$ reaction, which was performed using the DRAGON facility at TRIUMF. A total of six resonances were targeted in this study, including three recently identified low energy resonances at $E_{c.m.} = 149, 181$ and 248 keV, as well as the important reference resonance at $E_{c.m.} = 458$ keV. This is the first time that the 458 keV resonance has been measured in an absolute fashion that is totally independent of other resonances. A strength value of 0.467(14) eV was obtained for this resonance, which is significantly lower than the values reported in two recently published studies [72, 73]. In the case of the 632 keV resonance, the current result is higher than the recently reported value by Depalo *et al.* [73] by more than an order of magnitude, and a factor of two higher than the previous value by Meyer *et al.*[64]. The aforementioned result by Meyer *et al.* is however brought into 2σ agreement with the present value after renormalizing their relative strength to the 610 keV resonance strength reported in this work.

The yield measurements for the three low energy resonances were hindered by the lack of working MCP detectors to cleanly identify ^{23}Na recoils from scattered beam via time-of-flight. Nonetheless, measurements of the 181 and 248 keV resonance strengths were obtained which are in agreement with those published by the LUNA collaboration [83]. Unfortunately no clean recoil signal could be observed for the 149 keV resonance due to the aforementioned issues with the MCP time-of-flight detection system. The strengths of the 149 and 181 keV resonances put forward by the LENA collaboration [79] were measured relative to the 458 keV resonance strength reported in Ref [72], and are outside of 1σ agreement with the LUNA results [83]. However, renormalizing the low energy LENA resonance strengths to the present strength for the 458 keV resonance brings both results into much closer agreement with the LUNA values. A proposal put forward by the author to re-measure the 149 and 181 keV resonances, now that new MCPs have

been installed and tested, has been accepted by the TRIUMF experiment evaluation committee and will be scheduled at the earliest opportunity.

The direct capture contribution to the ^{22}Ne$(p,\gamma)^{23}$Na reaction was also measured in the energy range of $282 \leqslant E_{c.m.} \leqslant 511$ keV, from which an astrophysical S-factor of $S(0)_{eff} = 61.1 \pm 2.2$ keV $\cdot$ b was obtained. This is in good agreement with prior determinations of the non-resonant S-factor [75, 76], though substantially reduces the associated uncertainty. A new thermonuclear reaction rate was calculated based on this work, for which a factor of ~ 4 enhancement at 100 MK is seen over the previously assumed rate [86].

The impact of the new ^{22}Ne$(p,\gamma)^{23}$Na rate was then assessed for nucleosynthesis in both classical novae and AGB stars. In the case of the Carbon-Oxygen nova models an enhancement of a factor of ~ 2 is seen for the ^{23}Na ejecta content, with small changes in the ejected mass fractions of other elements between Ne and Al. For the Oxygen-Neon novaa models the ^{22}Ne is even more efficiently destroyed during the outburst, resulting in nearly a factor of 2 reduction in the ^{22}Ne ejecta content, while leaving other isotopes effectively unchanged. This result offers further constraints on the ^{20}Ne/^{22}Ne ratio expected from ONe novae, which is of interest for identifying and categorizing pre-solar grains of classical nova origin.

Post-processing nucleosythesis calculations performed for both intermediate mass and low mass AGB stars show that the present rate has minimal impact on the surface ^{23}Na abundances with respect to the previous rate. This is in contrast with calculations performed using the LUNA rate, which includes upper limits for the 68 keV and 100 keV resonances, showing a factor 3 enhancement in the surface ^{23}Na content for a $5M_{\odot}$ AGB star [102]. This suggests that the tentative 68 and 100 keV resonances dominate the uncertainty in the ^{22}Ne$(p,\gamma)^{23}$Na reaction rate at temperatures relevant for hot bottom burning in intermediate mass AGB stars. Direct measurement of the 100 keV resonance may be possible at the DRAGON facility, which potentially could reduce the LUNA upper limit by a factor of 10 if no yield is observed and beam suppression is favourable. However, improving the current upper limit for the 68 keV resonance is not feasible with DRAGON due to the lower cross section and recoil transmission efficiency.

The second goal of this thesis was to present the successful commissioning of a new recoil spectrometer at the ISAC facility: the Electromagnetic Mass Analyser (EMMA). The performance of EMMA was assessed in a series of in-beam and alpha source test studies. The m/q acceptance and dispersion match very well compared to design expectations. However, initial testing revealed issues relating to the energy dispersion cancellation and resolving power. The energy dispersion cancellation was vastly improved by re-positioning the magnetic dipole (MD) as well as adjusting the field strength settings

for the MD and electric dipoles (EDs). Varying the field strengths of the quadrupole magnets did not yield appreciable improvements in the resolving power.

The transport efficiencies of EMMA were subsequently mapped as a function of energy and angle using a ^{148}Gd alpha source. The results of these tests compare favourably with ion optical calculations for the transport efficiency as a function of energy and horizontal angle (θ). On the other hand, the vertical angular acceptance (ϕ) appears to be significantly reduced with respect to expectations by approximately a factor of two at the central energy tune. The source of this discrepancy is not yet known at this stage and requires further investigation. Nonetheless, the obtained results can still be used to estimate transport efficiencies for future EMMA experiments.

Lastly, the suitability of EMMA for fusion evaporation studies was successfully demonstrated in a brief test experiment, whereby EMMA was set to transmit the heavy ion residues produced from fusion evaporation of sodium beams on a natural Cu target. Well resolved mass spectra were produced for recoils in the $A = 76 - 85$ mass range, despite the large energy spread of products emerging from the target. Rejection of the un-reacted beam was also optimal during this test, with no (or negligible) scattered beam background observed at the focal plane.

Further tests are scheduled with a view towards demonstrating EMMA's applicability for radiative capture and single nucleon transfer studies. These tests are likely to present a greater challenge for beam suppression than fusion evaporation, due to the relatively smaller difference in A/q and E/q between beam and recoils. Moreover, the design of EMMA is optimised for acceptance of reaction products, rather than beam rejection. This is in contrast to DRAGON, which is specifically designed to have the beam rejection capabilities required to measure low yield radiative capture reactions at energies relevant for astrophysical processes.

To summarise, the results presented here represent important and necessary first steps towards successfully implementing EMMA into the experimental nuclear physics program at ISAC, to which the author has been privileged to contribute.

Appendix A

Calibration of the EMMA Quadrupole Magnets

Quadrupole magnets focus beams of charged particles transversely with respect to the direction of travel. The focussing direction is dependent upon the orientation of the magnet and direction of the electrical current. Figure A.1 shows the example of a y-focussing quadrupole field for a positively charged particle moving into the page. Note that the field is also dispersive in the x-direction. Therefore at least two quadrupole magnets are required to work in conjunction for both vertical and horizontal focusing to be achieved.

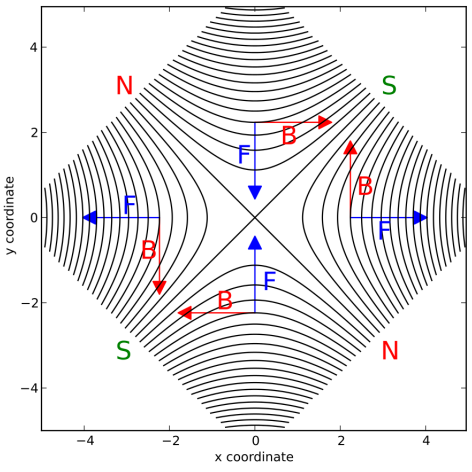

FIGURE A.1: Diagram of an idealized quadrupole field showing the direction of the Lorentz force for a positively charged particle moving into the page.

Recoil mass spectrometers such as EMMA focus charged particles onto detectors positioned at the focal plane. The dispersion across the focal plane is dependent on their

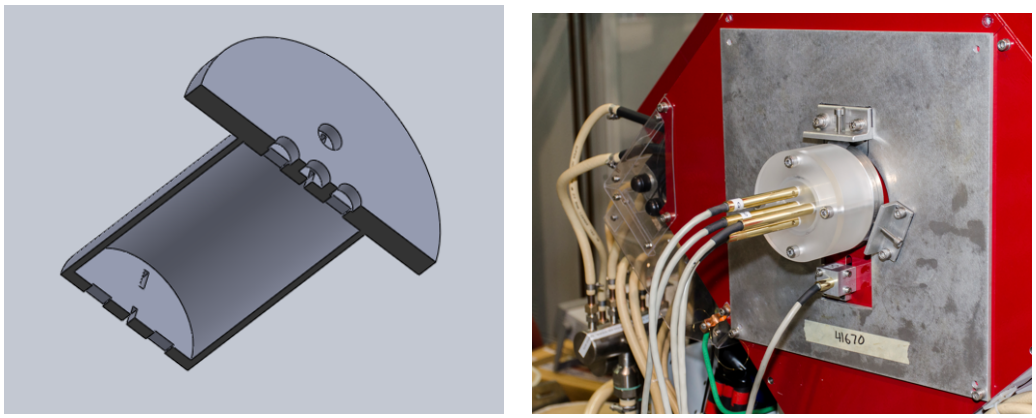

(A) (B)

FIGURE A.2: A) Cross-sectional view of the Q1 field measurement jig drawn in SolidWorks. B) Image of the Q1 measurement set up.

mass-to-charge (m/q) ratios. EMMA's quadrupole magnets play an important role in determining the (m/q) dispersion, as well as the (m/q) resolving power. Therefore very precise control and knowledge of the quadrupole field gradients is required for optimal operation of the spectrometer. This appendix details efforts to calibrate the quadrupole field strengths with respect to fixed Hall probes that are used to set the desired field. The work presented here was previously formalized in a technical report compiled by the author, which can be obtained by request.

A.1 Measurement set-up

Since magnets undergo hysteresis, the current applied to the magnet coils must be adjusted based on feed back from strategically placed Hall probe magnetometers, which provide a reference field that is directly proportionate to the field experienced by ions moving through EMMA. The reference field, as measured by the fixed Hall probes, must therefore be calibrated with respect to the field gradient across the magnets. The magnetic field gradient is obtained by recording the field at precisely known distances along the horizontal and vertical axis with respect to the magnet centre. This necessitates a reproducible way of positioning Hall probes within the magnets. For this purpose three jigs were designed to hold several Hall probes at fixed distances and orientations within each of the magnets; three jigs were required for the three different sized vacuum chambers (Q2 and Q3 being identical). The orientation of the Hall probes must fixed so as to measure the maximum flux passing through a local area. Figure A.2 shows Hall probes positioned within the magnet using the measurement jig. The reference probe is fixed to the field clamp with an aluminium holder just below the bore of the magnet.

The vacuum chambers, inside of which the measurement jigs are inserted, were at the time of these measurements resting on the bottom pole tips of each quadrupole doublet. Therefore the measurement positions on the jig did not reflect the true co-ordinates of the Hall probes with respect to the axis of the magnets. To overcome this issue alignment plates were manufactured to fix onto each of the quadrupole field clamps using the existing bolt holes. Three brackets attached to each alignment plate hold the vacuum chambers in position. Alignment was performed by the TRIUMF beam lines group using precise laser tracker measurements.

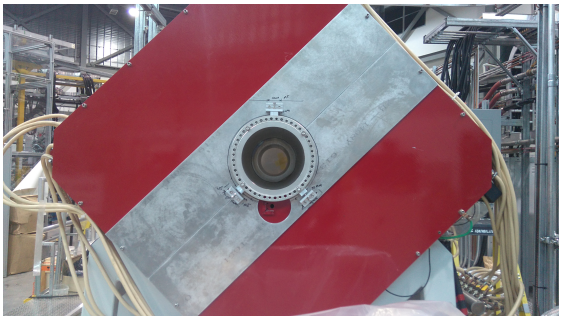

FIGURE A.3: Alignment plate fixed to the Q4 field clamps

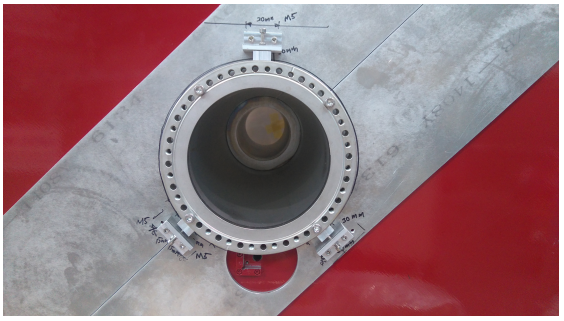

FIGURE A.4: Close-up image of alignment brackets holding the downstream flange of the Q3-Q4 vacuum chamber.

Each of the probes is connected to its respective teslameter. It is important to note that the teslameter should only be turned on once the Hall probe is connected, as per instructions from the manufacturer. The teslameters can then be connected to a voltmeter, where 1 Volt = 1 Tesla. Additional information on each of the quadrupole magnets, dipole magnet, and the voltmeter can be found in their respective manuals; digital copies of which are held by the author and Dr B. Davids.

A.2 Hall probe calibration check

Before beginning the quadrupole measurements, the calibration of each Hall probe was first checked with respect to an NMR probe. This was achieved by placing the Hall

probes, along with an NMR probe, inside the uniform field region of the EMMA dipole magnet. As shown by Figure A.5 the probes were all clamped between two aluminium bocks to ensure that they are held perpendicular to the magnetic field. The field measured by each Hall probe was recorded with respect to the NMR probe with various applied currents to the magnet. The results of this calibration check indicated that the Hall probes have indeed retained the calibration guaranteed by the manufacturer. According to the manual for the Hall probes, a measurement error of $(0.0001 \times B + 0.2)$ mT is expected, i.e. a minimum error of ± 0.2 mT which increases slightly with larger measured fields. Note that the Q1 probe was omitted from this calibration check since, due to its far shorter length, it was not used in the measurement of any of the quadrupole field gradients therefore its exact calibration with respect to the other probes need not be confirmed.

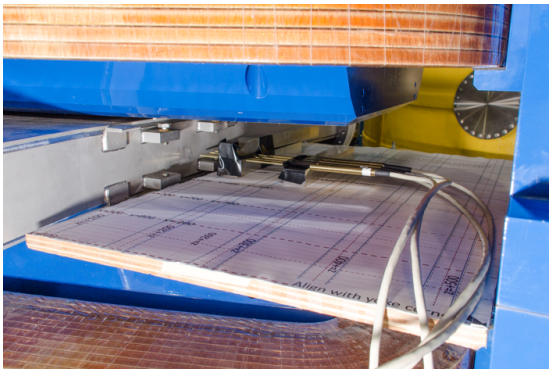

FIGURE A.5: Hall probes inserted into the uniform field region of the dipole magnet.

A.3 Measurement procedure

The measurement procedure begins by inserting the reference probe into a designated hole in the field clamps located immediately below the bore of the magnet. The reference probe is held in place by aluminium mounting blocks which are aligned with respect to an L-bracket screwed to the field clamp. It is important to ensure that the handle of the probe is held flush with the mounting block, and for preference it is desirable from a controls standpoint to orient the probe so as to measure a positive field. It is crucial that, once fixed in position, the reference probes are not disturbed during the calibration procedure, as even slight knocks will alter the measured field. The remaining probes are then used for the field gradient measurements by inserting them into the measurement jig, again ensuring that that handle is flush with the jig.

The mounting blocks for Q2 and Q3 fix the orientation of the reference probe, however for Q1 and Q4 the blocks allow considerable freedom for rotation as shown by Figure A.7. It is for this reason, along with the aforementioned sensitivity of the reference probe field,

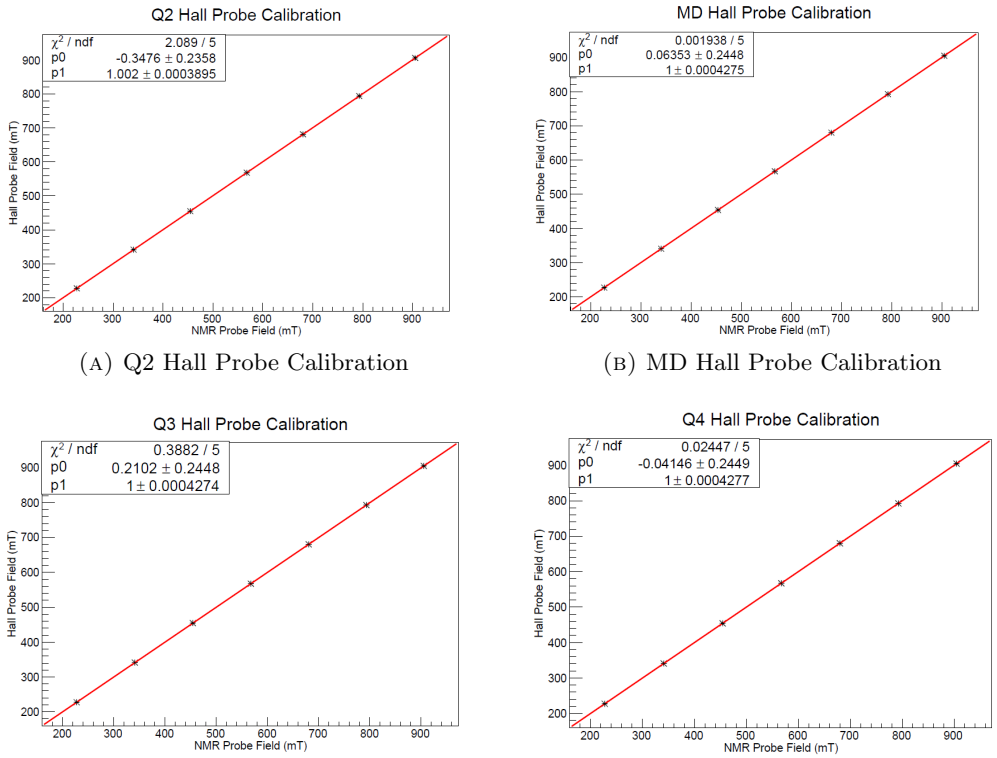

(A) Q2 Hall Probe Calibration

(B) MD Hall Probe Calibration

(C) Q3 Hall Probe Calibration

(D) Q4 Hall Probe Calibration

FIGURE A.6: Calibration of Hall probes with respect to an NMR probe.

that once a quadrupole has been calibrated its respective reference probe is left fixed into position and is not withdrawn to be used in subsequent calibrations. This means that the order in which the quadrupole magnets are calibrated required careful consideration. Since the Q1 Hall probe is too short to be used for the other magnet calibrations, the Q1 field gradient was calibrated first with the full complement of probes available for field measurements. The second was Q4 since it has the largest bore diameter and therefore the most radial positions to measure. Finally Q3 and Q2 were calibrated, with the final set of measurements performed using only the MD (magnetic dipole) Hall probe.

Once the reference probe is in position, the remaining available probes can be inserted into the measurement jig. The current flowing through the magnets is then incrementally increased, recording the field at each position on the jig as well as the the reference field. A 5 to 10 minute waiting period must be allowed after altering the current until the probe reading settles on a constant value. The field is also recorded for each possible probe orientation i.e. flipping the orientation of a probe within the same slot. The average of the field reading for each orientation effectively compensates for the exact depth of the sensitive region within the probe being unknown.

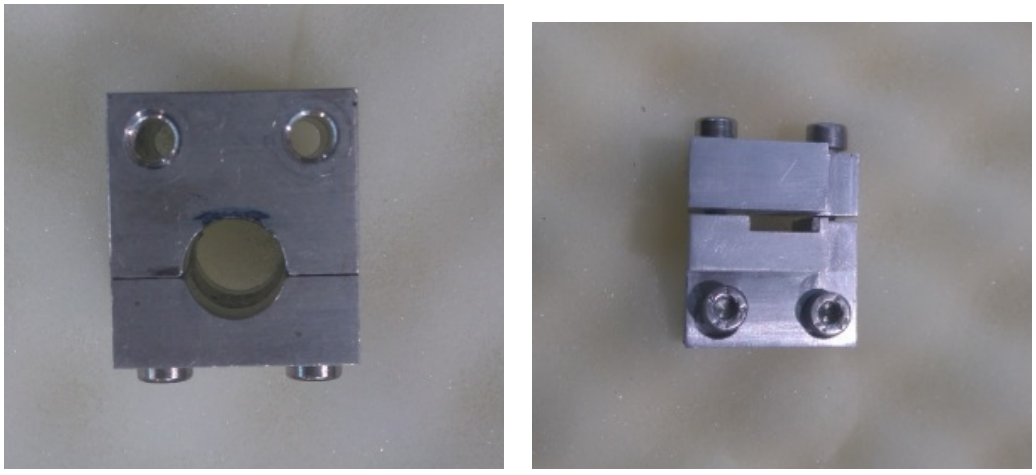

(A) Q1 and Q4 (B) Q2 and Q3.

FIGURE A.7: Mounting blocks for each quadrupole magnet's Hall probe.

A.4 Results

Figure A.8 shows the field gradient for each quadrupole as a function of the reference field. The linear relationships and associated fit coefficients allow each quadrupole to be tuned using their reference probes. The field gradients are calculated by fitting the field recorded at each probe position on the jig vs distance from the center. It was noticed that slight misalignment of the vacuum chamber resulted in a discrepancy between the field recorded at the same radial distance from the center, for instance the field at +20 mm in Q1 recorded a higher field than -20 mm. This means that the vacuum chamber was aligned off center and towards the positive direction. This misalignment was compensated for by averaging the two fields, since the increase in the field at +20 mm is proportional to the decrease at -20 mm, the field gradient of course being the constant of proportionality. The magnitude of the misalignment can be estimated by working backwards from a calculated field gradient. For instance in the case of Q2 the misalignment in both the vertical and horizontal directions is roughly between 0.4 and 0.8 mm. In addition, the extent to which the sensitive area of the probe deviates from its central axis can be calculated by working backwards from a known field gradient. In the case of the MD probe this results in an expected deviation of 0.2 ± 0.1 mm. This result is roughly 10% of the probe thickness.

The manual for each quadrupole includes measurements of the field gradient with respect to the applied current. The purpose of this calibration is to express the field gradient in relation to a reference field, however it is nevertheless useful to compare the obtained results with those quoted by the manufacturer (Bruker). Figure A.9 shows how the Bruker measurements compare with those obtained through this work. Overall the agreement between these measurements and those performed by Bruker are in close

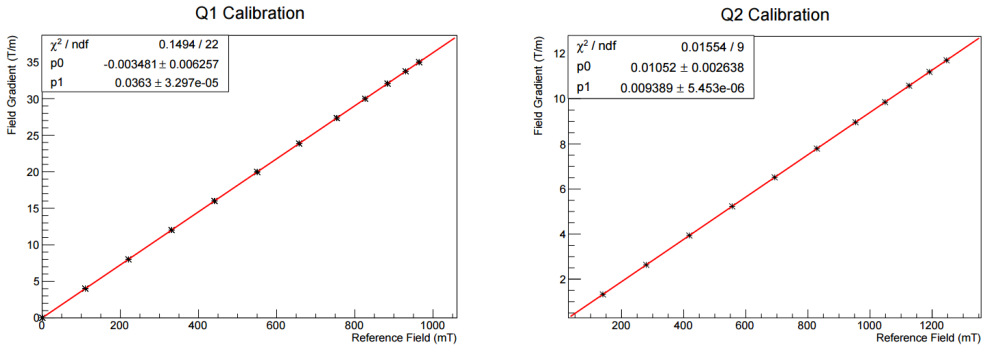

(A) Q1

(B) Q2

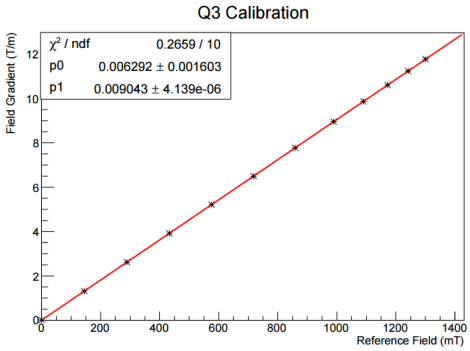

(C) Q3

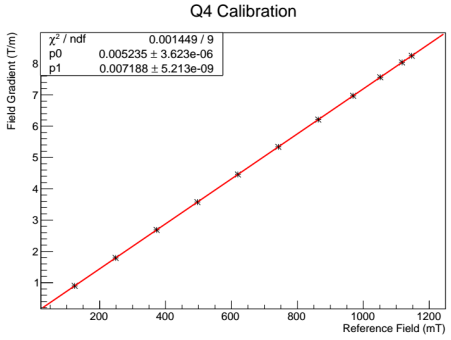

(D) Q4

FIGURE A.8: Graphs showing quadrupole field gradients plotted against reference probe field.

agreement, though it should be emphasized that hysteresis effects will mean that it is not unexpected to see some deviation between these data sets

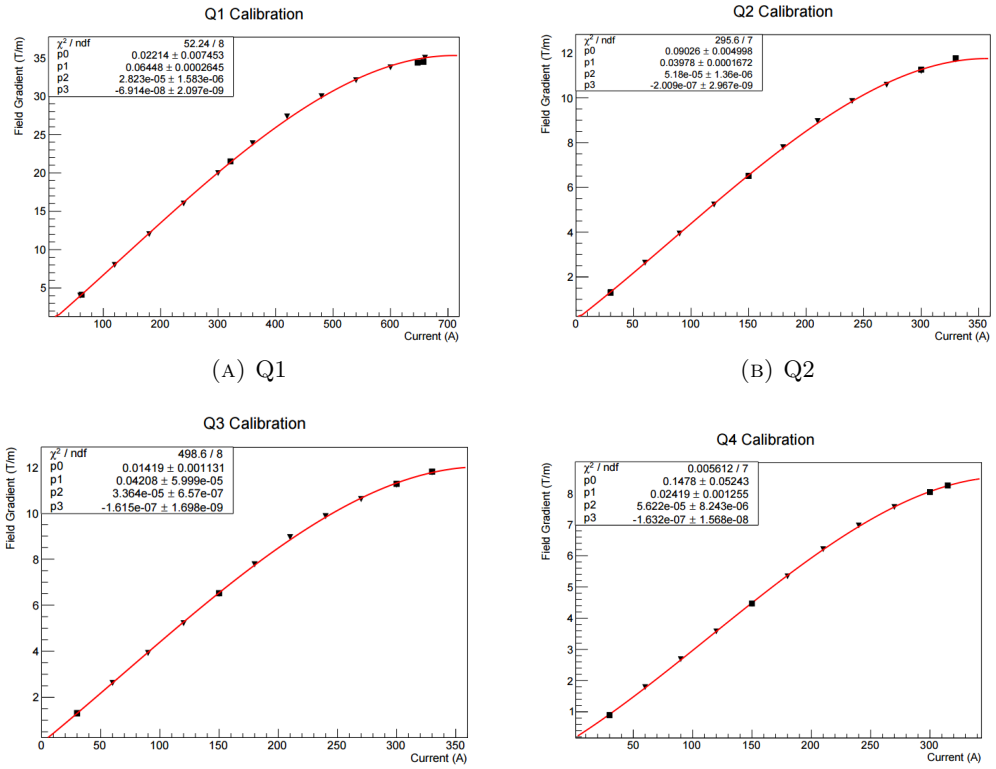

(A) Q1 (B) Q2

(C) Q3 (D) Q4

FIGURE A.9: Graphs showing quadrupole field gradients plotted against current. Triangles indicate measurements obtained in this report. Squares indicate Bruker's measurements.

Appendix B

Direct Capture Reactions with the DRAGON GEANT3 Simulation

In the event that a singles analysis is not possible for a DRAGON data-set, one must rely on a comprehensive simulation of the BGO array and separator developed in GEANT3 to obtain the coincidence efficiency [105]. This simulation has been used extensively to simulate narrow resonances contained within the gas target, but has not been utilized much for the case of direct capture. This appendix sets-out an approach for modifying the simulation inputs to more accurately simulate direct capture, given that the characteristics of direct capture reactions differ from resonant reactions in ways that could influence the estimated efficiency.

The direct capture cross section will be more-or-less uniform across the DRAGON gas target, in contrast to the case of resonant capture reactions which will predominantly occur within a small volume - ideally in the centre - of the target. The distribution of reactions across the gas target will influence the distribution of emitted γ-rays, as well as the recoil cone distribution at the exit aperture of the target, both of which could impact the estimated coincidence efficiency. By altering the resonance energy input to some arbitrarily large value, one can effectively produce a uniform reaction distribution across the target without altering the simulation code itself. A comparison of reaction locations within the target, for resonant and direct capture reactions, is shown by Figure B.1.

Another complication arises due to the unknown partial cross sections for capture into the various bound states. The instance of an unknown decay scheme for a DRAGON

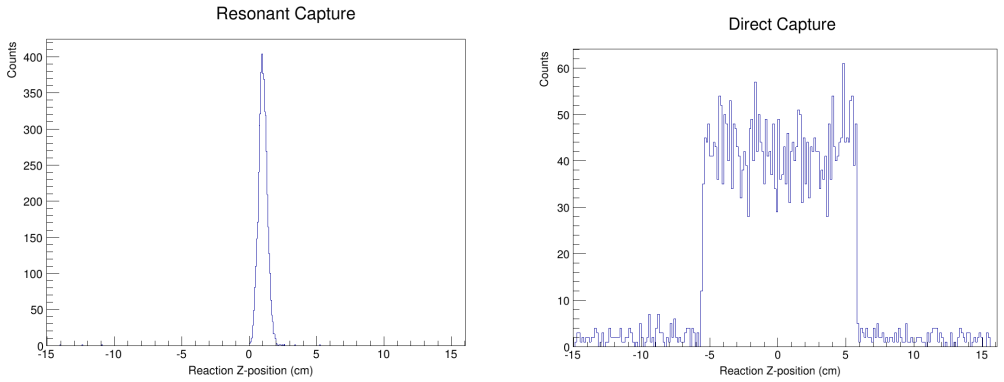

(A) (B)

FIGURE B.1: Simulated reaction profiles for (A) resonant and (B) direct capture across the DRAGON gas target

experiment has been dealt with before for ^{76}Se$(\alpha,\gamma)^{80}$Kr, whereby the compound nuclei are formed in a continuum of excited states in which no particular resonance dominates the cross section [106]. However, the solution of splitting the excitation energy into 50 randomly distributed fractions and simulating over 2000 possible decay schemes is not appropriate for the case of direct capture. This is because only a few primary transitions will tend to dominate the direct capture process, therefore an alternative approach must be formulated.

The relative contribution of each state to the direct capture cross-section as a function of energy can be estimated using existing codes; Ref [107] compares the performance of some of these codes, for the specific case of proton radiative capture, with respect to transfer reaction studies. Figure B.2 plots the calculated partial cross sections for the most dominant states contributing to ^{22}Ne$(p,\gamma)^{23}$Na direct capture. The displayed partial cross section for each transition have all been scaled by their respective spectroscopic factors found by Görres *et al* [75]. Using these plots, the branching ratio for each transition can be obtained for each energy at which direct capture measurements were performed. However, as was noted by Hale *et al.*, there is some uncertainty that must be considered with regards to extrapolating from the Görres data using the direct capture model. Hale *et al.* recommended a relative uncertainty of 40% for the total S-factor extrapolated to zero energy [78]. Though one may reasonably ascribe a lower uncertainty to the extrapolated cross section at the energies considered here, a conservative approach was instead taken by sampling each partial cross section from random Gaussian distributions with a sigma width of 40% of the mean value; the mean being set to the partial cross section obtained from each plot in Figure B.2 at the energy under consideration. At each direct capture energy measured, a total 30 different branching ratios were simulated. More simulations were deemed to be unnecessary since the standard deviation in coincidence efficiency averages over all simulations was already below that

of the typical systematic uncertainty in the simulation itself of 10% [105]. Gamma-decay information on secondary transitions were readily available on the NNDC database [91].

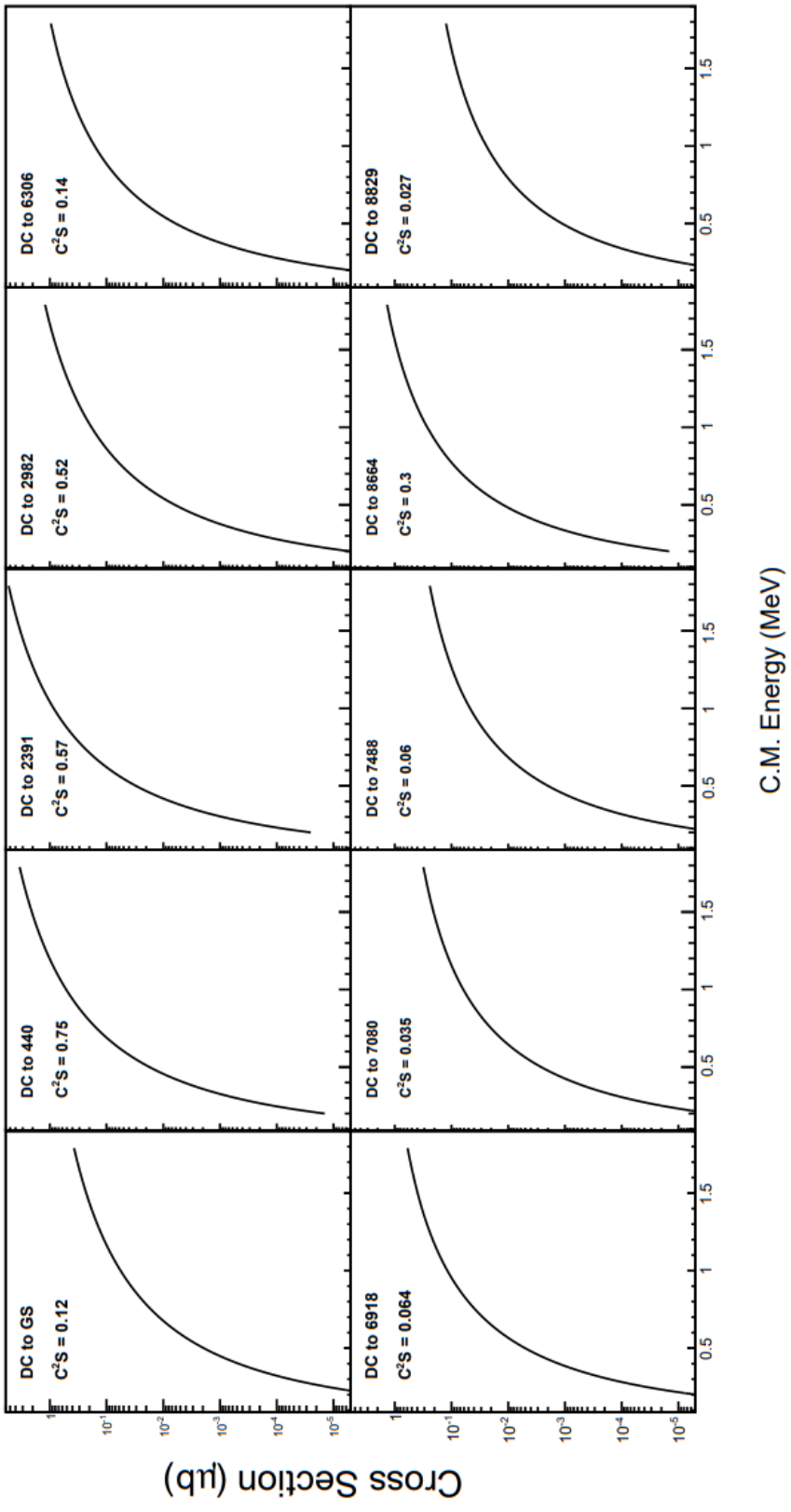

FIGURE B.2: Predicted direct capture cross sections to various secondary states in ^{23}Na. The results have already been scaled by the spectroscopic factors indicated on each panel, obtained from Ref [75]. The calculations were performed using a hard-sphere scattering potential and Woods-Saxon bound-state potential of radius $R = 4.56$ fm and diffuseness $a = 0.7$ fm. The used for these calculations was authored by C. Iliadis, and obtained via private communication with C. Ruiz

Appendix C

Tabulated ^{22}Ne$(p,\gamma)^{23}$Na Thermonuclear Reaction Rate

This appendix contains a numerical table of the $^{22}\mathrm{Ne}(p,\gamma)^{23}\mathrm{Na}$ thermonuclear reaction rate, in $\mathrm{cm}^3\mathrm{mol}^{-1}\mathrm{s}^{-1}$, derived from the measurements made in this thesis. The rate was calculated using the code `RatesMC`, which computes the probability density distribution at each temperature [94]. The log-normal probability density distribution parameters are labelled as 'Log-Norm μ' and Log-Norm σ'. The 'A-D Stat' or Anderson-Darling test statistic indicates how well the reaction rate at a given temperature is described by a log-normal distribution. An A-D test statistic of less than ≈ 1 means that the reaction rate is well described by the given log-normal distribution. However the log-normal assumption has been shown by inspection to hold well with A-D statistics in the range of $\approx 1 - 30$ [108].

T_9	Low Rate	Median Rate	High Rate	Log-Norm μ	Log-Norm σ	A-D Stat
0.01	4.17×10^{-25}	6.73×10^{-25}	1.08×10^{-24}	-5.57×10^{1}	4.76×10^{-1}	3.86×10^{-1}
0.011	1.57×10^{-23}	2.44×10^{-23}	3.77×10^{-23}	-5.21×10^{1}	4.33×10^{-1}	3.95×10^{-1}
0.012	3.18×10^{-22}	4.83×10^{-22}	7.25×10^{-22}	-4.91×10^{1}	4.05×10^{-1}	4.56×10^{-1}
0.013	4.01×10^{-21}	5.99×10^{-21}	8.79×10^{-21}	-4.66×10^{1}	3.87×10^{-1}	4.05×10^{-1}
0.014	3.47×10^{-20}	5.12×10^{-20}	7.39×10^{-20}	-4.44×10^{1}	3.77×10^{-1}	3.27×10^{-1}
0.015	2.23×10^{-19}	3.27×10^{-19}	4.71×10^{-19}	-4.26×10^{1}	3.72×10^{-1}	3.14×10^{-1}
0.016	1.12×10^{-18}	1.64×10^{-18}	2.37×10^{-18}	-4.10×10^{1}	3.72×10^{-1}	3.24×10^{-1}
0.018	1.62×10^{-17}	2.38×10^{-17}	3.47×10^{-17}	-3.83×10^{1}	3.77×10^{-1}	4.12×10^{-1}
0.02	1.35×10^{-16}	1.99×10^{-16}	2.95×10^{-16}	-3.62×10^{1}	3.87×10^{-1}	5.51×10^{-1}
0.025	5.69×10^{-15}	8.67×10^{-15}	1.32×10^{-14}	-3.24×10^{1}	4.18×10^{-1}	6.72×10^{-1}
0.03	6.53×10^{-14}	1.02×10^{-13}	1.60×10^{-13}	-2.99×10^{1}	4.45×10^{-1}	6.50×10^{-1}
0.04	1.25×10^{-12}	2.05×10^{-12}	3.33×10^{-12}	-2.69×10^{1}	4.85×10^{-1}	5.85×10^{-1}
0.05	6.96×10^{-12}	1.16×10^{-11}	1.93×10^{-11}	-2.52×10^{1}	5.06×10^{-1}	4.76×10^{-1}

0.06	2.32×10^{-11}	3.80×10^{-11}	6.24×10^{-11}	-2.40×10^{1}	4.89×10^{-1}	6.34×10^{-1}
0.07	8.94×10^{-11}	1.25×10^{-10}	1.82×10^{-10}	-2.28×10^{1}	3.52×10^{-1}	7.35×10^{0}
0.08	5.89×10^{-10}	7.31×10^{-10}	9.28×10^{-10}	-2.10×10^{1}	2.26×10^{-1}	3.44×10^{0}
0.09	4.15×10^{-9}	5.14×10^{-9}	6.53×10^{-9}	-1.91×10^{1}	2.26×10^{-1}	4.67×10^{0}
0.1	2.38×10^{-8}	2.93×10^{-8}	3.70×10^{-8}	-1.73×10^{1}	2.20×10^{-1}	4.17×10^{0}
0.11	1.06×10^{-7}	1.28×10^{-7}	1.59×10^{-7}	-1.59×10^{1}	2.04×10^{-1}	3.95×10^{0}
0.12	3.75×10^{-7}	4.48×10^{-7}	5.47×10^{-7}	-1.46×10^{1}	1.87×10^{-1}	4.00×10^{0}
0.13	1.11×10^{-6}	1.30×10^{-6}	1.56×10^{-6}	-1.35×10^{1}	1.71×10^{-1}	4.00×10^{0}
0.14	2.82×10^{-6}	3.27×10^{-6}	3.87×10^{-6}	-1.26×10^{1}	1.57×10^{-1}	3.83×10^{0}
0.15	6.39×10^{-6}	7.32×10^{-6}	8.50×10^{-6}	-1.18×10^{1}	1.45×10^{-1}	3.59×10^{0}
0.16	1.31×10^{-5}	1.49×10^{-5}	1.72×10^{-5}	-1.11×10^{1}	1.34×10^{-1}	3.34×10^{0}
0.18	4.43×10^{-5}	4.94×10^{-5}	5.57×10^{-5}	-9.91×10^{0}	1.15×10^{-1}	2.53×10^{0}
0.2	1.24×10^{-4}	1.36×10^{-4}	1.50×10^{-4}	-8.90×10^{0}	9.66×10^{-2}	1.93×10^{0}
0.25	1.44×10^{-3}	1.54×10^{-3}	1.66×10^{-3}	-6.47×10^{0}	7.55×10^{-2}	3.91×10^{0}
0.3	1.83×10^{-2}	1.99×10^{-2}	2.20×10^{-2}	-3.91×10^{0}	9.49×10^{-2}	1.11×10^{1}
0.35	1.52×10^{-1}	1.65×10^{-1}	1.81×10^{-1}	-1.80×10^{0}	9.08×10^{-2}	1.19×10^{1}
0.4	7.87×10^{-1}	8.47×10^{-1}	9.23×10^{-1}	-1.59×10^{-1}	8.19×10^{-2}	1.29×10^{1}
0.45	2.87×10^{0}	3.07×10^{0}	3.31×10^{0}	1.13×10^{0}	7.33×10^{-2}	1.37×10^{1}
0.5	8.17×10^{0}	8.65×10^{0}	9.27×10^{0}	2.16×10^{0}	6.58×10^{-2}	1.41×10^{1}
0.6	3.99×10^{1}	4.19×10^{1}	4.43×10^{1}	3.74×10^{0}	5.41×10^{-2}	1.32×10^{1}
0.7	1.27×10^{2}	1.33×10^{2}	1.39×10^{2}	4.89×10^{0}	4.71×10^{-2}	9.52×10^{0}
0.8	3.08×10^{2}	3.21×10^{2}	3.37×10^{2}	5.77×10^{0}	4.48×10^{-2}	5.82×10^{0}
0.9	6.23×10^{2}	6.52×10^{2}	6.84×10^{2}	6.48×10^{0}	4.69×10^{-2}	4.97×10^{0}
1	1.11×10^{3}	1.16×10^{3}	1.23×10^{3}	7.06×10^{0}	5.21×10^{-2}	6.45×10^{0}
1.25	3.23×10^{3}	3.43×10^{3}	3.69×10^{3}	8.15×10^{0}	6.94×10^{-2}	1.18×10^{1}
1.5	6.76×10^{3}	7.28×10^{3}	7.96×10^{3}	8.90×10^{0}	8.41×10^{-2}	1.28×10^{1}
1.75	1.17×10^{4}	1.27×10^{4}	1.40×10^{4}	9.46×10^{0}	9.37×10^{-2}	1.21×10^{1}
2	1.77×10^{4}	1.94×10^{4}	2.15×10^{4}	9.88×10^{0}	9.92×10^{-2}	1.12×10^{1}
2.5	3.21×10^{4}	3.53×10^{4}	3.93×10^{4}	1.05×10^{1}	1.02×10^{-1}	9.85×10^{0}
3	4.78×10^{4}	5.24×10^{4}	5.83×10^{4}	1.09×10^{1}	1.01×10^{-1}	9.15×10^{0}
3.5	6.33×10^{4}	6.91×10^{4}	7.65×10^{4}	1.11×10^{1}	9.69×10^{-2}	8.61×10^{0}
4	7.74×10^{4}	8.41×10^{4}	9.28×10^{4}	1.13×10^{1}	9.31×10^{-2}	8.15×10^{0}
5	1.00×10^{5}	1.08×10^{5}	1.18×10^{5}	1.16×10^{1}	8.64×10^{-2}	7.10×10^{0}
6	1.15×10^{5}	1.24×10^{5}	1.35×10^{5}	1.17×10^{1}	8.14×10^{-2}	5.99×10^{0}
7	1.24×10^{5}	1.33×10^{5}	1.44×10^{5}	1.18×10^{1}	7.78×10^{-2}	4.98×10^{0}
8	1.28×10^{5}	1.37×10^{5}	1.49×10^{5}	1.18×10^{1}	7.51×10^{-2}	4.16×10^{0}
9	1.30×10^{5}	1.39×10^{5}	1.50×10^{5}	1.18×10^{1}	7.30×10^{-2}	3.47×10^{0}
10	1.29×10^{5}	1.38×10^{5}	1.48×10^{5}	1.18×10^{1}	7.15×10^{-2}	2.95×10^{0}

TABLE C.1: Numerical table of the ^{22}Ne$(p,\gamma)^{23}$Na thermonuclear reaction rate calculated using the work presented in this thesis.

Bibliography

[1] A. S. Eddington. *The Internal Constitution of the Stars.* 1926.

[2] C. Iliadis. *Nuclear Physics of Stars.* Wiley-VCH Verlag, 2007.

[3] A. C. Phillips. *The Physics of Stars, 2nd Edition.* 1999.

[4] E. E. Salpeter. Nuclear Reactions in Stars Without Hydrogen. *Astrophys. J.*, 115:326–328, 1952.

[5] Fred Hoyle, D Noel F Dunbar, William A Wenzel, and Ward Whaling. A state in C^{12} predicted from astrophysical evidence. *Phys. Rev.*, 92(4):1095–1095, 1953.

[6] D. N. F. Dunbar, R. E. Pixley, W. A. Wenzel, and W. Whaling. The 7.68-Mev state in C^{12}. *Phys. Rev.*, 92:649–650, 1953.

[7] Charles W Cook, William A Fowler, Charles C Lauritsen, and Thomas Lauritsen. B^{12}, C^{12}, and the Red Giants. *Phys. Rev.*, 107(2):508, 1957.

[8] Fay Ajzenberg-Selove. Energy levels of light nuclei A= $13 - 15$. *Nuclear Physics A*, 523(1):1–196, 1991.

[9] P. Ventura and F. D'Antona. Full computation of massive AGB evolution. *Astronomy & Astrophysics*, 431(1):279–288, 2005.

[10] Harm J Habing and Hans Olofsson. *Asymptotic giant branch stars.* Springer Science & Business Media, 2013.

[11] R. G. Izzard, M. Lugaro, A. I. Karakas, C. Iliadis, and M. van Raai. Reaction rate uncertainties and the operation of the NeNa and MgAl chains during HBB in intermediate-mass AGB stars. *Astronomy & Astrophysics*, 466(2):641–648, 2007.

[12] Keith M Ashman and Stephen E Zepf. Some constraints on the formation of globular clusters. *The Astronomical Journal*, 122(4):1888, 2001.

[13] Brian Chaboyer, Pierre Demarque, Peter J. Kernan, and Lawrence M. Krauss. A lower limit on the age of the universe. *Science*, 271(5251):957–961, 1996.

[14] G. Piotto, L. R. Bedin, J. Anderson, I. R. King, S. Cassisi, A. P. Milone, S. Villanova, A. Pietrinferni, and A. Renzini. A triple main sequence in the globular cluster NGC 2808. *The Astrophysical Journal Letters*, 661(1):L53, 2007.

[15] E. Carretta, A. Bragaglia, R. G. Gratton, S. Lucatello, G. Catanzaro, F. Leone, M. Bellazzini, R. Claudi, V. D'Orazi, Y. Momany, S. Ortolani, E. Pancino, G. Piotto, A. Recio-Blanco, and E. Sabbi. Na-O anticorrelation and HB. VII. The chemical composition of first and second-generation stars in 15 globular clusters from GIRAFFE spectra. *A & A*, 505:117–138, 2009.

[16] Eugenio Carretta, Angela Bragaglia, RG Gratton, Alejandra Recio-Blanco, Sara Lucatello, Valentina D'Orazi, and Santi Cassisi. Properties of stellar generations in globular clusters and relations with global parameters. *Astronomy & Astrophysics*, 516:A55, 2010.

[17] Raffaele G Gratton, Eugenio Carretta, and Angela Bragaglia. Multiple populations in globular clusters. *The Astronomy and Astrophysics Review*, 20(1):50, 2012.

[18] RG Gratton, P Bonifacio, A Bragaglia, E Carretta, V Castellani, M Centurion, A Chieffi, R Claudi, G Clementini, F D'Antona, et al. The O-Na and Mg-Al anticorrelations in turn-off and early subgiants in globular clusters. *Astronomy & Astrophysics*, 369(1):87–98, 2001.

[19] Eugenio Carretta, RG Gratton, Angela Bragaglia, Piercarlo Bonifacio, and Luca Pasquini. Abundance analysis of turn-off and early subgiant stars in the globular cluster 47 Tuc (NGC 104). *Astronomy & Astrophysics*, 416(3):925–940, 2004.

[20] Eugenio Carretta, Angela Bragaglia, RG Gratton, Francesco Leone, Alejandra Recio-Blanco, and Sara Lucatello. Na-O anticorrelation and HB-I. The Na-O anticorrelation in NGC 2808. *Astronomy & Astrophysics*, 450(2):523–533, 2006.

[21] R. Gratton, C. Sneden, and E. Carretta. Abundance Variations Within Globular Clusters. *Annu. Rev. Astron. Astrophys*, 42:385–440, 2004.

[22] Pavel A Denissenkov and Falk Herwig. The abundance evolution of oxygen, sodium, and magnesium in extremely metal poor intermediate-mass stars: Implications for the self-pollution scenario in globular clusters. *The Astrophysical Journal Letters*, 590(2):L99, 2003.

[23] A. W. Shafter. The Galactic Nove Rate Revisited. *The Astrophysical Journal*, 834(2):196, 2017.

[24] Jordi José and Margarita Hernanz. Nucleosynthesis in classical novae: CO versus ONe white dwarfs. *The Astrophysical Journal*, 494(2):680, 1998.

[25] B. Paczynski. Evolutionary processes in close binary systems. *Annual Review of Astronomy and Astrophysics*, 9(1):183–208, 1971.

[26] A. Parikh, J. José, and G. Sala. Classical novae and Type I X-ray bursts: Challenges for the 21st century. *AIP Advances*, 4(4):041002, 2014.

[27] http://www.astroart.org/extrasolar. (Accessed: 2018-01-18).

[28] Christian Iliadis, Art Champagne, Jordi José, Sumner Starrfield, and Paul Tupper. The effects of thermonuclear reaction-rate variations on nova nucleosynthesis: A sensitivity study. *The astrophysical Journal supplement series*, 142(1):105, 2002.

[29] D. J. Rowe and J. L. Wood. *Fundamentals of Nuclear Models: Foundational Models*. World Scientific Press, 2010.

[30] P.J. Brussaard and P.W. Glaudemans. *Shell Model Applications in Nuclear Spectroscopy*. Elsevier, 1977.

[31] W. A. Fowler, C. C. Lauritsen, and T. Lauritsen. Gamma-radiation from excited states of light nuclei. *Rev. Mod. Phys.*, 20:236–277, 1948.

[32] D. D. Clayton. *Principles of stellar evolution and nucleosynthesis*. 1983.

[33] W. A. Fowler, G. R. Caughlan, and B. A. Zimmerman. Thermonuclear Reaction Rates. *Annu. Rev. Astron. Astrophs.*, 5:525, 1967.

[34] K. R. Lang. *Astrophysical formulae: A compendium for the physicist and astrophysicist*. 1974.

[35] M. S. Smith and K. Ernst Rehm. Nuclear Astrophysics Measurements with Radioactive Beams. *Annual Review of Nuclear and Particle Science*, 51:91–130, 2001.

[36] A. C. Mueller and B. M. Sherrill. Nuclei at the limits of particle stability. *Annual Review of Nuclear and Particle Science*, 43:529–584, 1993.

[37] M. Marchetto. Commissioning of the 20 MV superconducting LINAC upgrade at TRIUMF. *Proceedings of 2011 Particle Accelerator Conference, New York, NY, USA*.

[38] F. Ames, R. Baartman, P. Bricault, K. Jayamanna, M. McDonald, P. Schmor, T. Spanjers, D. H. L. Yuan, and T. Lamy. The ECRIS charge state breeding project at TRIUMF. *Review of Scientific Instruments*, 79(2):02A902, 2008.

[39] J. Dilling and R. Krücken. The experimental facilities at ISAC. *Hyperfine Interactions*, 225:111–114, 2014.

[40] K. Jayamanna, F. Ames, G. Cojocaru, R. Baartman, P. Bricault, R. Dube, R. Laxdal, M. Marchetto, M. MacDonald, P. Schmor, G. Wight, and D. Yuan. Off-line ion source terminal for ISAC at TRIUMFa). *Review of Scientific Instruments*, 79(2):02C711–02C711–4, 2008.

[41] C. E. Svensson, P. Amaudruz, C. Andreoiu, A. Andreyev, R. A. E. Austin, G. C. Ball, D. Bandyopadhyay, A. J. Boston, R. S. Chakrawarthy, A. A. Chen, R. Churchman, T. E. Drake, P. Finlay, P. E. Garrett, G. F. Grinyer, G. Hackman, B. Hyland, B. Jones, R. Kanungo, R. Maharaj, J. P. Martin, D. Morris, A. C. Morton, C. J. Pearson, A. A. Phillips, J. J. Ressler, R. Roy, F. Sarazin, M. A. Schumaker, H. C. Scraggs, M. B. Smith, N. Starinsky, J. J. Valiente-Dobón, J. C. Waddington, and L. M. Watters. TIGRESS: TRIUMF-ISAC gamma-ray escape-suppressed spectrometer. *Journal of Physics G Nuclear Physics*, 31:S1663–S1668, 2005.

[42] B. Davids and C. N. Davids. EMMA: A recoil mass spectrometer for ISAC-II at TRIUMF. *Nuclear Instruments and Methods in Physics Research A*, 544:565–576, 2005.

[43] C. N. Davids, B. B. Back, K. Bindra, D. J. Henderson, W. Kutschera, T. Lauritsen, Y. Nagame, P. Sugathan, A. V. Ramayya, and W. B. Walters. Startup of the Fragment Mass Analyzer at ATLAS. *Nuclear Instruments and Methods in Physics Research B*, 70:358–365, 1992.

[44] Paola Spolaore, James Daniel Larson, Cosimo Signorini, Silvio Beghini, Zhu Xi-Kai, and Si Hou-Zhi. A recoil mass spectrometer for the xtu tandem at lnl. *Nuclear Instruments and Methods in Physics Research Section A: Accelerators, Spectrometers, Detectors and Associated Equipment*, 238(2):381 – 392, 1985.

[45] H. Wollnik, J. Brezina, and M. Berz. Gios-beamtrace — a program package to determine optical properties of intense ion beams. *Nuclear Instruments and Methods in Physics Research Section A: Accelerators, Spectrometers, Detectors and Associated Equipment*, 258(3):408411, 1987.

[46] AMETEK (ORTEC) Advanced Measurement Technology. ULTRA and ULTRA AS Ion-Impanted-Silicon Charged-Particle Detectors. www.ortec-online.com/-/media/ametekortek/brochures/ultra.pdf (Date accessed: 09/04/2017).

[47] AMETEK (ORTEC) Advanced Measurement Technology. *142A,B, and C Preamplifier brochure.* www.ortec-online.com/-/media/ametekortek/brochures/142a-b-c.pdf (Date accessed: 09/04/2017).

[48] AMETEK (ORTEC) Advanced Measurement Technology. Preamplifier Selection Guides. www.ortec-online.com/-/media/ametekortek/other/preamplifier-selection-guide.pdf?la=en (Date accessed: 09/04/2017).

[49] D. A. Hutcheon, S. Bishop, L. Buchmann, M. L. Chatterjee, A. A. Chen, J. M. D'Auria, S. Engel, D. Gigliotti, U. Greife, D. Hunter, A. Hussein, C. C. Jewett, N. Khan, M. Lamey, A. M. Laird, W. Liu, A. Olin, D. Ottewell, J. G. Rogers, G. Roy, H. Sprenger, and C. Wrede. The DRAGON facility for nuclear astrophysics at TRIUMF-ISAC: design, construction and operation. *Nuclear Instruments and Methods in Physics Research A*, 498:190–210, 2003.

[50] M. Couder, G. P. A. Berg, J. Görres, P. J. LeBlanc, L. O. Lamm, E. Stech, M. Wiescher, and J. Hinnefeld. Design of the recoil mass separator St. George. *Nuclear Instruments and Methods in Physics Research A*, 587:35–45, 2008.

[51] G. P. A. Berg, D. W. Bardayan, J. C. Blackmon, K. A. Chipps, M. Couder, U. Greife, U. Hager, F. Montes, K. E. Rehm, H. Schatz, M. S. Smith, M. Wiescher, C. Wrede, and A. Zeller. A recoil separator for nuclear astrophysics SECAR. *Nuclear Instruments and Methods in Physics Research B*, 376:165–167, 2016.

[52] J. M. D'Auria, R. E. Azuma, S. Bishop, L. Buchmann, M. L. Chatterjee, A. A. Chen, S. Engel, D. Gigliotti, U. Greife, D. Hunter, A. Hussein, D. Hutcheon, C. C. Jewett, J. José, J. D. King, A. M. Laird, M. Lamey, R. Lewis, W. Liu, A. Olin, D. Ottewell, P. Parker, J. Rogers, C. Ruiz, M. Trinczek, and C. Wrede. The ^{21}Na (p,γ) ^{22}Mg reaction from $E_{c.m.}$ =200 to 1103 keV in novae and x-ray bursts. *Physical Review C*, 69(6):065803, 2004.

[53] S. Engel, D. Hutcheon, S. Bishop, L. Buchmann, J. Caggiano, M. L. Chatterjee, A. A. Chen, J. D'Auria, D. Gigliotti, U. Greife, D. Hunter, A. Hussein, C. C. Jewett, A. M. Laird, M. Lamey, W. Liu, A. Olin, D. Ottewell, J. Pearson, C. Ruiz, G. Ruprecht, M. Trinczek, C. Vockenhuber, and C. Wrede. Commissioning the DRAGON facility at ISAC. *Nuclear Instruments and Methods in Physics Research A*, 553:491–500, 2005.

[54] http://www.iuac.res.in/atmol/ safvan/mridulathesis/node21.html (Date Accessed: 25/03/2017).

[55] Micron Semiconductors. *W1 detector specification sheet.* www.micronsemiconductor.co.uk/pdf/w1.pdf (Date accessed: 16/04/2017).

[56] Glenn F. Knoll. Radiation Detection and Measurement, 2010.

[57] Olchanski, K. *VME-NIMIO32 - General Purpose VME FPGA board. Tech. Rep. TRIUMF, Vancouver, BC, Canada, 2012.*

[58] *Cyclone Device Handbook. Tech. Rep. (Altera Corporation, San Jose, CA, USA, 2008).*

[59] G. Christian, C. Akers, D. Connolly, J. Fallis, D. Hutcheon, K. Olchanski, and C. Ruiz. Design and commissioning of a timestamp-based data acquisition system for the dragon recoil mass separator. *Eur. Phys. J. A*, 50(4):75, 2014.

[60] *Model V792/V792N, 32/16 Channel QDC. Tech. Rep. (CAEN S.p.A., Viareggio, Italy, 2010).*

[61] *Model V812 16 Channel Constant Fraction Discriminator. Tech. Rep. (CAEN S.p.A., Viareggio, Italy, 2011).*

[62] *Model V1190-VX1190 A/B, 128/64 Channel Multihit TDC. Tech. Rep. (CAEN S.p.A., Viareggio, Italy, 2012).*

[63] *Model V785, 16/32 Channel Peak Sensing ADC, Tech. Tech. Rep. (CAEN S.p.A., Viareggio, Italy, 2012).*

[64] MA Meyer and JJA Smit. The energy levels of ^{23}Na. *Nuclear Physics A*, 205(1):177–192, 1973.

[65] Z. B. du Toit, P. R. de Kock, and W. L. Mouton. Resonance strengths, branching ratios and mean lifetimes of nuclear energy levels in 23Na. *Zeitschrift für Physik A Hadrons and nuclei*, 246(2):170–182, 1971.

[66] M Piiparinen, A Anttila, and M Viitasalo. A study of the excited states of ^{23}Na from the ^{22}Ne$(p,\gamma)^{23}$Na reaction. *Zeitschrift für Physik A Hadrons and nuclei*, 247(5):400–407, 1971.

[67] J. Keinonen, M. Riihonen, and A. Anttila. Absolute resonance strengths in the ^{20,21,22}Ne$(p,\gamma)^{21,22,23}$Na and ^{21}Ne$(p,p_1\gamma)^{21}$Ne reactions. *Phys. Rev. C*, 15:579–586, 1977.

[68] PM Endt and C Van der Leun. Strengths of gamma-ray transitions between bound states of A= 21-44 nuclei. *Atomic data and nuclear data tables*, 13(1):67–88, 1974.

[69] R. Longland, C. Iliadis, J. M. Cesaratto, A. E. Champagne, S. Daigle, J. R. Newton, and R. Fitzgerald. Resonance strength in ^{22}Ne$(p,\gamma)^{23}$Na from depth profiling in aluminum. *Phys. Rev. C*, 81:055804, 2010.

[70] D.C. Powell, C. Iliadis, A.E. Champagne, S.E. Hale, V.Y. Hansper, R.A. Surman, and K.D. Veal. Low-energy resonance strengths for proton capture on Mg and Al nuclei. *Nuclear Physics A*, 644(4):263 – 276, 1998.

[71] S Harissopulos, C Chronidou, K Spyrou, Th Paradellis, C Rolfs, WH Schulte, and HW Becker. The ^{27}Al$(p,\gamma)^{28}$Si reaction: direct capture cross-section and resonance strengths at $E_p = 0.2 - 1.12$ MeV. *The European Physical Journal A-Hadrons and Nuclei*, 9(4):479–489, 2000.

[72] K. J. Kelly, A. E. Champagne, R. Longland, and M. Q. Buckner. New recommended $\omega\gamma$ for the $E_r^{\text{c.m.}} = 458$ kev resonance in ^{22}Ne$(p,\gamma)^{23}$Na. *Phys. Rev. C*, 92:035805, 2015.

[73] Rosanna Depalo, Francesca Cavanna, Federico Ferraro, Alessandra Slemer, Tariq Al-Abdullah, Shavkat Akhmadaliev, Michael Anders, Daniel Bemmerer, Zoltán Elekes, Giovanni Mattei, et al. Strengths of the resonances at 436, 479, 639, 661, and 1279 keV in the ^{22}Ne$(p,\gamma)^{23}$Na reaction. *Physical Review C*, 92(4):045807, 2015.

[74] P.M. Endt. Energy levels of A = 21–44 nuclei (VII). *Nuclear Physics A*, 521:1 – 400, 1990.

[75] J Görres, HW Becker, L Buchmann, C Rolfs, P Schmalbrock, HP Trautvetter, A Vlieks, JW Hammer, and TR Donoghue. Proton-induced direct capture on ^{22}Ne*and*^{23}Na. *Nuclear Physics A*, 408(2):372–396, 1983.

[76] C. Rolfs, W.S. Rodne, M.H. Shapiro, and H. Winkler. Hydrogen burning of ^{20}Ne*and*^{22}Ne in stars. *Nuclear Physics A*, 241(3):460 – 486, 1975.

[77] C. Rolfs. Spectroscopic factors from radiative capture reactions. *Nuclear Physics A*, 217(1):29 – 70, 1973.

[78] S E. Hale, A.E. Champagne, C Iliadis, V Y. Hansper, D C. Powell, and J C. Blackmon. Investigation of the ^{22}Ne$(p,\gamma)^{23}$Na reaction via $(^3\text{He}, d)$ spectroscopy. 65, 2001.

[79] K. J. Kelly, A. E. Champagne, L. N. Downen, J. R. Dermigny, S. Hunt, C. Iliadis, and A. L. Cooper. New measurements of low-energy resonances in the ^{22}Ne$(p,\gamma)^{23}$Na reaction. *Phys. Rev. C*, 95:015806, 2017.

[80] D. G. Jenkins, M. Bouhelal, S. Courtin, M. Freer, B. R. Fulton, F. Haas, R. V. F. Janssens, T. L. Khoo, C. J. Lister, E. F. Moore, W. A. Richter, B. Truett, and A. H. Wuosmaa. γ-ray spectroscopy of the $A = 23$, $T = 1/2$ nuclei ^{23}Na and ^{23}Mg: High-spin states, mirror symmetry, and applications to nuclear astrophysical reaction rates. *Phys. Rev. C*, 87:064301, 2013.

[81] R.B. Firestone. Nuclear Data Sheets for A = 23. *Nuclear Data Sheets*, 108:1 – 78, 2007.

[82] J. Görres, C. Rolfs, P. Schmalbrock, H.P. Trautvetter, and J. Keinonen. Search for low-energy resonances in ^{21}Ne$(p,\gamma)^{22}$Na and ^{22}Ne$(p,\gamma)^{23}$Na. *Nuclear Physics A*, 385(1):57 – 75, 1982.

[83] F. Cavanna, R. Depalo, M. Aliotta, M. Anders, D. Bemmerer, A. Best, A. Boeltzig, C. Broggini, C. G. Bruno, A. Caciolli, P. Corvisiero, T. Davinson, A. di Leva, Z. Elekes, F. Ferraro, A. Formicola, Zs. Fülöp, G. Gervino, A. Guglielmetti, C. Gustavino, Gy. Gyürky, G. Imbriani, M. Junker, R. Menegazzo, V. Mossa, F. R. Pantaleo, P. Prati, D. A. Scott, E. Somorjai, O. Straniero, F. Strieder, T. Szücs, M. P. Takács, and D. Trezzi. Three new low-energy resonances in the ^{22}Ne$(p,\gamma)^{23}$Na reaction. *Phys. Rev. Lett.*, 115:252501, 2015.

[84] Carlo Broggini, Daniel Bemmerer, Alessandra Guglielmetti, and Roberto Menegazzo. Luna: Nuclear astrophysics deep underground. *Annual Review of Nuclear and Particle Science*, 60(1):53–73, 2010.

[85] R. Depalo, F. Cavanna, M. Aliotta, M. Anders, D. Bemmerer, A. Best, A. Boeltzig, C. Broggini, C. G. Bruno, A. Caciolli, G. F. Ciani, P. Corvisiero, T. Davinson, A. Di Leva, Z. Elekes, F. Ferraro, A. Formicola, Zs. Fülöp, G. Gervino, A. Guglielmetti, C. Gustavino, Gy. Gyürky, G. Imbriani, M. Junker, R. Menegazzo, V. Mossa, F. R. Pantaleo, D. Piatti, P. Prati, O. Straniero, T. Szücs, M. P. Takács, and D. Trezzi. Direct measurement of low-energy ^{22}Ne$(p,\gamma)^{23}$Na resonances. *Phys. Rev. C*, 94:055804, 2016.

[86] A. L. Sallaska, C. Iliadis, A. E. Champagne, S. Goriely, S. Starrfield, and F. X. Timmes. Starlib: A next-generation reaction-rate library for nuclear astrophysics. 2013.

[87] JM Cesaratto, AE Champagne, TB Clegg, MQ Buckner, RC Runkle, and A Stefan. Nuclear astrophysics studies at lena: The accelerators. *Nuclear Instruments and Methods in Physics Research Section A: Accelerators, Spectrometers, Detectors and Associated Equipment*, 623(3):888–894, 2010.

[88] D.A. Hutcheon, C. Ruiz, J. Fallis, J.M. D'Auria, B. Davids, U. Hager, L. Martin, D.F. Ottewell, S. Reeve, and A. Rojas. Measurement of radiative capture resonance energies with an extended gas target. *Nuclear Instruments and Methods in Physics Research Section A: Accelerators, Spectrometers, Detectors and Associated Equipment*, 689:70 – 74, 2012.

[89] O. Tengblad, U.C. Bergmann, L.M. Fraile, H.O.U. Fynbo, and S. Walsh. Novel thin window design for a large-area silicon strip detector. *Nuclear Instruments and Methods in Physics Research Section A: Accelerators, Spectrometers, Detectors and Associated Equipment*, 525(3):458 – 464, 2004.

[90] Chris Wrede, Ahmed Hussein, Joel G Rogers, and John D'Auria. A double sided silicon strip detector as a dragon end detector. *Nuclear Instruments and Methods in Physics Research Section B: Beam Interactions with Materials and Atoms*, 204:619–624, 2003.

[91] *National Nuclear Data Centre.* https://www.nndc.bnl.gov/ (Accessed: 2017/10/05).

[92] Wolfgang A. Rolke and Angel M. López. Confidence intervals and upper bounds for small signals in the presence of background noise. *Nuclear Instruments and Methods in Physics Research Section A: Accelerators, Spectrometers, Detectors and Associated Equipment*, 458(3):745 – 758, 2001.

[93] Ericson. T. A theory of fluctuations in nuclear cross sections. *Ann. Phys.(NY)*, 23:390, 1963.

[94] R. Longland, C. Iliadis, A.E. Champagne, J.R. Newton, C. Ugalde, A. Coc, and R. Fitzgerald. Charged-particle thermonuclear reaction rates: I. monte carlo method and statistical distributions. *Nuclear Physics A*, 841(1):1 – 30, 2010. The 2010 Evaluation of Monte Carlo based Thermonuclear Reaction Rates.

[95] Jina reaclib database. https://groups.nscl.msu.edu/jina/reaclib/db/. (Accessed: 2018/01/12).

[96] Jordi José, Margarita Hernanz, Sachiko Amari, Katharina Lodders, and Ernst Zinner. The imprint of nova nucleosynthesis in presolar grains. *The Astrophysical Journal*, 612(1):414, 2004.

[97] D. D. Clayton. ^{22}Na, Ne–E, extinct radioactive anomalies and unsupported ^{40}Ar. *Nature*, 257(5521):36, 1975.

[98] C Ritter, F Herwig, S Jones, M Pignatari, C Fryer, and R Hirschi. NuGrid stellar data set II. Stellar yields from H to Bi for stellar models with MZAMS = 1-25 $M_{\odot}$ and Z = 0.0001-0.02. *Monthly Notices of the Royal Astronomical Society*, 480(1):538–571, 2018.

[99] Bill Paxton, Lars Bildsten, Aaron Dotter, Falk Herwig, Pierre Lesaffre, and Frank Timmes. Modules for experiments in stellar astrophysics (MESA). *The Astrophysical Journal Supplement Series*, 192(1):3, 2010.

[100] S. Cristallo, O. Straniero, R. Gallino, L. Piersanti, I. Domínguez, and M. T. Lederer. Evolution, nucleosynthesis, and yields of low-mass asymptotic giant branch stars at different metallicities. *The Astrophysical Journal*, 696(1):797, 2009.

[101] Sara Lucatello, Thomas Masseron, Jennifer A Johnson, Marco Pignatari, and Falk Herwig. Fluorine and sodium in C-rich low-metallicity stars. *The Astrophysical Journal*, 729(1):40, 2011.

[102] A. Slemer, P. Marigo, D. Piatti, M. Aliotta, D. Bemmerer, A. Best, A. Boeltzig, A. Bressan, C. Broggini, C. G. Bruno, A. Caciolli, F. Cavanna, G. F. Ciani, P. Corvisiero, T. Davinson, R. Depalo, A. Di Leva, Z. Elekes, F. Ferraro, A. Formicola, Zs. Fülöp, G. Gervino, A. Guglielmetti, C. Gustavino, G. Gyürky, G. Imbriani, M. Junker, R. Menegazzo, V. Mossa, F. R. Pantaleo, P. Prati, O. Straniero, T. Szücs, M. P. Takács, and D. Trezzi. ^{22}Ne and ^{23}Na ejecta from intermediate-mass stars: the impact of the new LUNA rate for $^{22}\mathrm{Ne}(p,\gamma)^{23}\mathrm{Na}$. *Monthly Notices of the Royal Astronomical Society*, 465(4):4817–4837, 2017.

[103] R. J. Mathar. *Solid Angle of a Rectangular Plate.* www.mpia.de/ mathar/public/mathar20051002.pdf (Accessed: 02/04/2018).

[104] A. Gavron. Statistical model calculations in heavy ion reactions. *Phys. Rev. C*, 21:230–236, 1980.

[105] D. Gigliotti. Efficiency calibration measurement and geant simulation of the dragon bgo gamma array at triumf. Master's thesis, University of Northern British Columbia, 2004.

[106] C. Akers. *Radiative Capture Measurements of Astrophysically Important Reactions Using the DRAGON Seperator.* PhD thesis, University of York, 2014.

[107] C. Iliadis and M. Wiescher. Spectroscopic factors from direct proton capture. *Phys. Rev. C*, 69:064305, 2004.

[108] Christian Iliadis, Richard Longland, AE Champagne, Alain Coc, and Ryan Fitzgerald. Charged-particle thermonuclear reaction rates: Ii. tables and graphs of reaction rates and probability density functions. *Nuclear Physics A*, 841(1-4):31–250, 2010.